EXPERIMENTAL ANALYSIS OF FABRICS USED IN FAN BLADE OUT CONTAINMENT IN AIRCRAFT ENGINES

by

Dnyanesh Naik

A Thesis Presented in Partial Fulfillment
of the Requirements for the Degree
Master of Science

ARIZONA STATE UNIVERSITY

August 2005

EXPERIMENTAL ANALYSIS OF FABRICS USED IN FAN BLADE OUT CONTAINMENT IN AIRCRAFT ENGINES

by

Dnyanesh Naik

has been approved

August 2005

APPROVED:

_____, Chair

_____

_____

_____

Supervisory Committee

ACCEPTED:

_____

Department Chair

_____

Dean, Division of Graduate Studies

….To My Parents

ACKNOWLEDGEMENTS

I express my sincere gratitude to my advisor and committee chair, Dr. Barzin Mobasher, for his constant guidance, support and help throughout the course of the my MS studies. I would also like to extend sincere gratitude to Dr. Subramaniam D. Rajan who inspired me to learn FEM and other programming tools which are extremely invaluable. Thanks also to Dr. Apostolos Fafitis for his encouragement throughout my MS degree and for being on my committee. I greatly appreciate the help provided by Dr. Dallas Kingsbury, Peter Goguen and Jeff Long in day to day laboratory work. Without them my task would have been very difficult. Thanks are also extended to my laboratory mate, Satish Sankaran for helping me in research. I am very glad to have moral boosting friends like Saurabh Saksena, Mayur Jain, Sunil Wagh, Janine, Himanshu Joshi, who have always been there at the time of my need. I am grateful to Jitendra and Nora who helped me gel into the MS program and research work with ease. Finally, I would like to acknowledge all my friends, especially Chote and Li Shen for their constant support. I would also like to express my gratitude to all the CEE administrative staffs and folks at International Student Office for their kind help and support. Last and the most important I would like to thank my mother, Manali Naik and father Santosh Naik whose blessings and sacrifice have brought me to this place along with the love from my younger sister Shivangi.

Chapter 1: Introduction

1.1 Introduction

Aircrafts are the mode of travel in the 21st century. Nowadays, most of the airplanes are driven with multi jet propulsion engines. One of the many challenges facing the jet engine designer is to contain a failed fan blade within the engine, so that it threatens neither the passengers nor the airframe. Conventional containment systems are designed using titanium or other high strength metals and alloys to prevent engine fragments from damaging other crucial systems such as the fuselage, fuel lines etc. These metal cases are heavy and require intricate design changes in the aircraft aerodynamics coupled with substantial increase in production costs. This kind of system is known as the hardwall fan case and is designed to reflect the blade back into the engine. Another containment approach being employed recently is the softwall fan case, features a casing of aluminum, over-wound with dry aramid fibers. It is designed to permit a broken blade to pass through its aluminum component, where it is stopped and contained within the external aramid fiber wrap. The key material properties that are to be considered in both types of fan cases are the ductility of the metal cases and, particularly in the case of the softwall system, the energy absorbing capabilities of the aramid fibers and their high strength per unit weight. Also, these fabric wraps are comparatively inexpensive (comparison done on weight basis with metals used in the hardwall case type) and thereby effectively reduce overall aircraft construction expenditure.

Kevlar fabrics are popular wraps that are commonly used in the fan housing of an aircraft engine. Kevlar, golden brown in color, is a synthetic fiber made by EI du Pont de Nemours & Co., Inc. Kevlar is a very large molecule (polymer) formed by combining a large number of smaller molecules, called monomers, in a regular pattern. Kevlar is synthesized from the monomers 1,4-phenyl-diamine (para-phenylenediamine) and terephthaloyl chloride. The result is a polymeric aromatic amide (aramid) with alternating benzene rings and amide groups. When they are produced, these polymer strands are aligned randomly. To make Kevlar, these strands are dissolved and spun, causing the polymer chains to orient in the direction of the fiber. Its chemical name and formula is poly-paraphenylene terephthalamide and $C_{14}H_{10}N_2O_2$ respectively. The chemical structure of Kevlar is shown in figure 1.1.

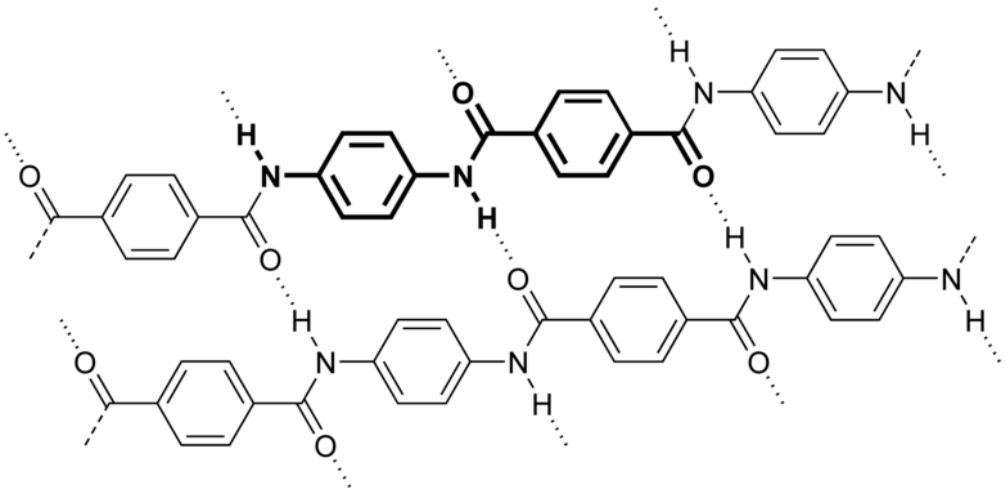

Figure 1.1: Chemical Structure of Kevlar.

Kevlar is about five times stronger than steel on an equal weight basis, yet, at the same time, is lightweight, flexible and comfortable

Kevlar has been used for a variety of purposes as summarized below

- Ropes that secured the airbags in the landing apparatus of the Mars Pathfinder.
- Shrapnel-resistant shielding in jet aircraft engines to protect the passengers if there was an explosion.
- Run-flat tires that allow for greater safety because they won't destroy the wheels.
- Gloves that protect hands and fingers against cuts and slashes.
- Kayaks that provide better impact resistance without the extra weight.
- Skis and helmets that are stronger and lighter in weight to help prevent fatigue.
- Bullet proof vests used by the police and the army.

Zylon is another fabric that could be developed as a potential aircraft engine housing component. In this FAA (Federal Aviation Authority) sponsored research two types of Zylon materials were studied, namely Zylon 500D and Zylon 1500D. Denier (D) is the unit of linear density equal to the mass in grams per 9000 m of fiber, yarn, or other textile strand. Zylon is a trademarked name for a range of thermoset polyurethane materials manufactured by TOBOYO. It consists of rigid-rod chain molecules of poly phenylene-benzobisoxazole (PBO). Figure 1.2 shows the chemical structure of Zylon.

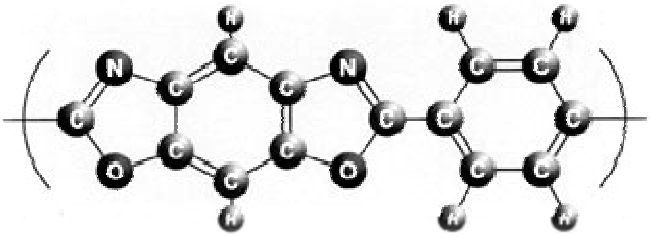

Figure 1.2: Chemical structure of Zylon

Like Kevlar, Zylon is also used in a variety of applications ranging from protective clothing to sporting goods, industrial applications to aerospace needs. Zylon is currently being studied as a potential fragment barrier within the walls of the aircraft fuselage to provide resistance to any ballistic impact. The areal properties of all the three fabrics that form a part of this study are discussed in the following section.

Area Properties

The total cross sectional area for each ply was calculated using the values of the linear density and bulk density of the material. Initially, the cross-section area of each yarn was calculated by taking into account the linear density of the yarn (material) and dividing it by its bulk density. The total cross-section (c/s) area of the specimen was defined as the cross-sectional area per yarn multiplied by the number of yarns per inch of fabric times the total width of the fabric. The dimensions and other properties of the specimens are provided in Table 1.1. In the table, AS stands for As Spun.

Table 1.1: Basic Material Properties

Material	Ply Count	Bulk density (lb/in^3)	Linear density (lb/in)	c/s area per ply (in^2)	Specimen Size (in)
Kevlar AS-49	17 x 17	0.00530516	$9.457(10^{-7})$	$1.78(10^{-4})$	2.5 x 12
Zylon AS-500	35 x 35	0.00567358	$3.175(10^{-7})$	$5.59(10^{-5})$	2.5 x 12
Zylon AS-1500	17 x 17	0.00567358	$9.134(10^{-7})$	$1.61(10^{-4})$	2.5 x 12

1.2 Literature Review

There is a growing interest in the use of dry aramid fabrics such as Kevlar and Zylon for use in the softwall fan case. Several researchers like NASA are conducting ballistic tests under contract to FAA to design fan housing barriers to protect critical aircraft components against debris from fan blade out events. Impact tests were conducted by NASA on dry Kevlar 29® and Zylon AS® fabric specimens in a test configuration designed to simulate its application in a jet engine fan containment system. For the NASA test setup, high speed 304L stainless steel projectiles (accelerated by a gas gun) were allowed to pass over the leading edge of the test configuration (a steel ring) and impact the fabric wound over the ring through a slot from the general direction of the center of the ring. The projectile impacted the specimen edge on. Impact and residual energy and fabric deformation for a number of different test conditions were reported. The energy absorbed was calculated from the change in velocity of the projectile. The test results demonstrated that aramids Kevlar and Zylon absorb 5 times more kinetic energy per weight than aluminum fuselage skin. These results also show that Zylon is

able to absorb almost three times more energy than Kevlar when compared on an overall weight basis.

Pereira, Roberts and Revilock conducted similar ballistic tests on Poly phenylene benzobizoxazole (PBO) and Kevlar 29 fabrics. T6 aluminum cylinders were used as projectiles that were accelerated using a compressed helium gas gun. These tests were conducted at elevated temperatures using quartz lamps as heat sources and simulated the impact of engine fragments in supersonic jet engines. The study concluded that unaged PBO had excellent energy absorption characteristics. At 260 °C (500 °F) it was able to absorb approximately 70 percent of the energy that the room temperature fabric could absorb. However, both at room temperature and at 260 °C (500 °F), it was significantly better than a similar weight Kevlar fabric.

In another related study, SRI International carried out yarn tensile tests and transverse load tests, to characterize the deformation and failure of individual fabric yarns. . The transverse loader tests show the effect of sharp penetrators and blunt cylindrical penetrators upon impact with the weave fabric. These tests showed that the two different penetrators result in rupture of yarns at the place of impact and in remote failure of the yarns respectively.

Softwall engine housings in aircrafts consist of number of fabric layers wound around an aluminum casing. Briscoe and Motamedi (1992) studied the ballistic impact characteristics of aramid fabrics considering the influence of interface friction between the fabric layers. The study showed that the interface frictional work dissipated at the filament--filament and yarn--yarn junctions is a critical factor in determining the static tensile yarn and (transverse) fabric stiffness. The changes in these static parameters are

considered to be the origin of the subtle changes observed in the ballistic performance of the corresponding fabrics.

The shear modulus of fabrics is an important variable in the finite element modeling of ballistic tests on dry aramid fabrics. A shear frame to study the shear response of fabrics was developed by Chen, Lussier, Cao and Peng (2002). Along with Liu (2002), they also conducted experimental and numerical analysis on normalization of picture frame tests (shear frame) for various composite materials.

1.3 Thesis Objective

The primary aim of this thesis is to experimentally obtain the independent material constants that have a large influence in the development of a robust finite element model simulating a softwall fan containment system. In this research, the main focus is on the following areas.

1) The modulus of elasticity, E, Poisson's Ratio, ν and shear modulus G of any material are directionally dependent. Because of symmetry, there are a total of nine independent material constants - E_1, E_2, E_3, G_{12}, G_{23}, G_{13}, ν_{12}, ν_{23}, and ν_{13}. The objective of this task is to perform the static tests (uniaxial tension tests) on fabric wraps to obtain the values of confirmed sensitive material constants of Kevlar and Zylon materials and thereby provide the data necessary for modeling woven Kevlar and Zylon warps.
2) Perform the experimental static testing (ring tests) of containment wraps subjected to loads through a blunt nose impactor (penetrator). A wide variation in the

location, orientation and geometry of the blunt nose impactor-to-fabric is to be implemented to assess the robustness of the material models and methodologies used in the FE quasi static simulations.

3) Perform experiments to determine the frictional coefficients between the individual fabric layers and understand the importance of the interlayer friction.
4) Investigate, develop and perform methodologies to measure in-plane shear response. Properties of primary interest from these tests include the mode of load transfer through reorientation, yarn slip, and shear locking in addition to the mode of failure under biaxial loading.

The details and the results of the standard tensile tests are explained in Chapter 2. Chapter three specifically deals with the static ring tests simulating the fan housing of an engine containment system. Chapter 4 discusses the friction tests and develops a material mechanics approach in predicting the load deflection curves of multi-ply static ring tests using the determined coefficients of friction. Details of the various shear tests conducted are explained in Chapter 5 and conclusions are outlined in Chapter 6.

Chapter 2: Simple Tension Tests

2.1 Introduction to the Tension Tests

The simple tension tests were conducted to evaluate the material constants for a particular type of fabric. Accordingly, these tests were performed on various fabric specimens of known dimensions. The obtained data were used in creating the stress-strain curves for the different fabrics. These curves can then be used as a basis for a material model suitable for use in a finite element analysis.

2.1.1 Objectives

The primary aim of these simple tension tests was to construct the stress-strain diagram up to ultimate failure in the warp and fill material directions for the Kevlar AS-49, Zylon AS-500 and Zylon AS-1500 fabrics. These diagrams were used to determine the Young's Modulii and Poisson's ratios for the fabrics.

2.1.2 Specimen Preparation Procedure

The specimens were custom made with their sides stitched or sides glued using the sergene greige method. The side stitched specimens and the sides glued specimens are represented as S1 and S2 respectively. The specimens using the two different methods for side stitching are shown in figures 2.1 and 2.2.

Figure 2.1: Kevlar Specimens (S1)

Figure 2.2: Kevlar Specimens (S2)

End Plates

In order to ensure that slipping of the specimens (from the grips) did not influence the deflection values, a different gripping fixture was used. Each fabric was tested with a new gripping fixture that is shown in figures 2.3 to 2.7. Flat steel plates 2.5" wide, 2" long, 0.25" thick are used to grip the specimen at both ends. At each end, one of the two pieces has a curved groove at the center of the plate throughout its width, which is half the thickness of the plate. The other plate has a V-notch cut in the same position about half the thickness of the plate. A round aluminum rod is cut along the length to the shape of the groove to match the existing grooves in the steel plate. Two shoulder pins are assembled at the top of the plates to keep the assembly intact and prevent any wobble of the plates with respect to each other about the aluminum piece. The fabric was held between the V-notch and the aluminum piece so that the notch pinches against the fabric and prevents from slipping with respect to the end plates. The two plates were pressed with hydraulic grips thereby ensuring uniform pressure application to minimize, if not

prevent, any fabric slipping. The revised grip assembly is denoted as Grip T2. Two specimens of each fabric type were tested with a new gripping fixture.

Figure 2.3: End plates for gripping

Figure 2.4: Side view

Figure 2.5: Inner view of the grip assembly

Clip Gage System

A clip gage system was designed to determine the displacement of the fabric. The primary part of the clip gage system consists of two rectangular wood buttons that are woven onto the fabric. Figure 2.6 shows the buttons used in the clip gage system. The top

button is fixed while the bottom button is allowed to move along the length of the aluminum rod. A calibrated extensometer fitted on the "button" measures the strain of the fabric for a particular extensometer gage length. Gage lengths varying from 1.2" to 3.2" can be adopted using this arrangement. The mass of the button apparatus along with the extensometer is 0.065 kg. The button is attached to the fabric using a high strength thread. Figure 2.7(a) illustrates the connection between the button and the fabric. Figure 2.7(b) shows the bond between the fabric and the button after the completion of a tension tests. The bond between the button apparatus and the fabric is strong enough for proper load transfer to take place. The experimental setup for a typical tension test using the clip gage system is shown in figure 2.8.

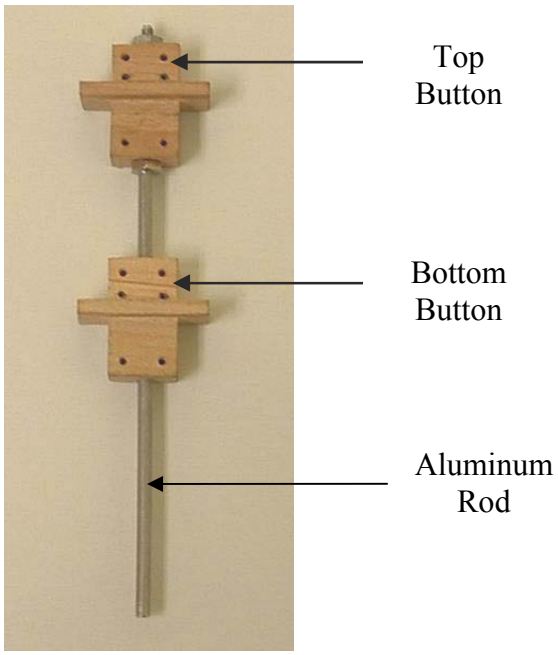

Figure 2.6: Button part of the clip gage system

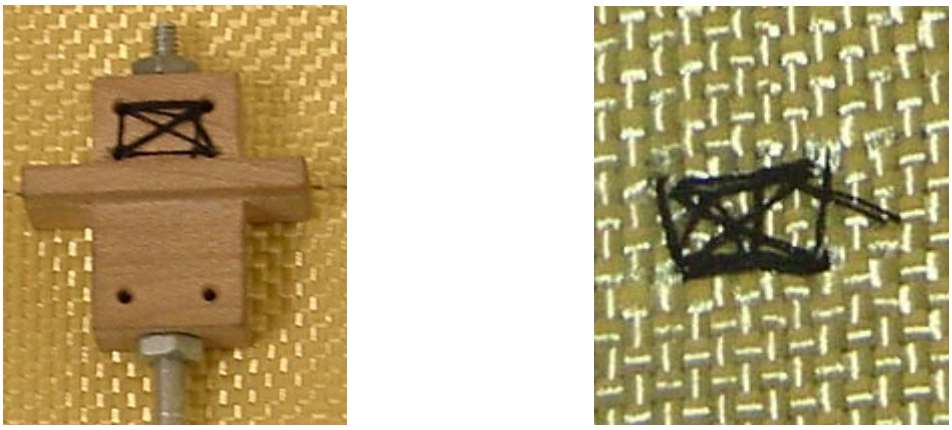

Figure 2.7: Button apparatus attached to the fabric (a) before testing and (b) after testing

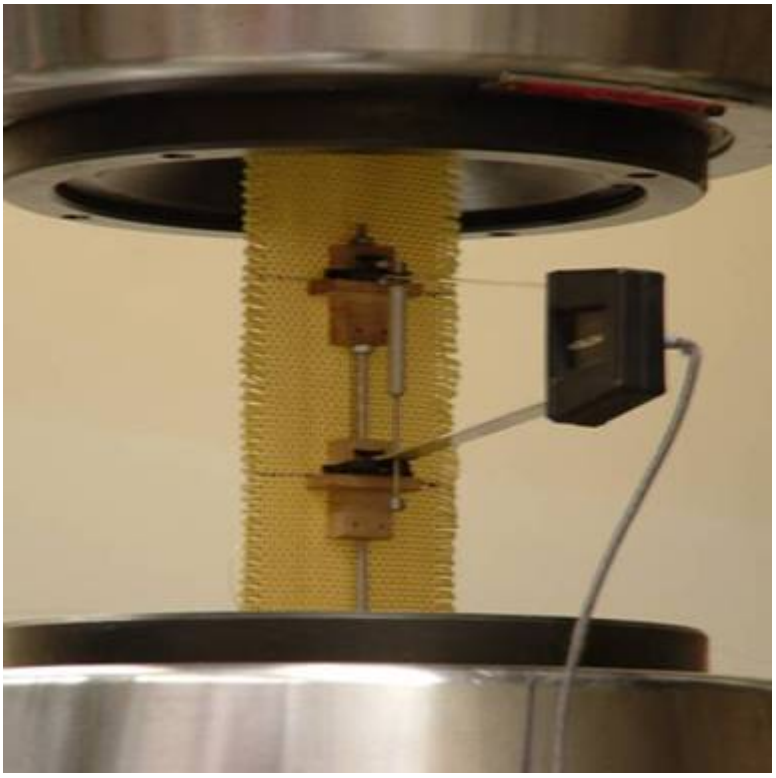

Figure 2.8: Experimental Setup using the clip gage system

2.1.3 Specimen Test Procedure

The tests were performed according to the Standard ASTM procedure – ASTM D 3039 *"Standard Test Method for Tensile Properties of Fiber-Resin Composites"*. Tests were conducted in a 22 Kips servo-hydraulic test frame operated under closed-loop control.

The test procedure included a displacement control test with the rate of displacement of actuator (stroke) set at 0.1"/min. Digital data acquisition was used to collect data at every 0.5 second. The test was continued until complete failure of the specimen was achieved. The load-deformation results were used to calculate the stress-strain response. The overall deformation of the specimen was measured by the stroke movement of the actuator.

Figure 2.9: Test setup with specimen

2.2 Test Procedure Validations

The tension tests provide the stress-strain curves for the various fabrics. Woven fabrics inherently have crimp (or waviness) and slack. In the initial stages of testing, the applied load essentially straightens the yarns of these fabrics by removing the crimp. Also, two different types of specimens namely S1 and S2 and various different gage lengths of the actuator and extensometer were used to plot these curves. A number of different tests were run in order to ascertain the effect of these parameters on the obtained results

2.2.1 Varying Gage Lengths

A number of tests were run to analyze the affect of different extensometer and actuator gage lengths on the tension tests results. Table 2.1 provides the details of various samples tested.

The following notations are used for the gage lengths of the actuator and extensometer.

L1 = Center-to-center distance between the two V-notches of the grip

L2 = Center-to-center distance between the centers of the button holes in the top portion of the two buttons.

Table 2.1: Test Details

Sample Name	Sample Type
A1	9" Actuator Gage Length; 1.2" Extensometer Gage Length
A2	9" Actuator Gage Length; 2.0" Extensometer Gage Length
A3	9" Actuator Gage Length; 3.2" Extensometer Gage Length
B1	12" Actuator Gage Length; 1.2" Extensometer Gage Length
B2	12" Actuator Gage Length; 2.0" Extensometer Gage Length
B3	12" Actuator Gage Length; 3.2" Extensometer Gage Length
C1	12” Actuator Gage Length (Pre-Loaded Sample); No extensometer
C2	9” Actuator Gage Length (Pre-Loaded Sample); 2.0" Extensometer Gage Length

A typical load–displacement plot (Figure 2.10) shows that actuator displacement measured is much greater than the extensometer displacement measured. Figure 2.11 shows a typical stress-strain curve.

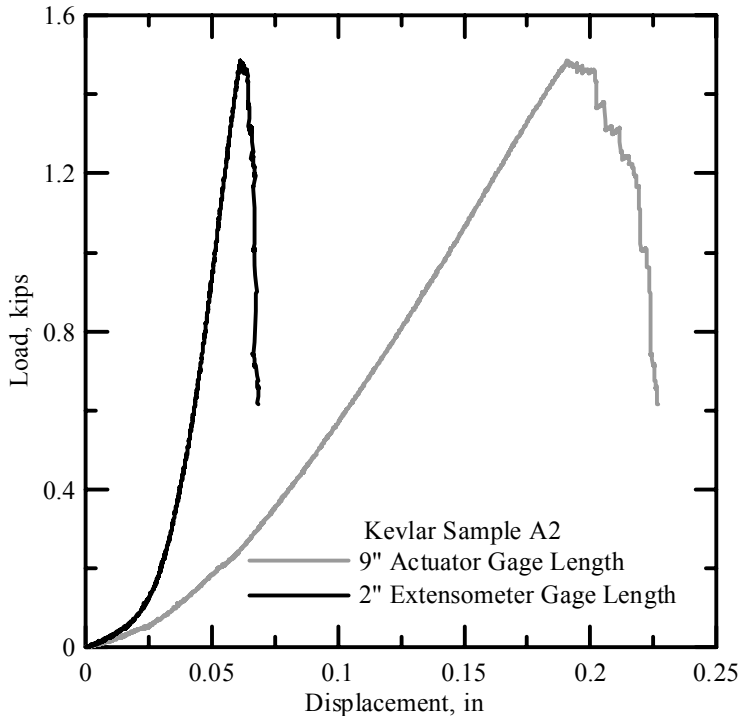

Figure 2.10: Load–displacement plot (Sample A2) using actuator stroke & extensometer reading

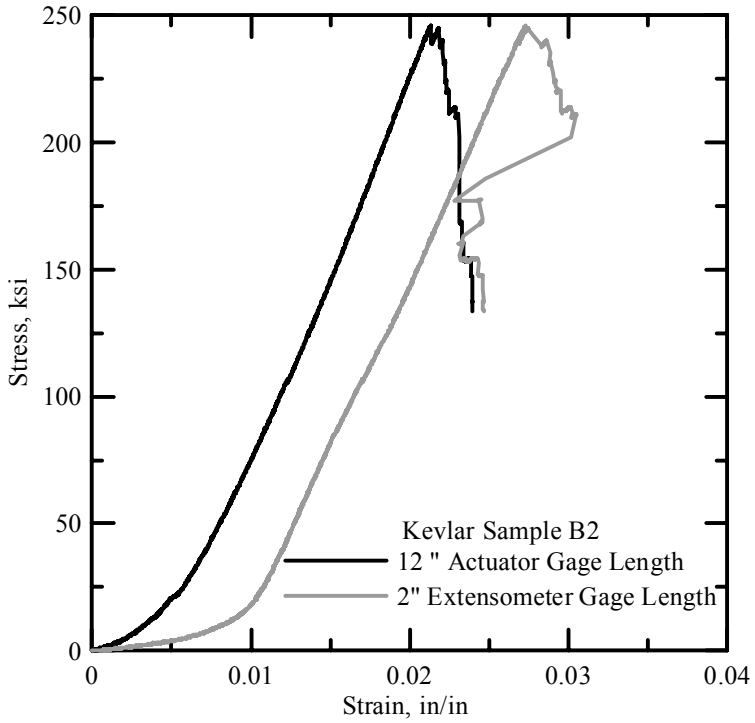

Figure 2.11: Stress-strain plot using actuator & extensometer strain (Sample B2)

It was observed that the stress strain curve obtained from the actuator displacement readings is similar to the curve obtained from extensometer displacement readings. The decrease in the strain values in the post-peak range of the extensometer stress strain curve can be attributed to the failure of the sample occurring along the gage length of the extensometer. The obtained graph also shows that the slope of the stress strain curve obtained from the extensometer readings is slightly higher than that obtained from the actuator readings in the pre-peak range. This difference was clearly indicated by the values of stiffness obtained from the actuator strain readings and extensometer strain readings. It was also seen that the effect of slack and crimp is more prominent in the extensometer readings than the actuator readings. Figures 2.13(a) and (b) show the stress–strain plots for all samples, obtained using the actuator and extensometer readings.

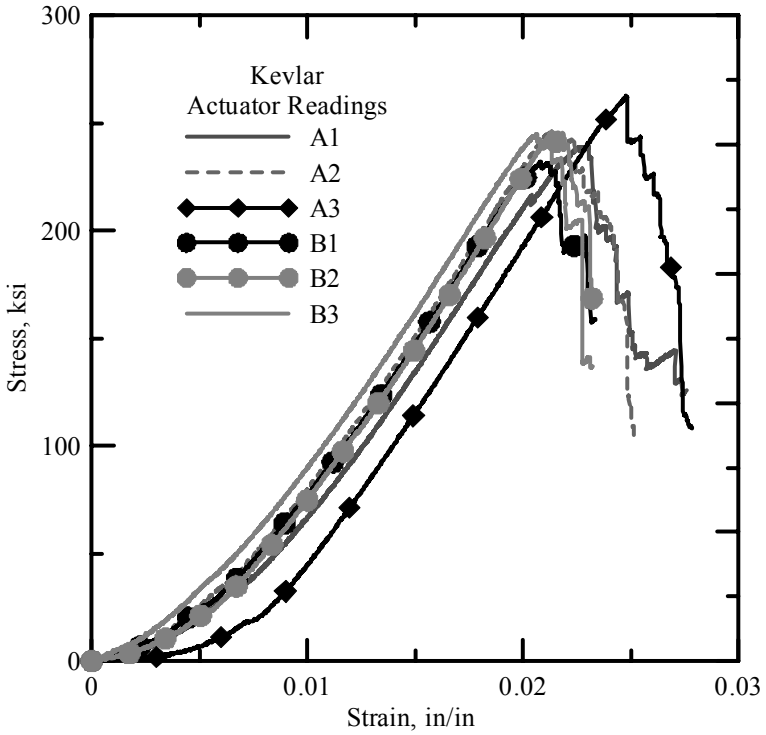

Figure 2.13(a): Stress-Strain Response with Actuator Readings

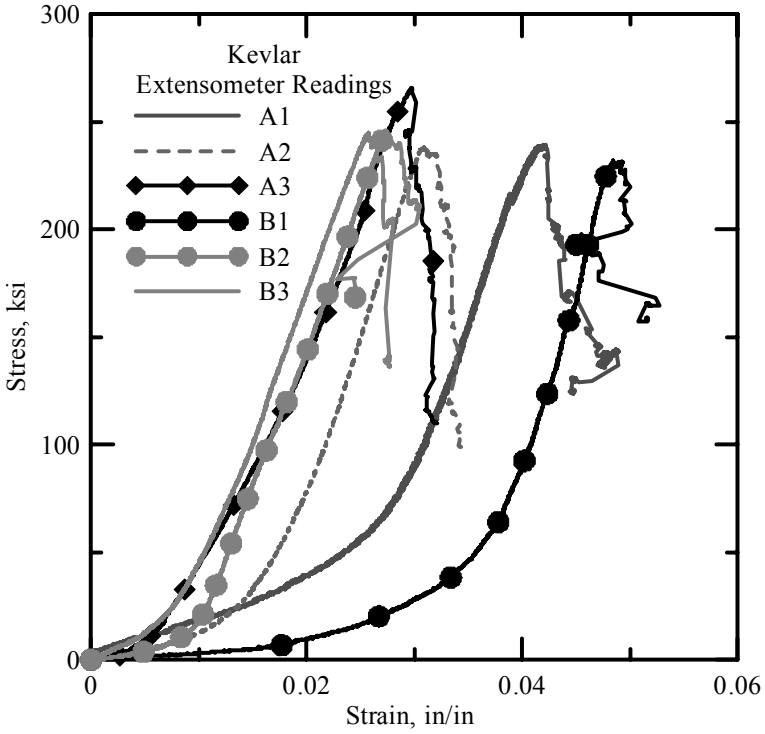

Figure 2.13(b): Stress-Strain Response with Extensometer Readings

Some of the differences in the initial part of the stress strain curves for the different samples (A & B) with different extensometer gage lengths (1.2", 2" and 3.2") can be attributed to the different levels of slack and crimp in each sample. The results are summarized in Table 2.2.

Table 2.2: Kevlar Test Results

	Sample Type	**Maximum Stress (ksi)**	**Actuator Readings**		**Stiffness, E ksi**	
			Maximum Ult. Strain (in/in)	**Toughness (ksi)**	Extensometer	Actuator
	A1	240.41	0.0178	2.92	14942.11	13412.77
	A2	247.22	0.0174	2.89	15287.93	13172.24
	A3	263.04	0.0185	3.00	14100.61	13071.31
Average		250.22	0.0179	2.94	**14776.9**	**13218.8**
Std. Dev		11.61	0.0006	0.05	610.7	175.4
	B1	233.38	0.0168	2.41	14926.76	12961.50
	B2	247.09	0.0171	2.55	14426.71	13132.65
	B3	245.42	0.0170	2.47	14715.12	12800.05
Average		241.96	0.0170	2.48	**14689.5**	**12964.7**
Std. Dev		7.48	0.0002	0.07	251.0	166.3

2.2.2 Cyclic Load Tests

The phenomenon of pre-loading the test specimen was used to study the effect of the slack and crimp. The specimen was subjected to cyclic loading between 0-0.1 kips applied at 100 cycles with a frequency of 1 Hz. This loading was applied to the specimen before the specimen is subjected to the actual loading. Figure 2.14 shows the effect of this cyclic preloading. The control sample was not preloaded and shows the presence of slack and crimp visible at the initial portion of the graph (Control Sample Original B1). By computing the largest slope (corresponding to the largest stiffness of the specimen), one can slide the graph so that the largest slope passes through the origin. This graph was denoted as Control Sample Linearized. The same procedure was applied to the sample that is preloaded (Sample C1). The amount of sliding that was required is greatly reduced indicating that very little slack and crimp was present in the specimen.

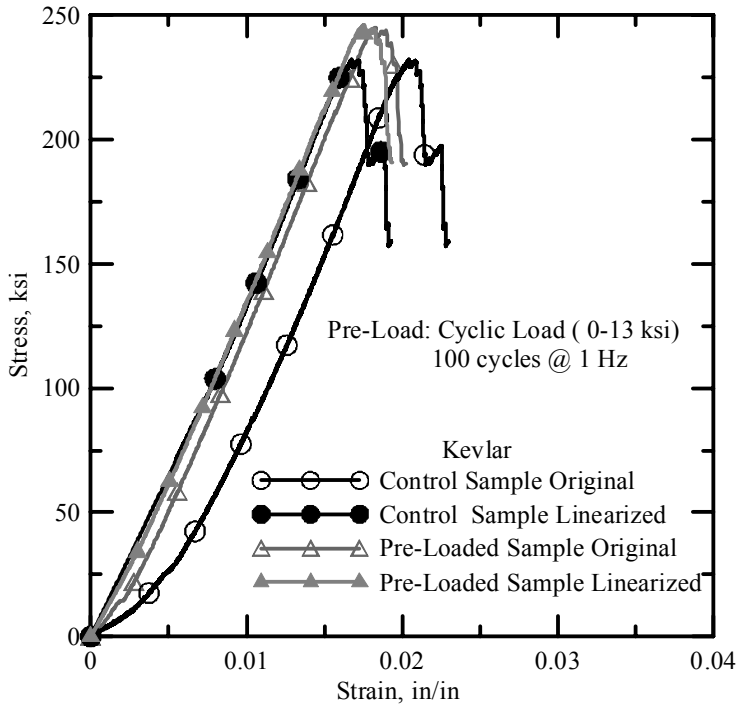

Figure 2.14: Stress–strain plots with (Sample C1) and without pre-loading (Sample B1)

Samples C1 and B1 were tested without the extensometer assembly attached to the sample. A cyclic load test performed on Kevlar sample C2 of size 9” actuator gage length and 2” extensometer gage length is shown in the figure 2.15 below.

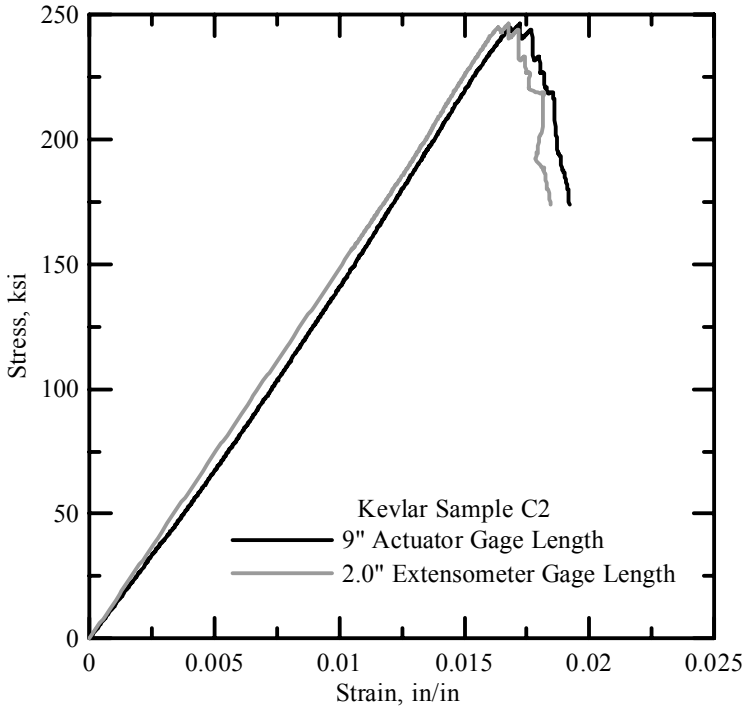

Figure 2.15: Stress–Strain plots with pre-loading (Sample C2)

The stiffness obtained for the above sample is compared to a similar sample A2 (without pre-loading) in Table 2.3.

Table 2.3: Stiffness and Ultimate Strains With and Without Preloading

	Stiffness, E, ksi		Max Ult. Strain (in/in)	
	Extensometer	Actuator	Extensometer	Actuator
Without Preloading (Sample A2)	15288	13172	0.031	0.021
With Preloading (Sample C2)	15109	13232	0.016	0.017

The values of the stiffness obtained for a sample with and without preloading are similar to each other. Thus, pre-loading of the sample only eliminates the slack and crimp present in the initial portion of the stress strain curve. However, there is a significant difference in the ultimate strain values for the extensometer readings. Hence, the cyclic load test may be employed for samples that require an accurate calculation of the ultimate strain values.

2.2.3 Stitched and Glued Samples

Stitched and glued samples were used in the test program. Figures 2.16 and 2.17 show the tension tests results for stitched and glued samples for Kevlar and Zylon AS-500. Table 2.4 depicts the comparison of the values of the Young's modulii obtained using the stitched and glued samples for the two fabrics. Table 2.4 indicates that there is no significant difference in the Young's Modulii E_{11} for the two fabrics using the stitched and glued samples. Hence, both samples S1 and S2 can be used to the determine the material constants for the fabrics

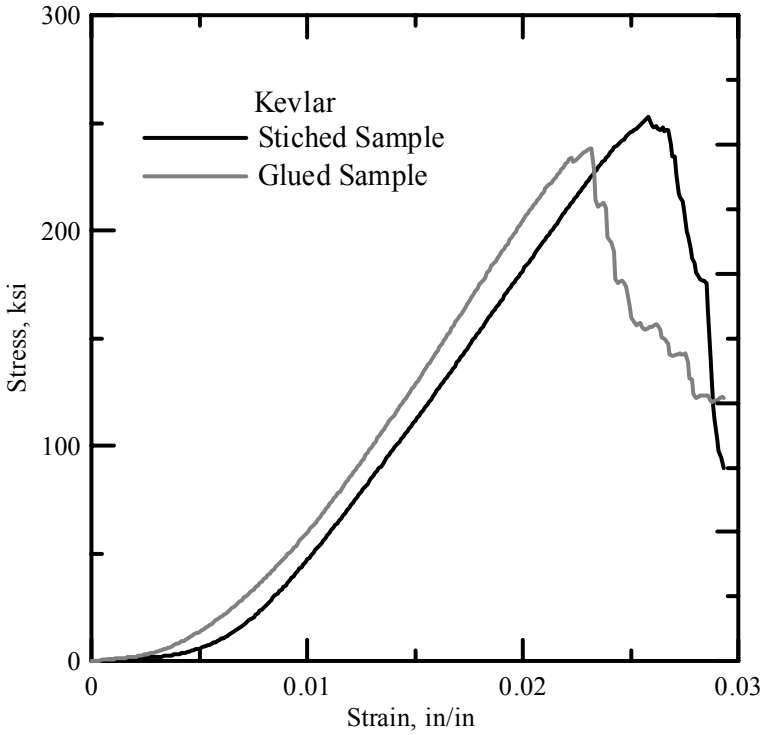

Figure 2.16 Stress–Strain Comparisons for Stitched and Glued Samples for Kevlar

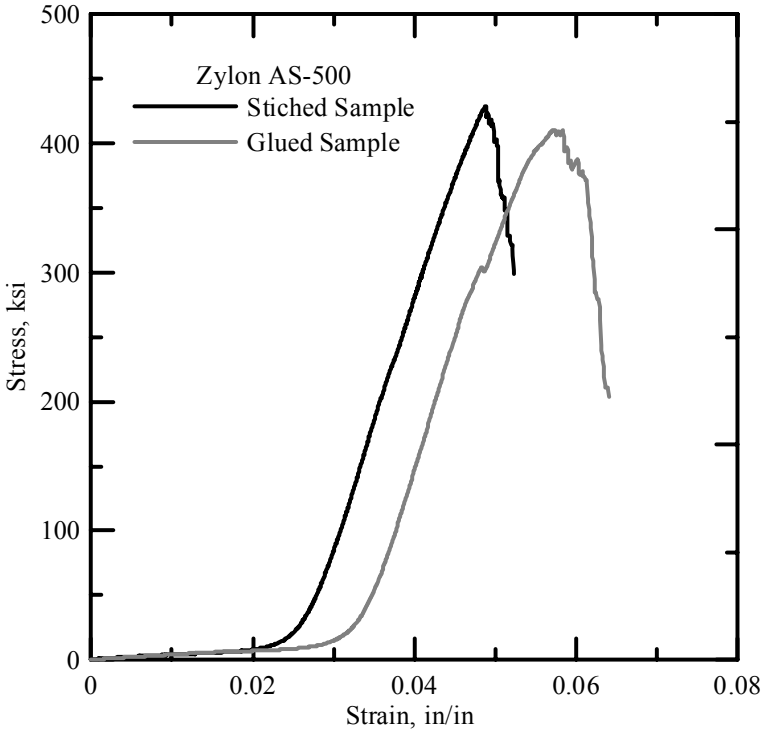

Figure 2.17: Stress–Strain Comparisons for Stitched & Glued Samples for Zylon AS-500

Table 2.4: Young's Modulus Comparison for Stitched and Glued Samples for Different Fabrics

Fabric	Young's Modulus E_{11}, MPa	
	Stitched	Glued
Kevlar	13232	13326
Zylon AS-500	19319	19421

2.3 Tension Test Results

Simple tension tests were run on the three types of fabrics using the 22 Kips servo-hydraulic test frame operated under closed-loop control. The clip gage system was attached perpendicular to the direction of the actuator displacement for measuring the Poisson's ratio for the fabric. For each type of fabric, a total of ten samples were tested, five in the fill direction and five in the warp direction. The Poisson's ratio was calculated for three different ranges as the ratio of lateral stiffness to longitudinal stiffness.

2.3.1 Kevlar Tension Tests

The following are the results of the tension tests carried out on Kevlar samples for determining Young's Modulus E_{11}. Figure 2.18 shows the stress-strain response of five Kevlar samples. Table 2.5 summarizes these results.

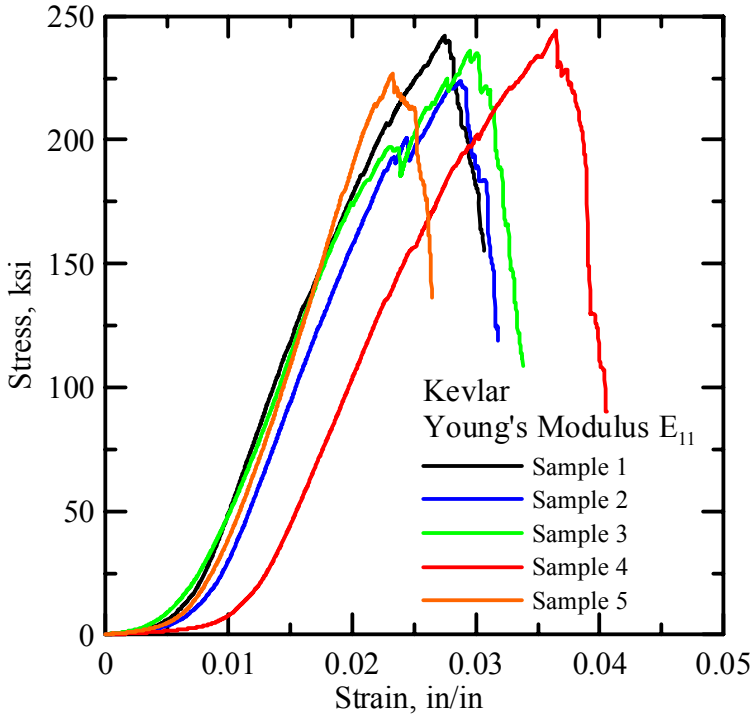

Figure 2.18: Stress-Strain Curves for the Kevlar Samples for E_{11}

Table 2.5: Tension Test Results From Kevlar Samples for E_{11}

	Sample Type	Maximum Stress ksi	Maximum Ult. Strain in/in	Toughness ksi	Stiffness, E ksi
	1	241.99	0.0274	3.52	13608.58
	2	223.93	0.0287	3.27	13187.96
	3	235.96	0.0295	4.01	13525.44
	4	244.32	0.0365	4.24	13154.00
	5	227.41	0.0319	3.73	13380.51
Average		234.72	0.03	3.75	13371.30
Std. Dev		8.90	0.00	0.39	200.61

The Poisson's Ratio ν_{12} for Kevlar was obtained from the tension tests using the clip gauge system. The following graphs (Figures 2.19 and 2.20) show the axial stress versus lateral strain for these samples.

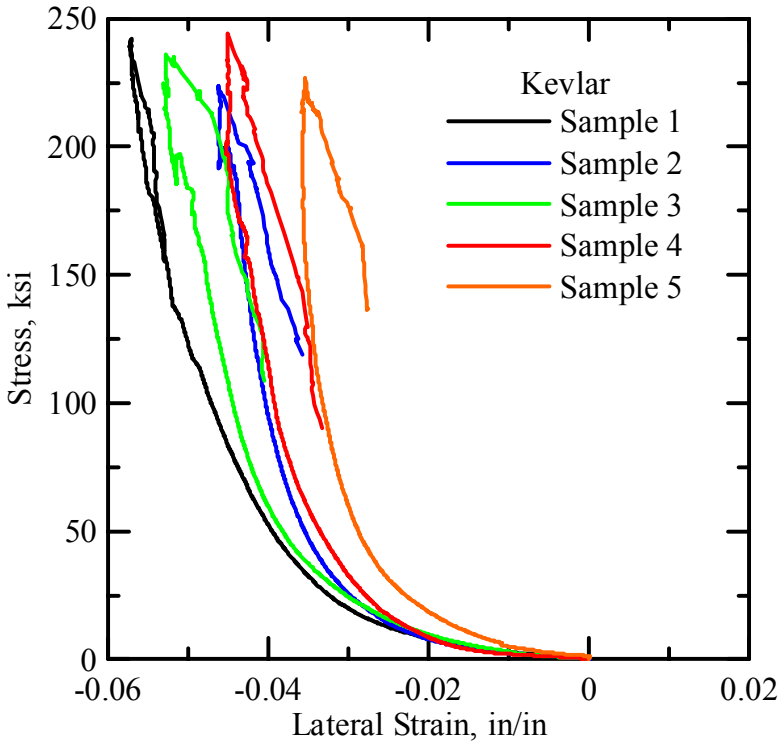

Figure 2.19: Axial Stress Versus Lateral Strains for Kevlar Samples for ν_{12}

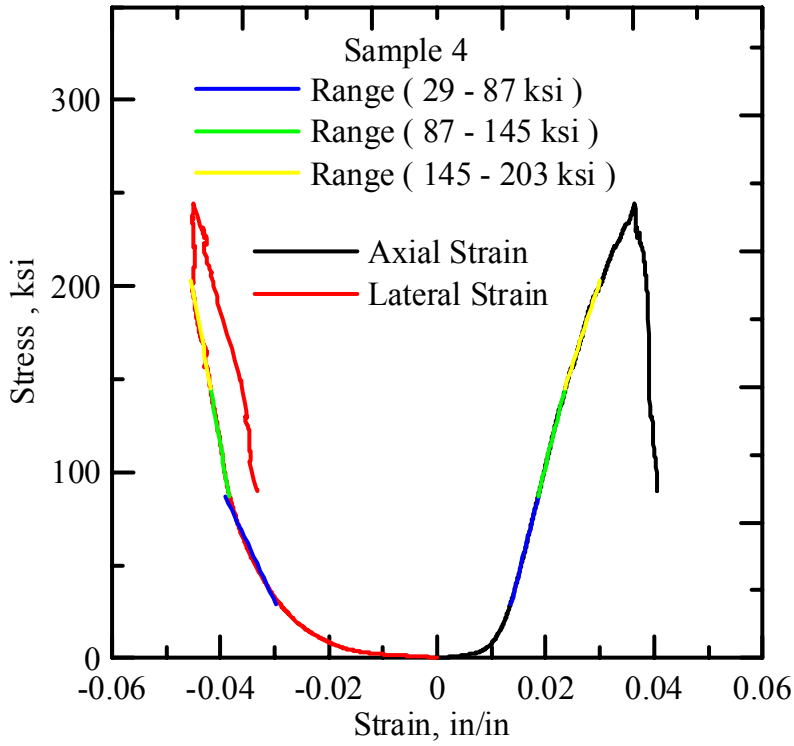

Figure 2.20: Axial Stress Versus Axial Strain and Lateral Strain for Sample 4 for ν_{12}

The Poisson's Ratio ν_{12} was calculated for three different ranges of stresses and the results are summarized in table 2.6.

Table 2.6: Poisson's ratio ν_{12} for the Kevlar Samples

Stress Range	**Poisson's Ratio**						
	Sample 1	Sample 2	Sample 3	Sample 4	Sample 5	Average	Std. Dev
29-87 ksi	1.945	1.746	1.921	1.842	1.764	1.844	0.090
87-145 ksi	0.797	0.680	0.746	0.685	0.615	0.705	0.069
145-203 ksi	0.738	0.524	0.618	0.578	0.631	0.618	0.079

The results obtained from five tension tests run on Kevlar AS-49 for Young's Modulus E_{22} are shown in the figure 2.21 and table 2.7.

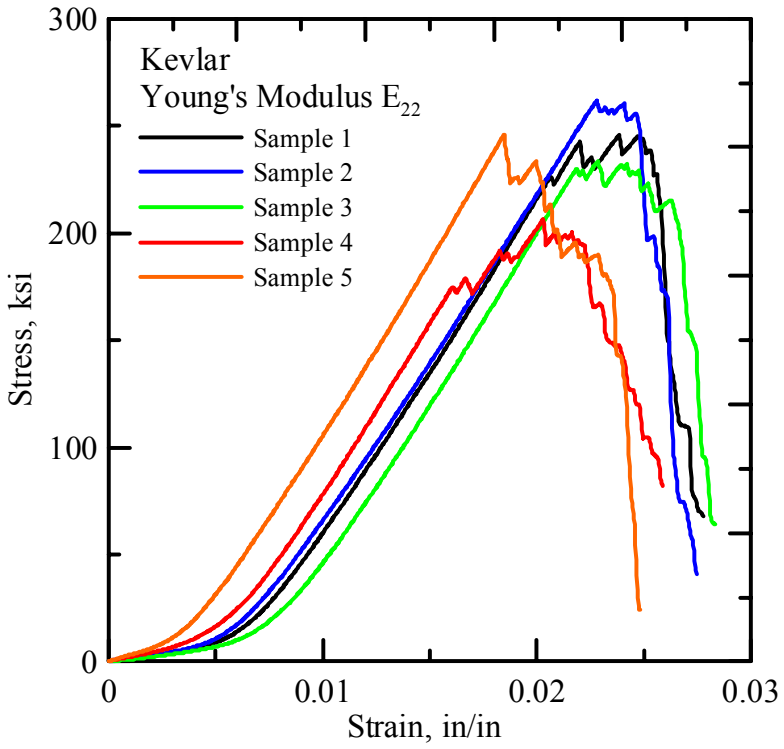

Figure 2.21: Stress-Strain Curves for the Kevlar As-49 Samples for E_{22}

Table 2.7: Tension Test Results From Kevlar Samples for E_{22}

	Sample Type	Maximum Stress ksi	Maximum Ult. Strain in/in	Toughness ksi	Stiffness, E ksi
	1	245.82	0.0238	3.11	15136.68
	2	261.73	0.0228	3.15	15013.68
	3	233.39	0.0228	3.01	15378.25
	4	206.35	0.0203	2.68	15154.16
	5	245.95	0.0185	3.04	15736.76
Average		238.65	0.02	3.00	15283.91
Std. Dev		20.67	0.00	0.19	285.27

The Poisson's Ratio ν_{21} for Kevlar AS-49 was obtained from the tension tests using the clip gauge system. The following graphs (Figures 2.22 and 2.23) show the axial stress versus lateral strain for these samples.

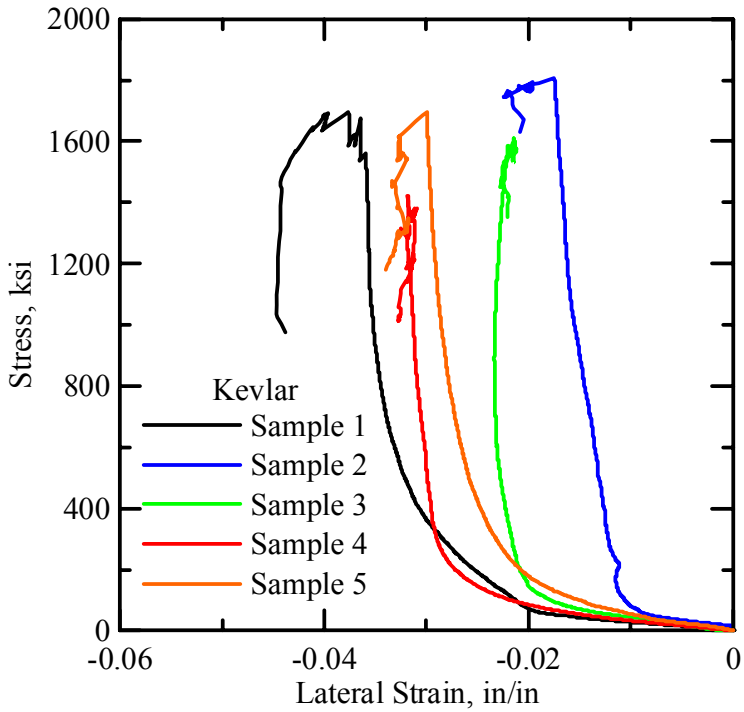

Figure 2.22: Axial Stress Versus Lateral Strains for Kevlar AS-49 Samples for ν_{21}

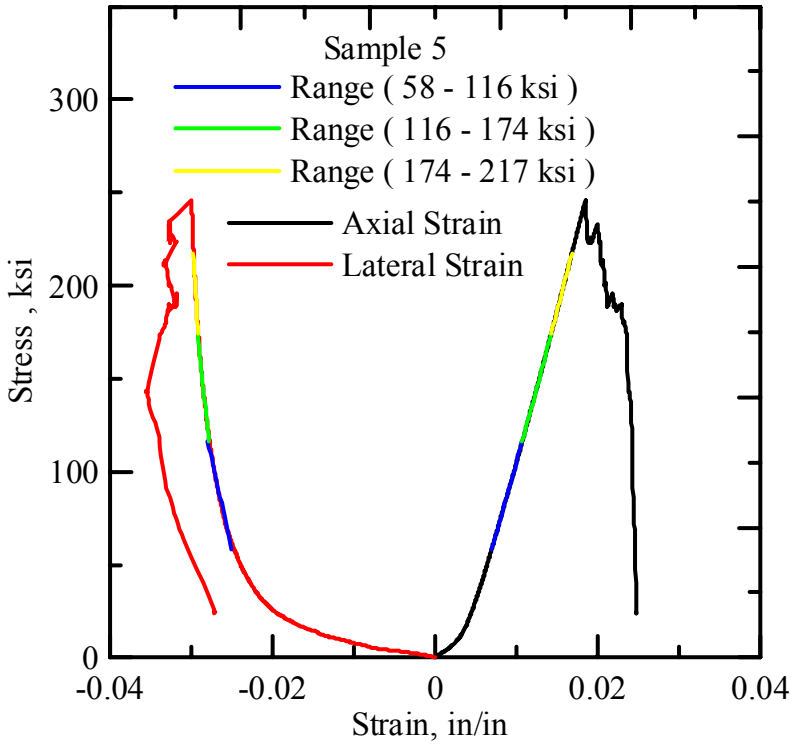

Figure 2.23: Axial Stress Versus Axial Strain and Lateral Strain for Sample 5 for ν_{21}

The Poisson's Ratio ν_{21} was calculated for three different ranges of stresses and the results are summarized in Table 2.8

Table 2.8: Poisson's Ratio ν_{21} For the Kevlar AS-49 Samples

Stress Range	**Poisson's Ratio**						
	Sample 1	Sample 2	Sample 3	Sample 4	Sample 5	Average	Std. Dev
58-116 ksi	0.828	0.802	0.290	0.350	0.786	0.611	0.267
116-174 ksi	0.302	0.345	-0.110	0.182	0.391	0.222	0.201
174-217 ksi	0.211	0.256	-0.261	0.000	0.231	0.087	0.220

2.3.2 Zylon AS-500 Tension Tests

The results obtained from five tension tests run on Zylon AS-500 for Young's Modulus E_{11} are shown in the figure 2.24 and table 2.9.

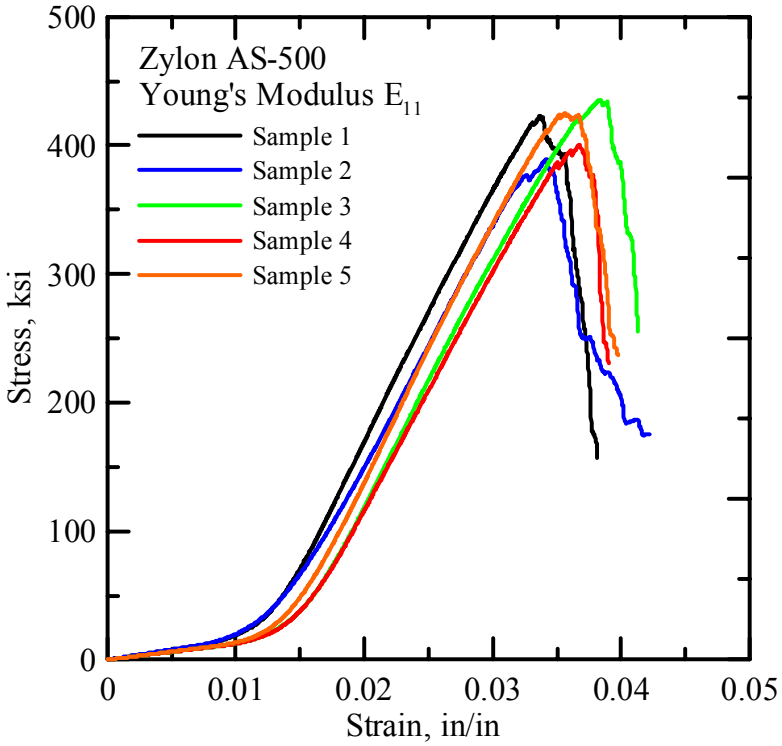

Figure 2.24: Stress-Strain Curves for the Zylon As-500 Samples for E_{11}

Table 2.9: Tension Test Results Zylon AS-500 Samples for E_{11}

	Sample Type	Maximum Stress ksi	Maximum Ult. Strain in/in	Toughness ksi	Stiffness, E ksi
	1	423.21	0.0337	6.49	19672.93
	2	445.82	0.0365	6.92	19930.00
	3	400.70	0.0368	5.80	18613.02
	4	425.37	0.0356	6.70	19217.05
	5	435.37	0.0384	6.99	19115.51
Average		426.09	0.04	6.58	19309.70
Std. Dev		16.80	0.00	0.48	511.95

The Poisson's Ratio ν_{12} for Zylon AS-500 was obtained from the tension tests using the clip gauge system. The following graphs (Figures 2.25 and 2.26) show the axial stress versus lateral strain for these samples.

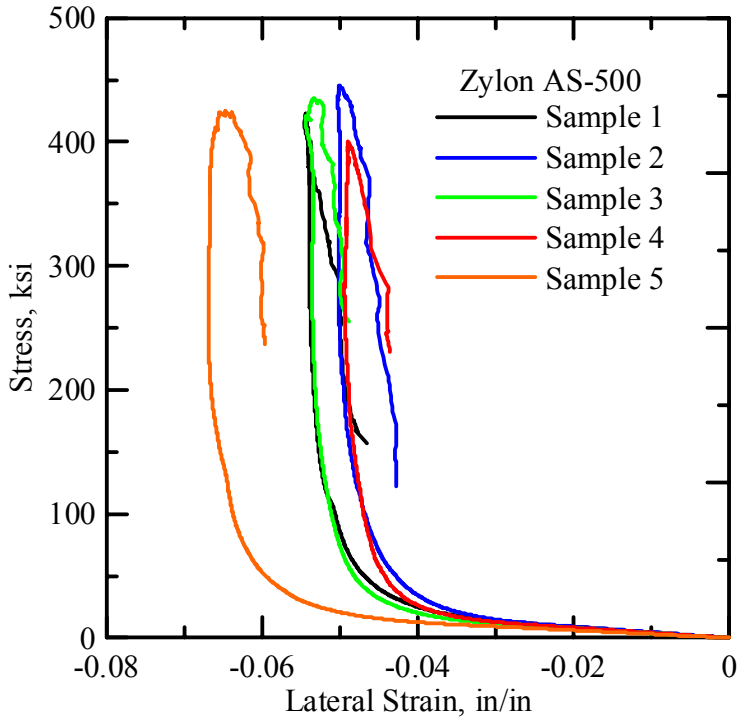

Figure 2.25: Axial Stress Versus Lateral Strains for Zylon AS-500 Samples for ν_{12}

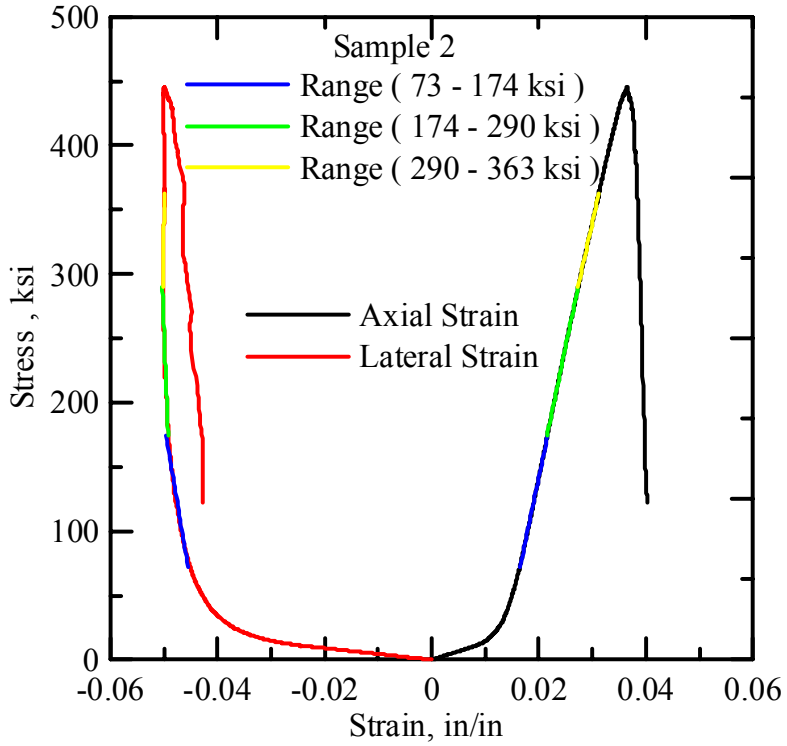

Figure 2.26: Axial Stress Versus Axial Strain and Lateral Strain for Sample 2 for ν_{12}

The Poisson's Ratio ν_{12} was calculated for three different ranges of stresses and the results are summarized in Table 2.10

Table 2.10: Poisson's Ratio ν_{12} For the Zylon AS-500 Samples

Stress Range	**Poisson's Ratio**						
	Sample 1	Sample 2	Sample 3	Sample 4	Sample 5	Average	Std. Dev
73-174 ksi	0.822	0.793	0.486	0.718	0.560	0.676	0.147
174-290 ksi	0.147	0.186	0.130	0.173	0.122	0.152	0.027
290-363 ksi	0.033	0.044	0.056	0.070	0.056	0.052	0.014

The results obtained from five tension tests run on Zylon AS-500 for Young's Modulus E_{22} are shown in the figure 2.27 and table 2.11.

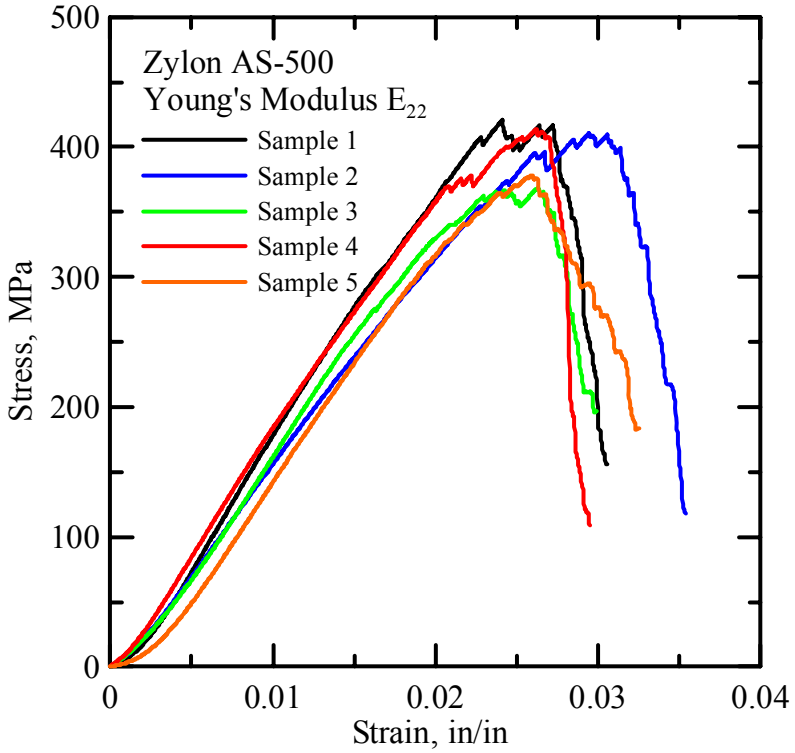

Figure 2.27: Stress-Strain Curves for the Zylon As-500 Samples for E_{22}

Table 2.11: Tension Test Results Zylon AS-500 Samples for E_{22}

	Sample Type	Maximum Stress ksi	Maximum Ult. Strain in/in	Toughness ksi	Stiffness, E ksi
	1	420.69	0.0241	7.37	19730.82
	2	410.31	0.0294	8.47	18910.97
	3	368.40	0.0263	6.49	19174.01
	4	413.91	0.0262	6.93	19717.47
	5	378.15	0.0260	6.90	19274.66
Average		398.29	0.0264	7.23	19361.59
Std. Dev		23.40	0.0019	0.76	356.65

The Poisson's Ratio ν_{21} for Zylon AS-500 was obtained from the tension tests using the clip gauge system. The following graphs (Figures 2.28 and 2.29) show the axial stress versus lateral strain for these samples.

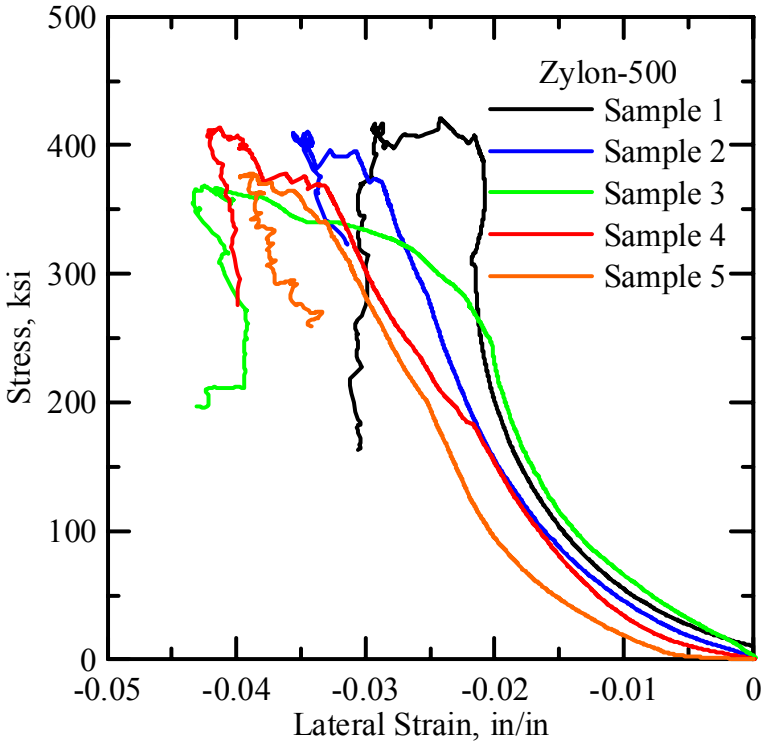

Figure 2.28: Axial Stress Versus Lateral Strains for Zylon AS-500 Samples for ν_{21}

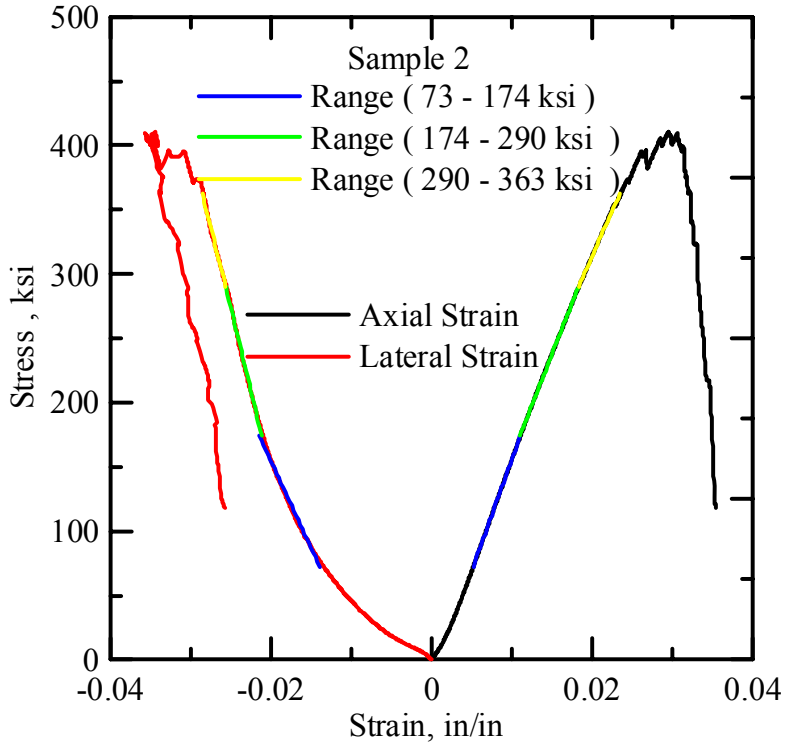

Figure 2.29: Axial Stress Versus Axial Strain and Lateral Strain for Sample 2 for ν_{21}

The Poisson's Ratio ν_{21} was calculated for three different ranges of stresses and the results are summarized in Table 2.12

Table 2.12: Poisson's Ratio ν_{21} For the Zylon AS-500 Samples

Stress Range	**Poisson's Ratio**						
	Sample 1	Sample 2	Sample 3	Sample 4	Sample 5	Average	Std. Dev
73-174 ksi	1.434	1.280	1.295	1.357	1.101	1.293	0.124
174-290 ksi	0.724	0.613	0.711	0.961	0.801	0.762	0.130
290-363 ksi	0.482	0.564	1.583	0.785	0.671	0.817	0.443

2.3.3 Zylon AS-1500 Tension Tests

Figure 2.30 shows the stress-strain response of five Zylon AS-1500 samples for a loading rate of 0.2 inches per minute. Table 2.13 summarizes these results.

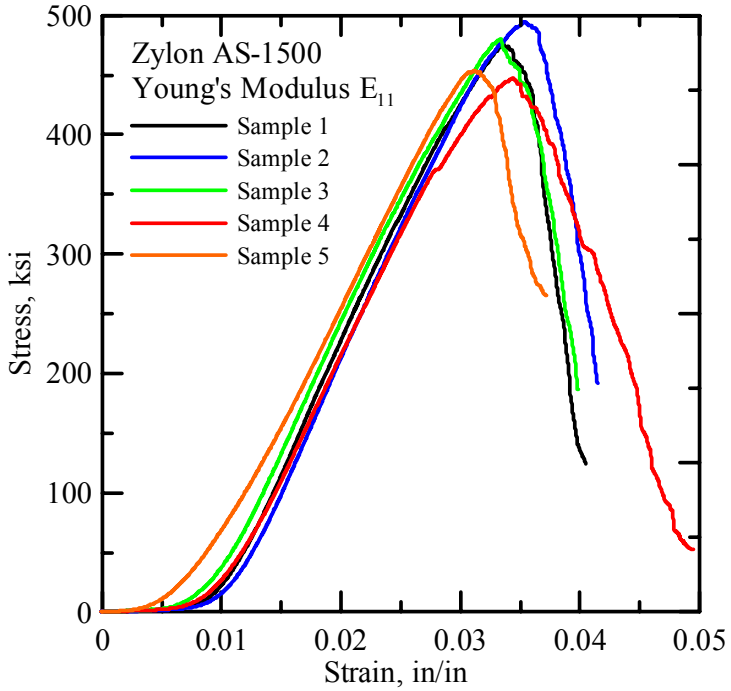

Figure 2.30: Stress-Strain Curves for the Zylon AS-1500 Samples for E_{11}

Table 2.13: Tension Test Results Zylon AS-1500 Samples for E_{11}

	Sample Type	Maximum Stress ksi	Maximum Ult. Strain in/in	Toughness ksi	Stiffness, E ksi
	1	476.49	0.0337	8.45	21477.55
	2	494.80	0.0365	9.09	22062.84
	3	477.20	0.0368	8.80	21895.82
	4	447.86	0.0356	10.11	21111.46
	5	453.51	0.0384	8.02	21534.49
Average		469.97	0.04	8.89	21616.43
Std. Dev		19.18	0.00	0.79	373.61

The Poisson's Ratio ν_{21} for Zylon AS - 1500 was obtained from the tension tests using the clip gauge system. The following graphs (Figures 2.31 and 2.32) show the axial stress versus lateral strain for these samples.

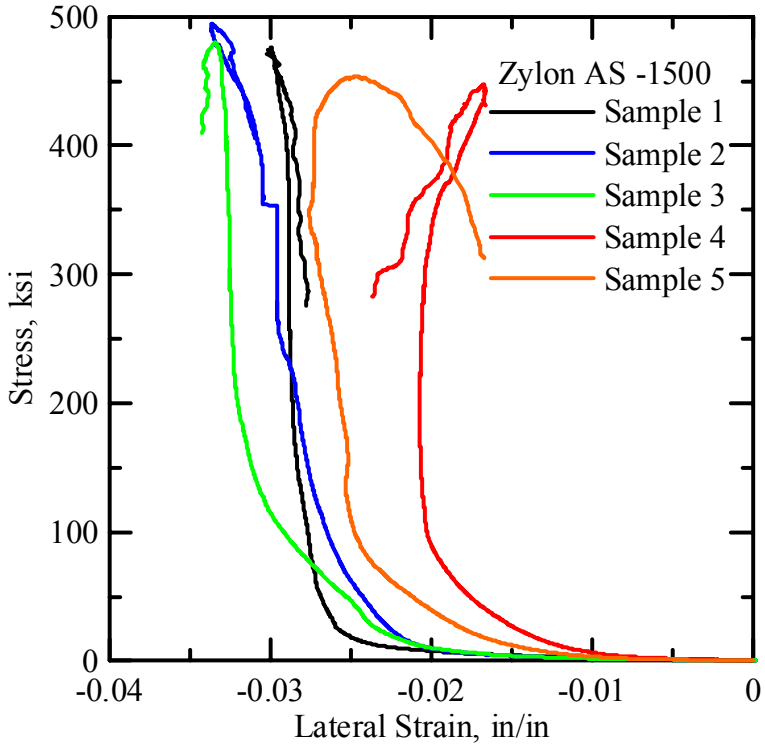

Figure 2.31: Axial Stress Versus Lateral Strains for Zylon As-1500 Samples for ν_{12}

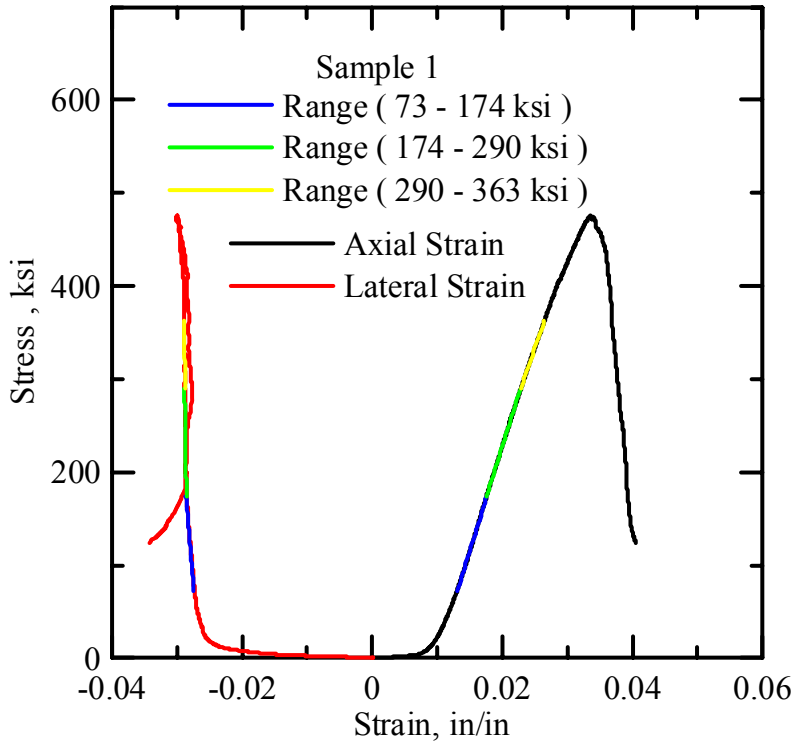

Figure 2.32: Axial Stress Versus Axial Strain and Lateral Strain for Sample 2 for ν_{12}

The Poisson's Ratio ν_{12} was calculated for three different ranges of stresses and the results are summarized in Table 2.14

Table 2.14: Poisson's Ratio ν_{12} For the Zylon As-1500 Samples

Stress Range	**Poisson's Ratio**						
	Sample 1	Sample 2	Sample 3	Sample 4	Sample 5	Average	Std. Dev
73-174 ksi	0.467	0.552	0.720	0.309	0.469	0.503	0.150
174-290 ksi	0.261	0.466	0.159	-0.053	0.244	0.215	0.188
290-363 ksi	0.014	0.384	0.041	-0.280	0.260	0.084	0.255

The results obtained from five tension tests run on Zylon AS-1500 for Young's Modulus E_{22} are shown in the figure 2.33 and table 2.15.

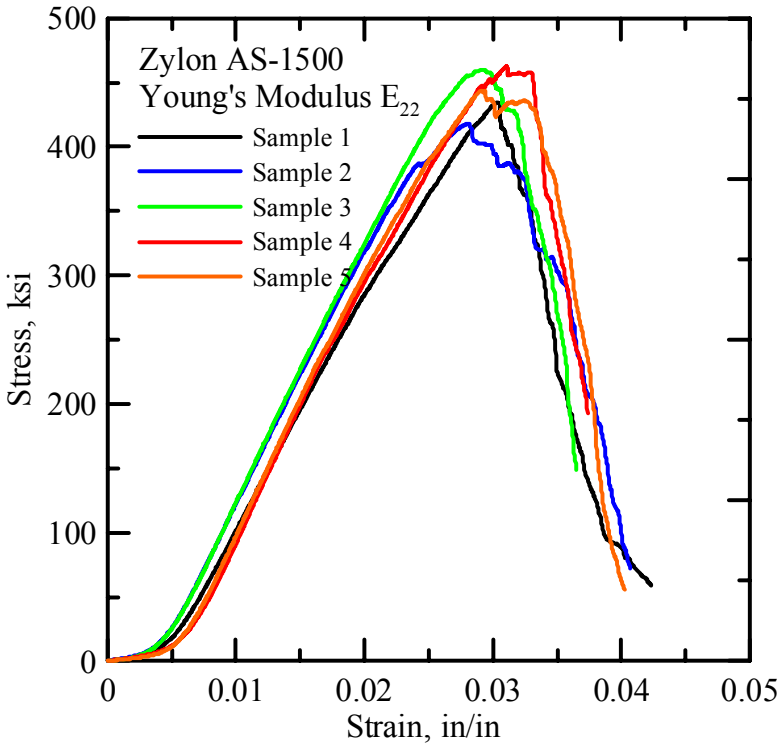

Figure 2.33: Stress-Strain Curves for the Zylon AS-500 Samples for E_{22}

Table 2.15: Tension Test Results Zylon AS-1500 Samples for E_{22}

	Sample Type	Maximum Stress ksi	Maximum Ult. Strain in/in	Toughness ksi	Stiffness, E ksi
	1	434.65	0.0303	8.53	20944.24
	2	418.19	0.0281	9.32	21136.55
	3	460.32	0.0293	8.96	21451.08
	4	462.63	0.0311	8.77	21595.03
	5	443.91	0.0291	9.28	21403.10
Average		443.94	0.0296	8.97	21306.00
Std. Dev		18.48	0.0012	0.34	261.53

The Poisson's Ratio ν_{21} for Zylon AS-1500 was obtained from the tension tests using the clip gauge system. The following graphs (Figures 2.34 and 2.35) show the axial stress versus lateral strain for these samples.

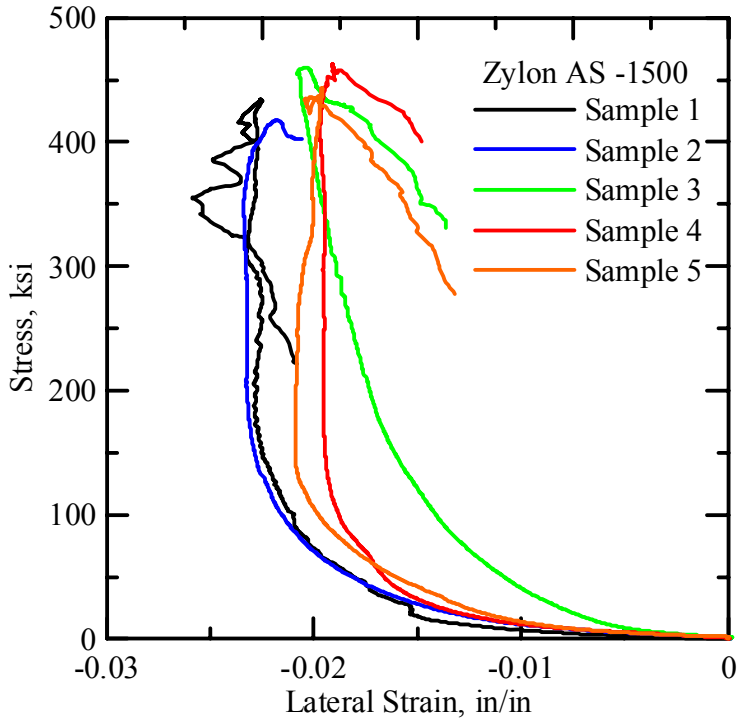

Figure 2.34 Axial Stress Versus Lateral Strains for Zylon AS-1500 Samples for ν_{21}

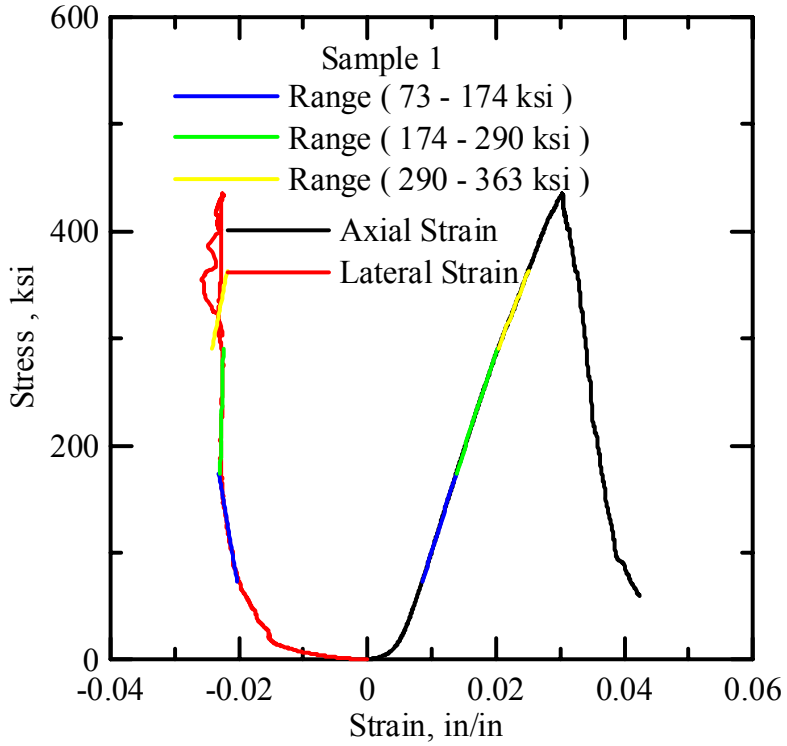

Figure 2.35: Axial Stress Versus Axial Strain and Lateral Strain for Sample 1 for ν_{21}

The Poisson's Ratio ν_{21} was calculated for three different ranges of stresses and the results are summarized in Table 2.16

Table 2.16: Poisson's Ratio ν_{21} For the Zylon AS-500 Samples

Stress Range	**Poisson's Ratio**						
	Sample 1	Sample 2	Sample 3	Sample 4	Sample 5	Average	Std. Dev
73-174 ksi	0.526	0.539	0.700	0.356	0.501	0.525	0.122
174-290 ksi	0.095	0.079	0.315	0.090	0.156	0.147	0.098
290-363 ksi	0.076	0.035	0.231	0.057	0.064	0.093	0.079

2.4 Comparison of All Fabrics

A comprehensive graph showing all the stress-strain curves for all the fabrics tested in this phase of the research is presented in figure 2.36. The samples used in the graph are the samples for E_{11} tests for all fabrics.

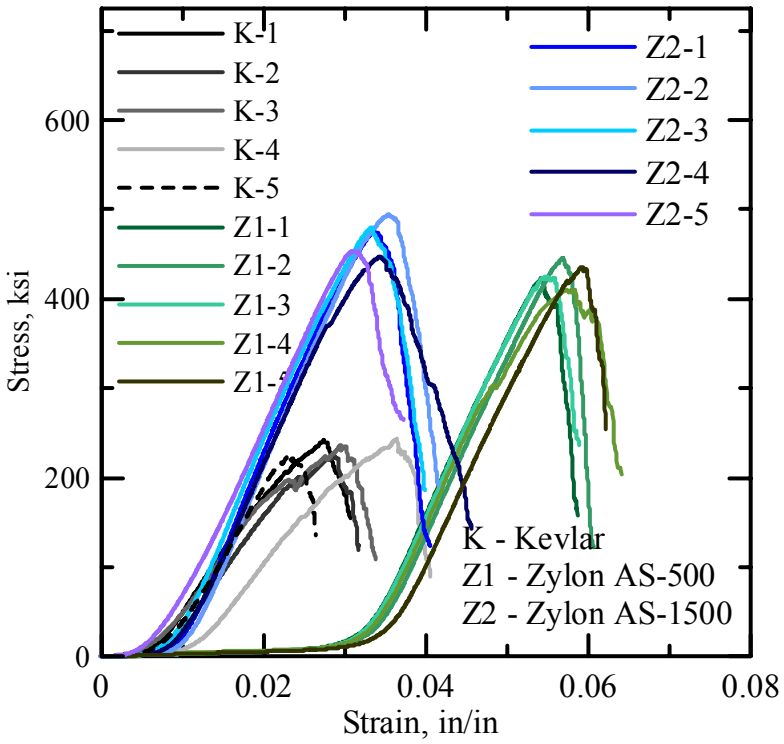

Figure 2.36: Stress-Strain Curves for All Three Fabrics (E_{11})

The initial portion of the load-deflection graph shows a large increase in displacement (actuator stroke) for a very small increase in load. The slack and crimp is predominant in Zylon AS-500 while it is almost similar for Zylon AS-1500 and Kevlar AS-49. As the load increases, the yarns stiffen as shown by the increase of the slope of the load-deflection graph. The failure of all the specimens is sudden (brittle behavior).

Table 2.17 and 2.18 shows the comparison of the results obtained from the simple tension tests run on all the three fabric types.

Table 2.17: Tension Tests Results – E_{11} Results

		For E_{11}			
	Fabric Type	Max. Stress ksi	Max. Ult. Strain in/in	Toughness ksi	Stiffness ksi
Average	Kevlar AS-49	234.63	0.0291	3.52	13468.47
Std. Dev		8.99	0.0048	0.67	299.49
Average	Zylon AS-500	426.09	0.0362	6.58	19309.70
Std. Dev		16.80	0.0017	0.48	511.95
Average	Zylon AS-1500	469.97	0.0336	8.89	21616.43
Std. Dev		19.18	0.0015	0.79	373.61

Table 2.18: Tension Tests Results – E_{22} Results

		For E_{22}			
	Fabric Type	Max. Stress ksi	Max. Ult. Strain in/in	Toughness ksi	Stiffness ksi
Average	Kevlar AS-49	238.65	0.0217	3.00	15283.91
Std. Dev		20.67	0.0022	0.19	285.27
Average	Zylon AS-500	398.29	0.0264	7.23	19361.59
Std. Dev		23.40	0.0019	0.76	356.65
Average	Zylon AS-1500	443.94	0.0296	8.97	21306.00
Std. Dev		18.48	0.0012	0.34	261.53

The stiffness values obtained from the E_{11} and E_{22} tests for the Zylon fabrics are almost similar. The values differ by about 15% percent for the Kevlar fabrics. This difference can be attributed to different manufacturing batches used for the specimen testing. The standard deviation for the (Kevlar) peak strain values of five tests is 0.48% and 0.22% for the Young's Modulus in the warp and fills direction respectively. In the case of Zylon, the peak strain values obtained using Zylon AS-500 are less than those obtained from Zylon AS-500. The standard deviation of the peak strain for the five tests for E_{11} is 0.17% and 0.15%. The ultimate tensile strain is obtained by dividing the elongation at peak load by the specimen gage length. Gage length used for the grip is L1. The modulus of elasticity was measured as the maximum slope within the linear range of the ascending portion of the stress strain curve. The toughness of each specimen is calculated as the area under the stress strain curve. This included the initial nonlinear ascending portion of the curve and nonlinear post peak response of the curve.

The average Poisson's ratios for the three fabric types are represented in the table 2.19. It is observed that the Poisson's ratio gradually decreases as the specimen approaches its failure. The higher values of standard deviation for the final stress range are due to the failure of some yarns in the vicinity of the clip gage system. This failure is more prominent in the E_{22} specimens that measure the Poisson's ratio ν_{21}. There is a significant decrease in Poisson's ratio ν_{21} as compared to the Poisson's ratio ν_{12} for the Kevlar fabric and an increase for Zylon AS-500 fabric. Both the Poisson's ratios are almost the same for Zylon AS-1500.

Table 2.19: Tension Tests Results – Poisson's Ratios

	Poisson's ratio ν_{12}			Poisson's ratio ν_{21}		
Fabric	Stress Range	Average	Std. Dev	Stress Range	Average	Std. Dev
Kevlar AS-49	29-87 ksi	1.844	0.090	58-116 ksi	0.611	0.267
	87-145 ksi	0.705	0.069	116-174 ksi	0.222	0.201
	145-203 ksi	0.618	0.079	174-217 ksi	0.087	0.220
Zylon AS-500	73-174 ksi	0.676	0.147	73-174 ksi	1.293	0.124
	174-290 ksi	0.152	0.027	174-290 ksi	0.762	0.130
	290-363 ksi	0.052	0.014	290-363 ksi	0.817	0.443
Zylon AS-1500	73-174 ksi	0.503	0.150	73-174 ksi	0.525	0.122
	174-290 ksi	0.215	0.188	174-290 ksi	0.147	0.098
	290-363 ksi	0.084	0.255	290-363 ksi	0.093	0.079

Some of the failure modes using the grips are shown in Figure 2.37 through 2.42. The failure (broken yarns) occurred at the middle of the specimen for the Kevlar specimen while the failure occurred near the grips for the Zylon specimen. For the E_{22} specimens, there is a localized failure in most of the specimens.

Figure 2.37: Kevlar specimen

Figure 2.38: Failure at center

Figure 2.39: Zylon AS-500 specimen

Figure 2.40: Failure at the edge

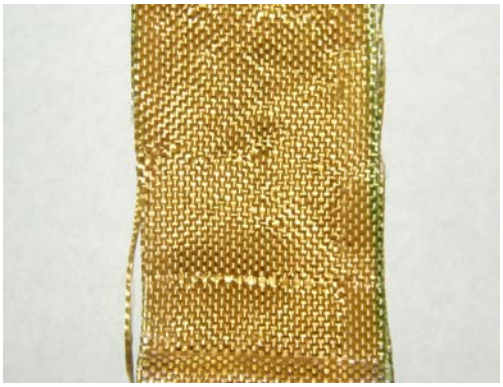

Figure 2.41: Zylon AS-1500 specimen

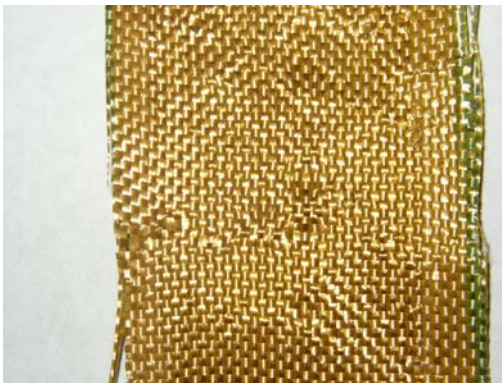

Figure 2.42: Localized Failure

Chapter 3: Static Ring Tests

3.1 Introduction to the Static Ring Tests

A series of static ring tests were conducted on the two types of fabric: Kevlar AS-49 and Zylon AS-500. These tests were conducted using a steel ring to simulate the engine housing of an aircraft in case of fan blade out event. A total of 21 tests on Kevlar AS-49 and 21 tests on Zylon AS-500 were conducted. These tests were carried out for 1, 4 and 8 layer fabric wraps.

3.1.1 Objectives

The primary objective of static tests is to simulate the penetration of the blunt object through the engine containment system assembly. A steel cylinder is used to simulate the engine housing, and the composite fabric is wrapped around this cylinder. The tests were conducted by applying the load in a quasi-static manner until failure, defined as full penetration of the blunt nose through the single or multi-layer fabric. The load and deformation history were collected throughout the test and energy absorption capacity of the structure was calculated from this response. This test may ultimately be used as one of the key parameters in the determination of properties and design of the containment chamber.

3.1.2 Specimen Preparation Procedure

The proposed plan for testing required determination of the load-deformation response of single and multi-layer specimens for both Kevlar and Zylon wraps. The specimens were subjected to outward penetration motion of a blunt nose assembly at various orientations and positions of the two different blunt noses. The blunt nose assembly was initially set up inside the steel ring. The specimen dimensions were 32” in diameter, 4” wide and consisted of 1, 4, and 8 layers wrapped around the outside of the steel cylinder. A small window was machined in the ring to allow for the penetration of the blunt nose.

For the single layer specimens, a 6” length of fabric overlap was used to glue the fabric onto itself. For multi layer fabrics, the first layer was directly mounted onto the ring and temporary fixed onto it by means of a standard cello tape. The last layer was glued to the previous layer using 5-minute® epoxy. Overlap length for all specimens was 6”. The specimens were covered with opaque plastic sheeting to minimize the degrading effects of moisture and ultraviolet light.

3.1.3 Test Setup

A test fixture was manufactured by rolling a section of A36 mild steel to the inner diameter dimensions of the test setup. The ring dimensions are as follows: Outer Diameter (OD) of 32”, Internal Diameter (ID) of 30”, width of 6”, and a thickness of 1”. This ring was the main component of the loading fixture and was fabricated at Karlson Machinery, Phoenix, AZ. The complete loading fixture was made up of four major parts. The ring was assembled in two parts - as a large, and a small arc. The other components

include the two side support plates and end plate to connect the two ring components. A detailed view of the cylinder with side plates is shown in Figure 3.1. The small arc that was cut out from the ring was connected at the bottom of the ring assembly and did not alter the geometry of the test set up. The size of the small arc corresponds to a 38° angle. Use of the ring as two parts allowed for easy installation of the specimen in the loading fixture. The specimens were first wrapped on an aluminum mandrel (Figure 3.2). Removal of the small arc during the sample mounting stage facilitated the transfer of the test specimen from the transfer mandrel (Figure 3.3). The cylinder was attached to two side plates using 15-3/4" diameter high strength bolts connected along the ring's perimeter. These side plates were connected to the base-plate; hence the ring had a clearance of 3" from the base plate.

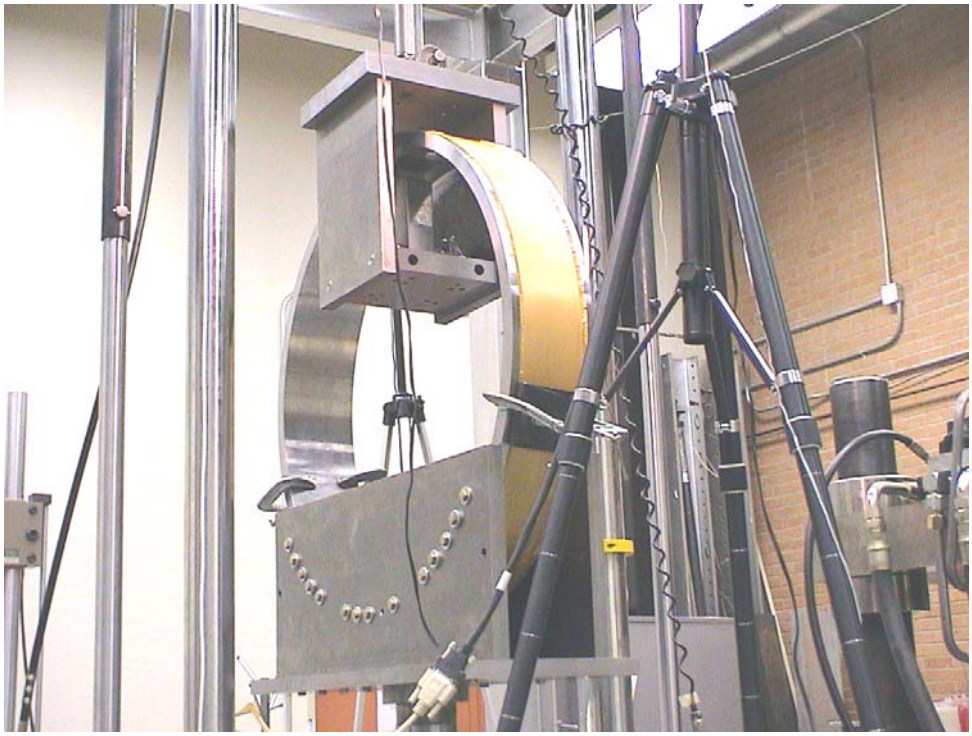

Figure 3.1: Test setup

Figure 3.2: Mandrel for specimen preparation

Figure 3.3: Specimen transfer ring

Two different blunt noses were used as the penetrators for the tests in this program. The dimensions of steel noses are as described in the table 3.1. Figures 3.4 and 3.5 illustrate the two different blunt noses.

Table 3.1 Dimensions of the Various Blunt Noses

Type of Blunt Nose	Width	Thickness	Radius
Thicker Penetrator { Type A }	2”	0.3125”	0.1563”
Thinner Penetrator {Type B}	1.5”	0.2370”	0.1185”

Figure 3.4: Top View Comparison of the Two Blunt Noses

Figure 3.5: Side View Comparison of the Two Blunt Noses

Another important parameter was the effect of fixity of the blunt nose loading mechanism with respect to the specimen, especially with large displacements expected throughout the test. It was expected that if the side loads were not removed through the use of hinges, a stiff system would be created which would result in side loads. Alternatively, any rotation of the test assembly could result in loss of contact of the full length of the blunt nose with the fabric, thus increasing the contact pressure and premature failure of the specimen. Measurement of such second order effects would be difficult if not impossible. Thereby, it was found necessary to fix the end conditions at the top of the blunt nose housing by fixing the load cell bearings that were placed orthogonal to the nose bearings as shown in Figure 3.6. In order to avoid side loads and thereby the titling of the blunt nose, the fixed-fixed condition for the blunt nose assembly as shown in figure 3.7 was used for all the forty-two tests conducted.

Figure 3.6: Top plate with bearings orthogonal to nose bearings (Fixed end condition at top)

Figure 3.7: Blunt nose housing design (fixed-fixed conditions)

In order to avoid transferring the entire load to the end joint C-Clamps were used at points remote from the blunt head contact. The tests were conducted with the clamps in place for both Kevlar and Zylon specimens. These clamps were placed at the same height on both sides of the ring to maintain symmetry and uniformity – clamps are placed at the height of 13.75” from the top of the base plate or at the height of 10.75” from the bottom of the cylinder OD. The figure 3.8 illustrates the attachment of the C-Clamps to the steel ring.

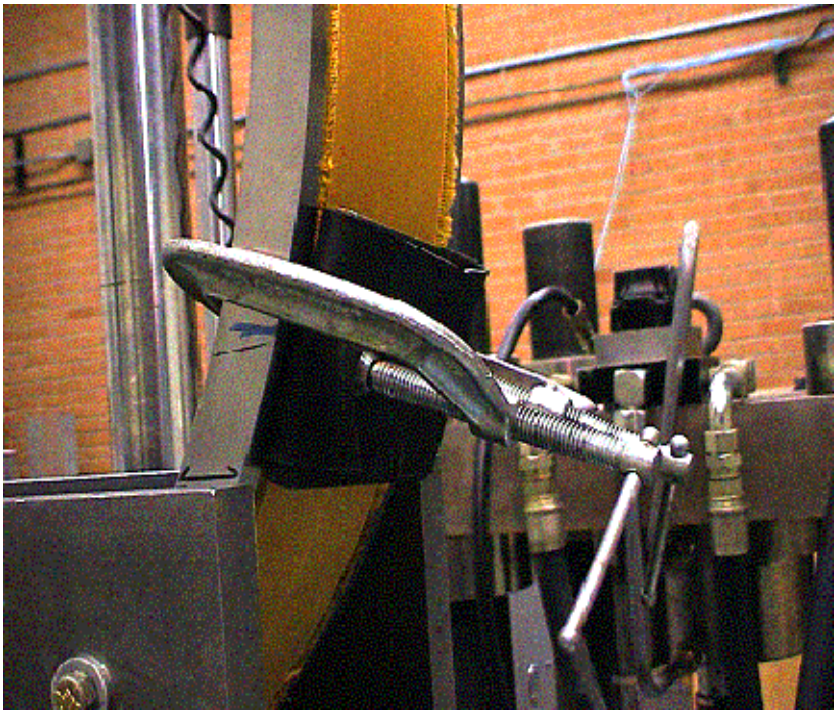

Figure 3.8: Attachment of C-clamps to the specimen

It was furthermore observed through the preliminary tests that significant slack existed for the multi-ply Zylon samples. This can be verified through the analysis of the

raw test data, which indicated up to 2” of stroke travel under an insignificant amount of load (e.g. up to 250 lbs). In order to relieve the slack, the specimens were pre-tensioned using an outward pressure applied at the bottom portion of the ring. The pressure was applied by placing two steel spacer blocks between the small arc of the ring and the spacer plate, and pushing the spacer plate outward by tightening the screws. Schematic diagrams of this set up are shown in figures 3.9 and 3.10. This ensured some of the slack recovery.

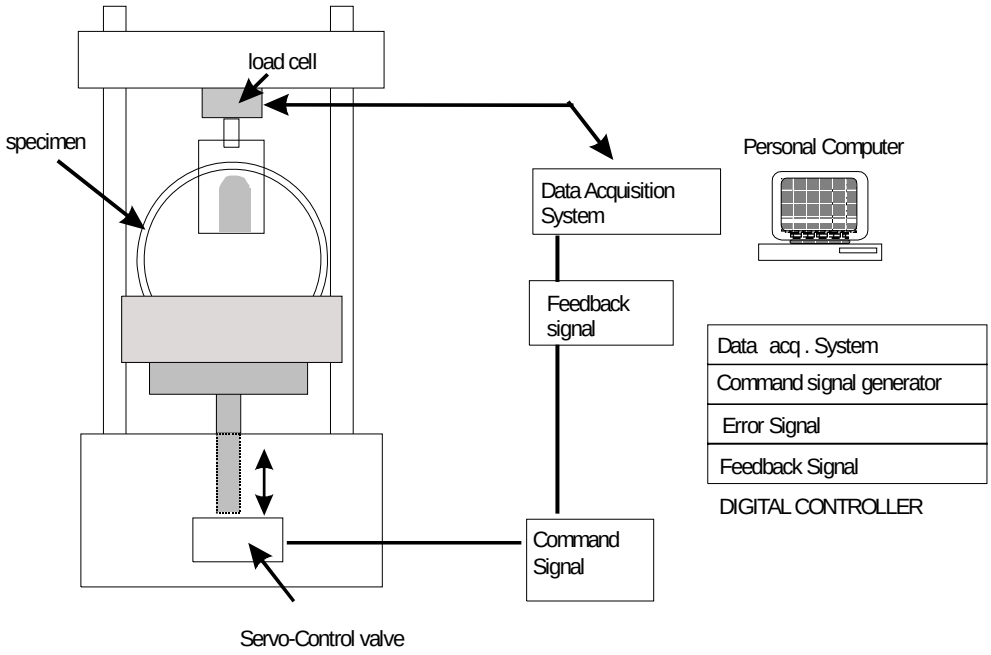

Figure 3.9: Schematic diagram of the test setup

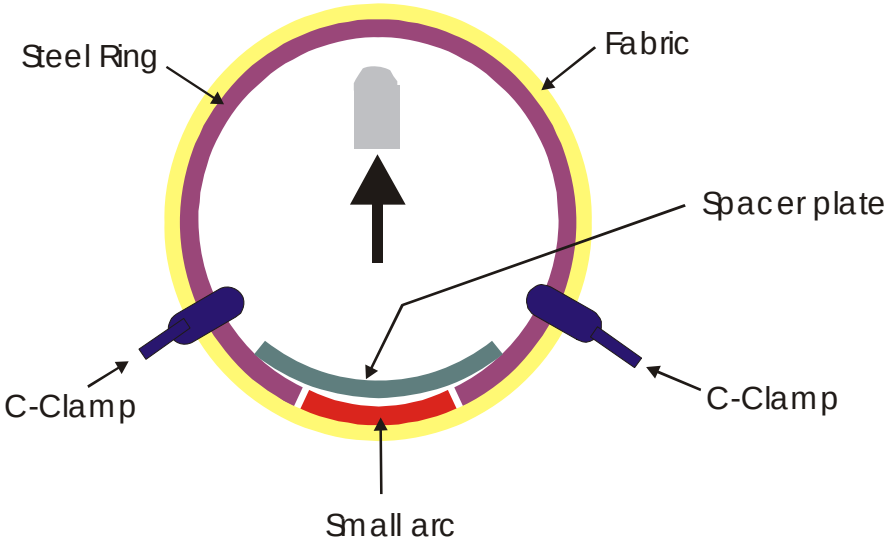

Figure 3.10: Schematic of test setup with clamps and hinges to remove spurious loads

Additionally, a threaded rod in between the blunt nose and the support plate was used in order to increase the length of the nose. This also facilitated the rotation of the blunt nose for various angles as proposed in the test plan. For testing the fabrics for the off center orientation, a new set of base blocks were designed. These base blocks when fixed onto the base plate align the edge of the penetrator at a distance of 0.15” from the edge of the machined window.

3.1.4 Test procedure

Each sample was transferred from the wrapping mandrel to the test rig and the side plates were then attached. An MTS servo-hydraulic test machine with Digital Teststar2 controller software was used for all the specimens. All the tests were conducted under actuator control using a constant rate of travel of 0.4”/min. The test was conducted in a manner such that the load cell housing the blunt nose remained stationary throughout

the test, while the actuator and, hence the ring, moved downward thus loading the fabric against a stationary blunt nose. The data were collected using a digital data acquisition system at a rate of 2 Hz.

For certain specimens, the test was run in a single step and continued until failure occurred. For multi-ply specimens (4, 8 ply Kevlar and all Zylon) tests were performed in two steps. Since the maximum actuator travel length was limited to 4 inches, a readjustment of the position of the sample was necessary to extend the total displacement beyond 4" expected in the multi ply and Zylon tests. During the first stage, the sample was loaded to 250 lbs and the test was placed on hold. At this point the actuator was brought back to the zero position, while the cross head was moved up to maintain the preload of the sample at the 250 lbs. At this point, the test was resumed, and displacement was imposed until the failure of specimen. The adjustment of the cross head was necessary to ensure enough travel was available for the sample to fail without causing any impact on the quality of the data obtained.

3.2 Static Ring Test Results

The load deflection curves for various multi ply specimens of Kevlar AS-49 and Zylon AS-500 were obtained from the data generated through the static ring test. It was observed that in the initial region of the load deflection curve there was a gradual increase in the deflection with minimal increase in the load carrying capacity. This was attributed to the slack due to the sliding and loss of gripping at the clamps. The amount of slack in all tested specimens was significant to the level of up to 3" of travel distance.

The latter part of the load deflection curve is considered to be dominated by slack recovery (there is some deformation because of the straightening of the yarns) and gradual loading of the specimen to reach the stiffness of the fabric being loaded in tension on the static ring.

Finally, the ultimate load is reached in these samples in an abrupt manner after several yarns fracture. The fracture of the yarns before the peak load is observed as the sudden jump in the load response. The load carried by the fractured yarns is being transferred to unbroken yarns. It is expected that the load redistribution after the fracture of a few yarns results in excess load on the surviving yarns. This excess load is sufficient to push the average stress on the yarns beyond the average ultimate tensile strength. A maximum level as high as 60% post peak strength was observed in some samples.

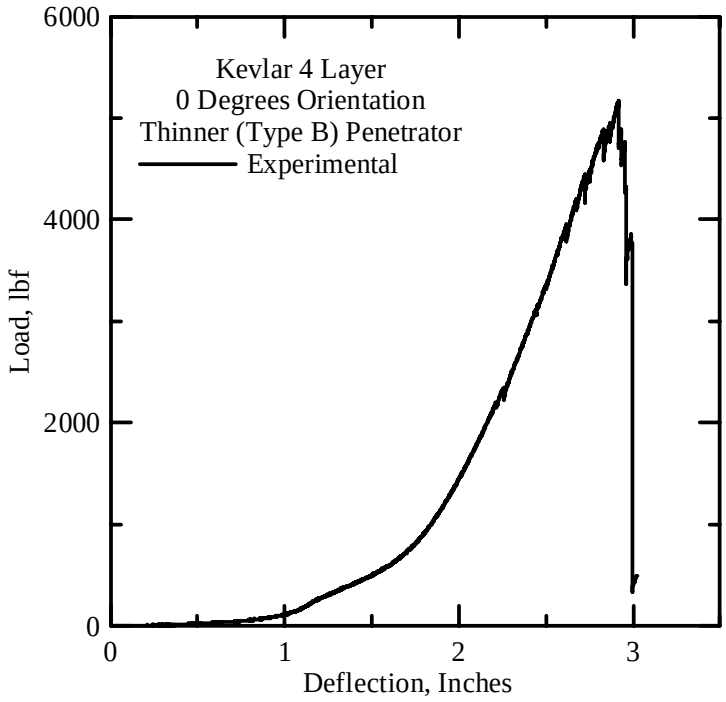

Figure 3.11: Typical Load Deflection Response

The figures 3.12 and 3.13 show a four layer Kevlar AS-49 specimen tested with the thinner penetrator. Figure 3.12 shows the fabric during the beginning of the test while figure 3.13 shows the fabric towards the end of the test approaching failure. The figure 3.13 shows that a number of yarns fractured yarns at that state of loading. Figure 3.12 was taken when the load was 4.5 lbs; figure 3.13 was taken at the load of 4617 lbs while the failure load was 5131.5 lbs. The failure of the specimen near the blunt nose area is shown in figure 3.14.

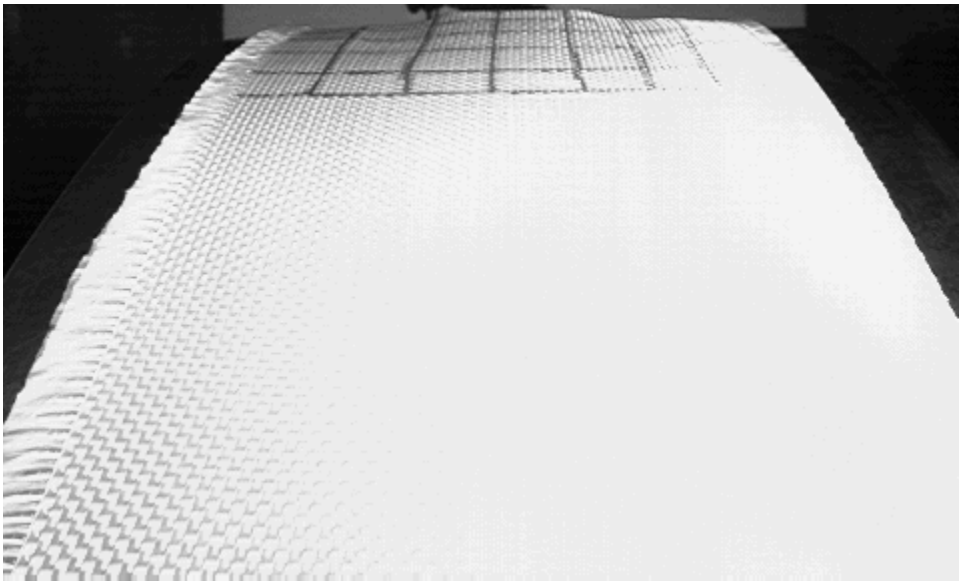

Figure 3:12: Kevlar Sample at Start of Loading.

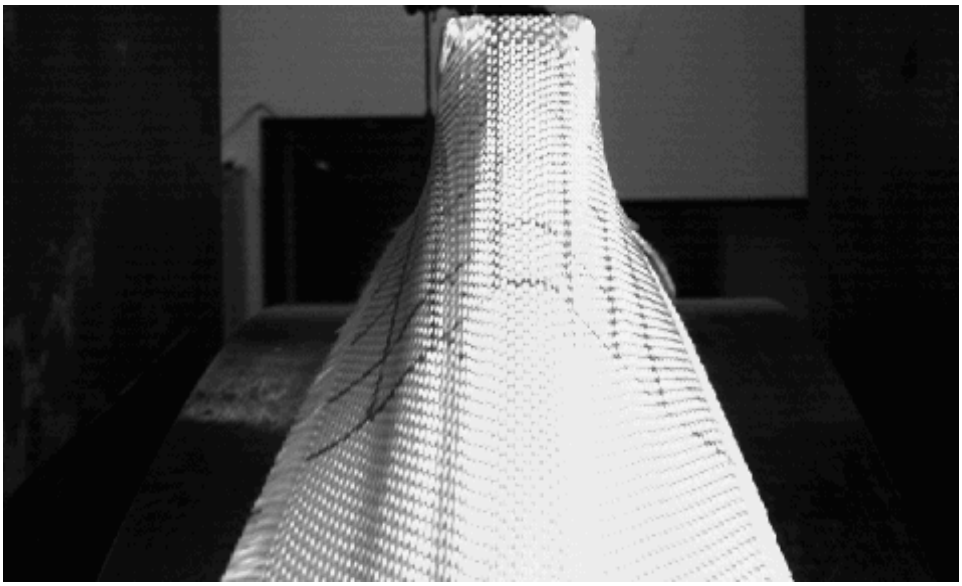

Figure 3:13: Kevlar Sample at End of a Static Ring Test.

Figure 3:14: Failure of Kevlar Sample at the Blunt Nose.

3.2.1 Kevlar Test Results

Multi-Ply, Multi-Orientation & Same Blunt Nose Comparison

The following section deals with the comparison of the results of the static ring test for Kevlar for different number of layers (1, 4 and 8) and orientations using the same kind of blunt nose.

Thicker Penetrator

The plot 3.15 hereafter shows the load deflection curves for 1, 4, and 8 layer Kevlar specimens for 45 degrees orientation for the thicker penetrator.

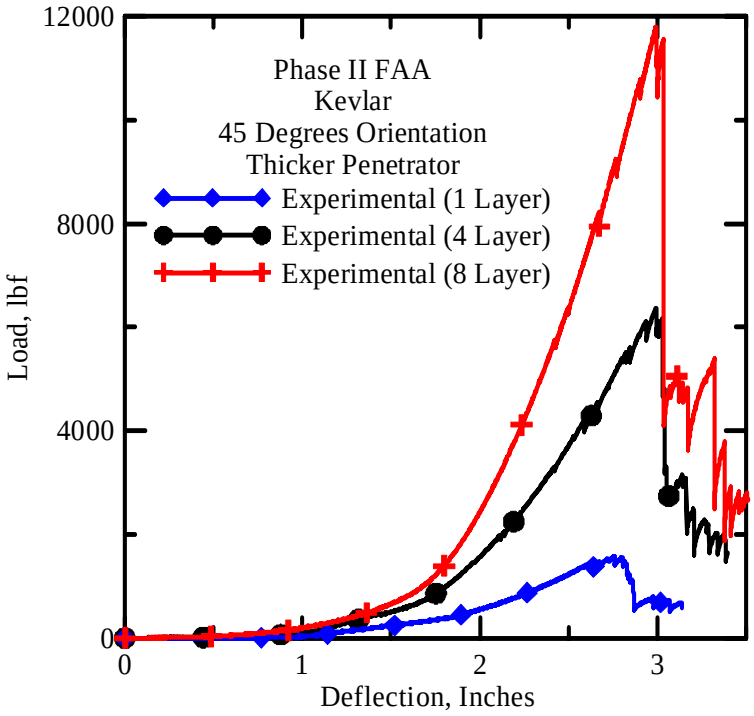

Figure 3.15: Load Deflection response of Kevlar for same orientation of thicker blunt nose for multi-layer specimens

The peak loads for 45 degrees orientation with the thicker blunt nose were 1573, 6363 and 11796 lbs for 1, 4 and 8 layers Kevlar fabric respectively. These peak loads seem to scale proportionally according to the number of layers of the Kevlar fabric tested.

The figure 3.16 below shows the load deflection response of one layer Kevlar fabric for different orientations of the thicker blunt nose.

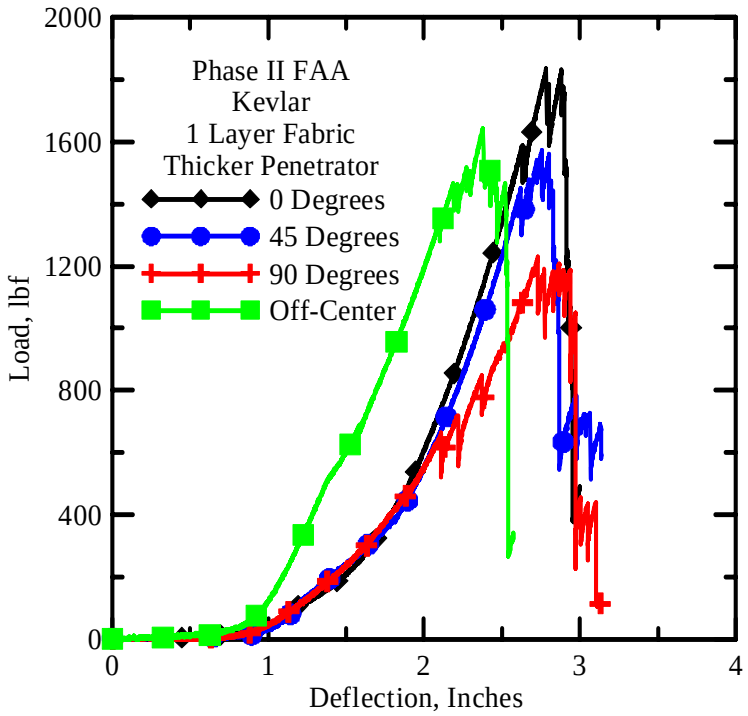

Figure 3.16: Load Deflection for various orientations of thicker blunt nose with one Layer Kevlar

Examination of figure 3.16 indicates that maximum loads at failure differ for various orientations of blunt nose for the same number of layers. The load is maximum at zero degrees orientation of the blunt nose and minimum at the 90 degrees orientation.

The figure also shows that stiffness of Kevlar (lb/in) remains fairly constant up to the fracture of the first yarn of the fabric. A drop in stiffness is observed from the 0 degrees to 45 degrees orientation of the blunt nose with the 90 degrees orientation having the least stiffness. Table 3.2 shows the stiffness values for multi layered Kevlar specimens for various orientations of the thicker penetrator. The maximum load for the off-center orientation of the blunt nose lies closer to the maximum load of the 45 degrees orientation with deviations of 69,161 and 829 lbs for 1, 4 and 8 layer respectively. The stiffness for the off-center orientation lies between the 45 and 90 degree orientation stiffness.

Table 3.2: Maximum Load & Stiffness for Kevlar for Thicker Penetrator

Layers	**Orientation**	**Maximum Load**	**Stiffness, lb/in**
1	0	1858	1715
1	45	1573	1418
1	90	1228	1080
1	Off	1642	1307
4	0	6625	5909
4	45	6363	5271
4	90	4925	4790
4	Off	6202	5079
8	0	13231	11025
8	45	11796	10618
8	90	9110	8340
8	Off	10967	9770

The responses for 4 and 8 layers of Kevlar fabric using the thicker penetrator are plotted in figures 3.17 and 3.18 respectively. These responses are similar to the one layer results for Kevlar.

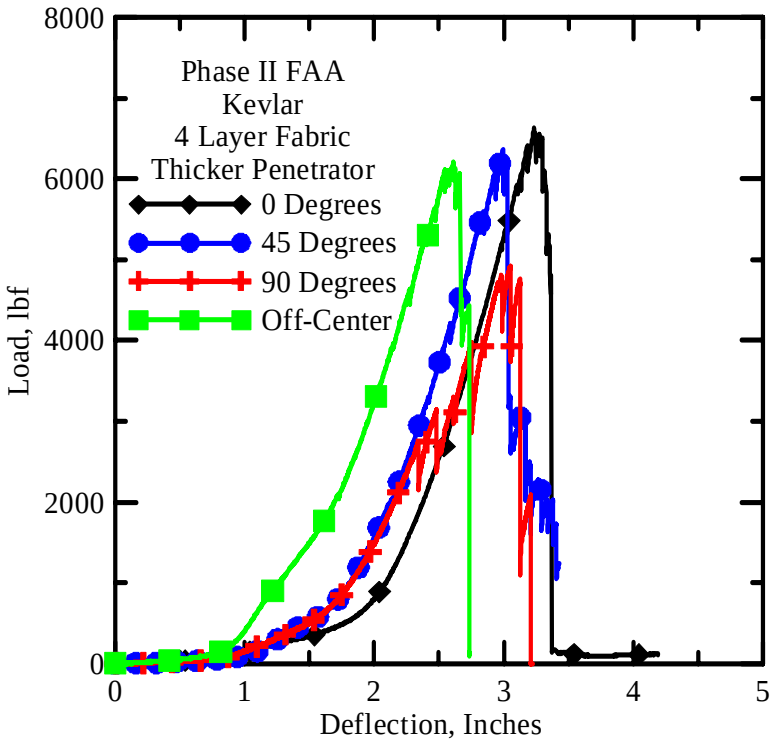

Figure 3.17: Various Orientations of thicker blunt nose - 4 Layer Kevlar Fabric

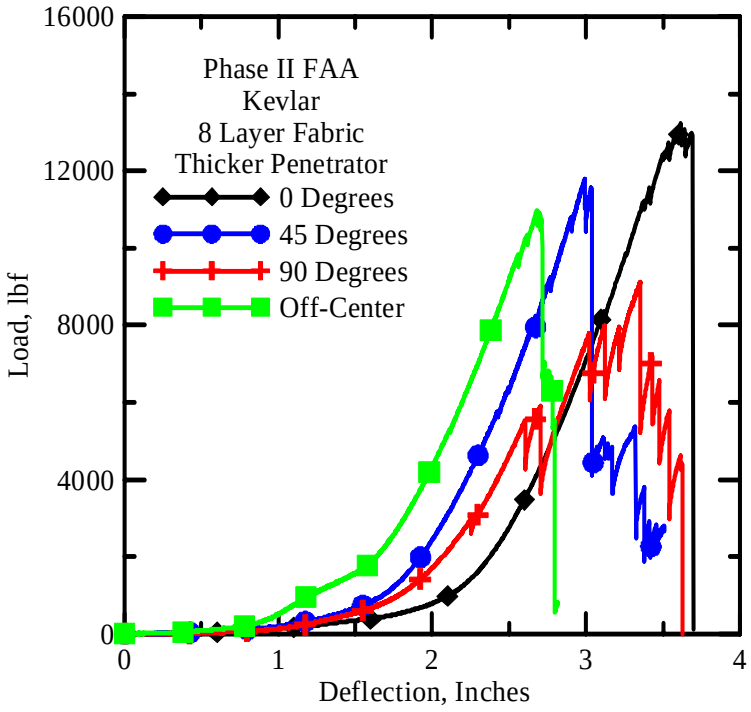

Figure 3.18: Various Orientations of thicker blunt nose - 8 Layer Kevlar Fabric

The figures 3.19 and 3.20 are the energy absorbed/areal density and normalized energy absorbed/areal density graphs for Kevlar samples tested using the thicker penetrator. The energy-absorbed graphs predict the fabric capacities as near linear in nature but the normalized energy absorbed capacity show that there is no consistency in the energy absorption capacity of the fabrics. Figure 3.21 represents the peak load vs. number of plies for Kevlar using the Type A Penetrator and Figure 3.22 represents the peak load normalized by areal density for the same. Figure 3.23 represents the stiffness vs. number of plies as well as linearly extrapolated stiffness values for Kevlar samples using the thicker blunt nose. Figure 3.24 shows the same with the stiffness value normalized with the areal density for Kevlar.

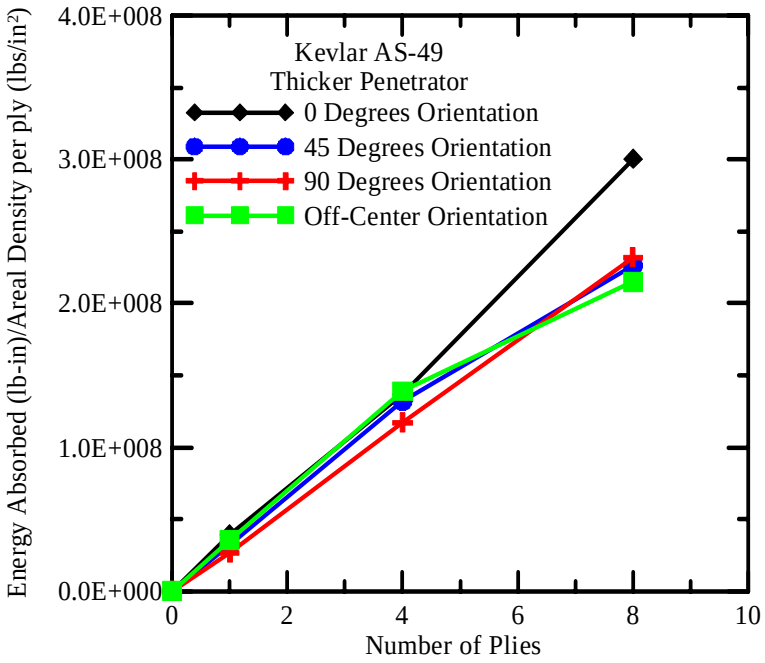

Figure 3.19: Energy absorbed/areal density graphs of 1, 4 and 8 ply Kevlar for thicker penetrator

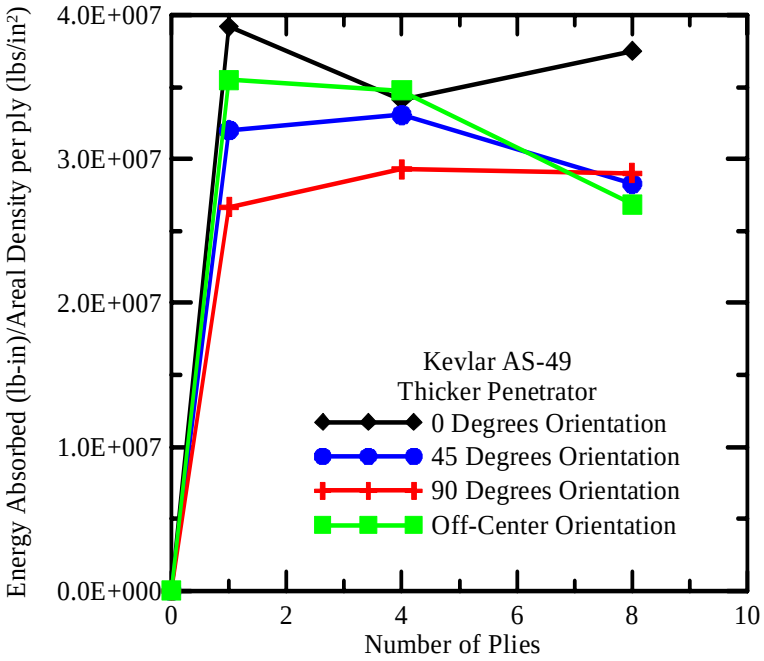

Figure 3.20: Energy absorbed/areal density graphs of 1, 4 and 8 ply Kevlar samples normalized by no of plies for thicker penetrator

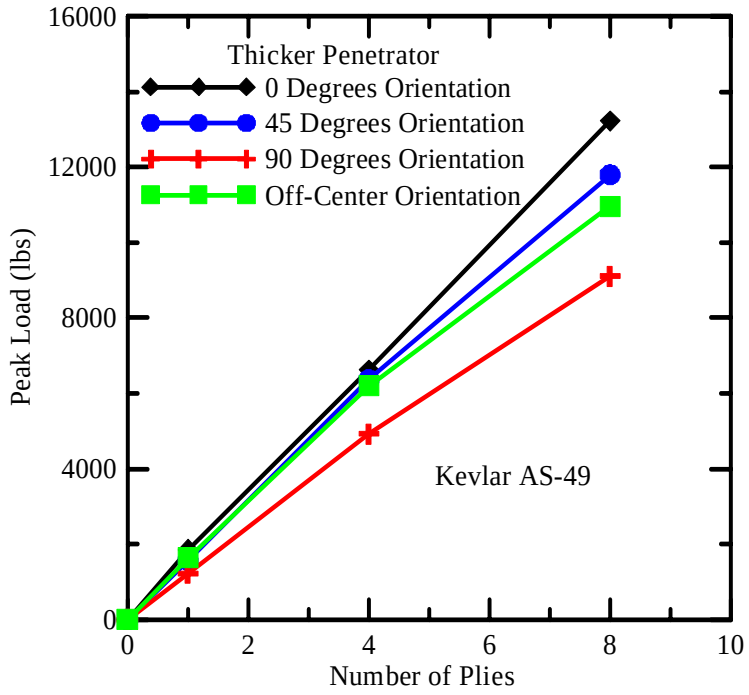

Figure 3.21: Number of plies vs. peak load for Kevlar using thicker penetrator

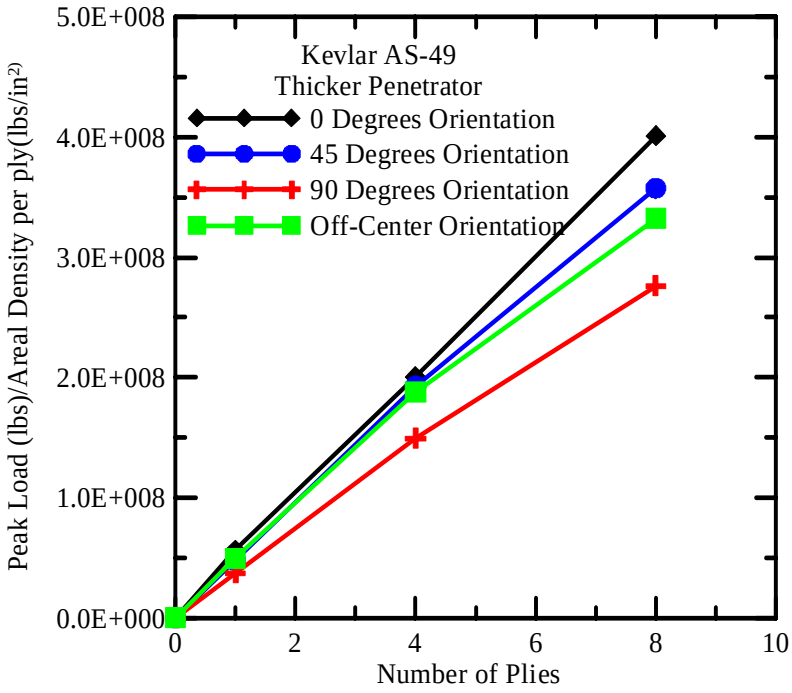

Figure 3.22: Number of plies vs. normalized peak load for Kevlar using thicker penetrator

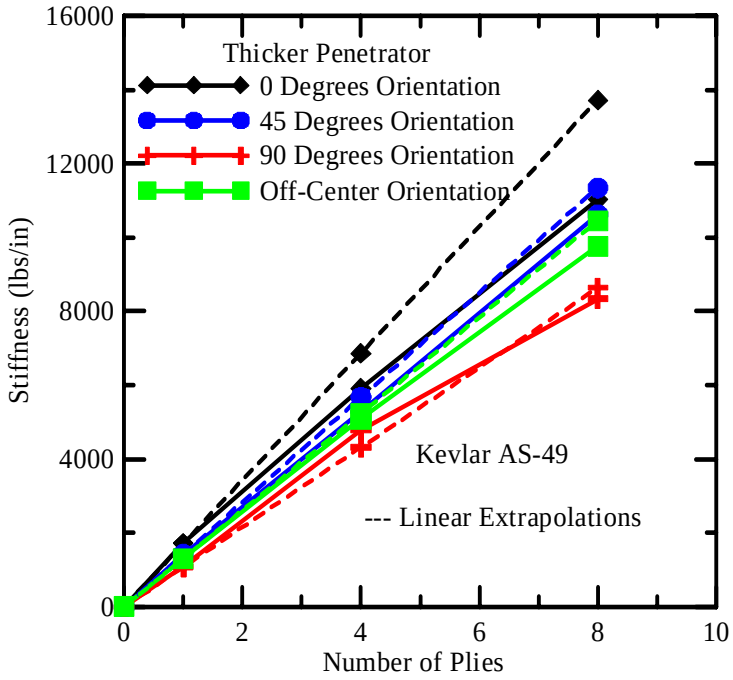

Figure 3.23: No. of plies vs. stiffness for Kevlar using thicker penetrator (actual and linearly extrapolated)

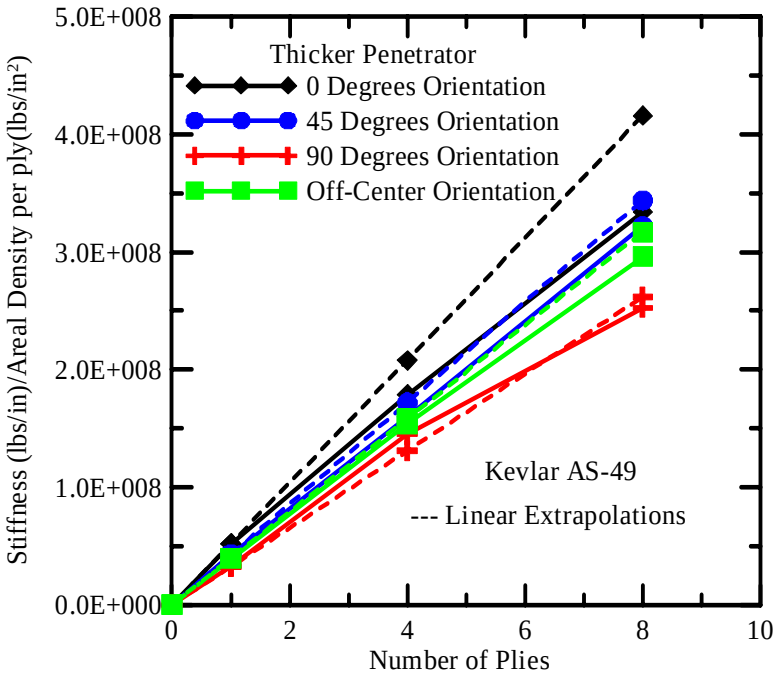

Figure 3.24: No. of plies vs. normalized stiffness for Kevlar using thicker penetrator (actual and linearly extrapolated)

Thinner Penetrator

The load deflection curves for 1, 4, and 8 layer Kevlar specimens for 45 degrees orientation using the thinner penetrator are shown in figure 3.25.

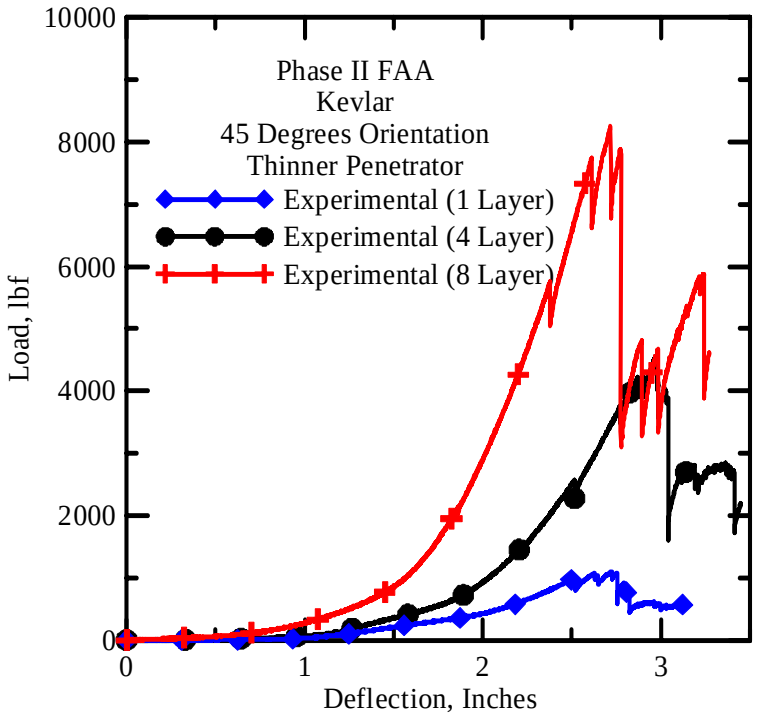

Figure 3.25: Load Deflection response of Kevlar for same orientation of thinner blunt nose for multi-layer specimens

The peak loads with the thinner penetrator were 1104, 4552 and 8257 lbs for 1, 4 and 8 layers respectively. The following plots show the response of multi-layered Kevlar fabric with the thinner penetrator. The figure 3.26 shows load-deflection plot for various orientations of thinner blunt nose with one layer of Kevlar.

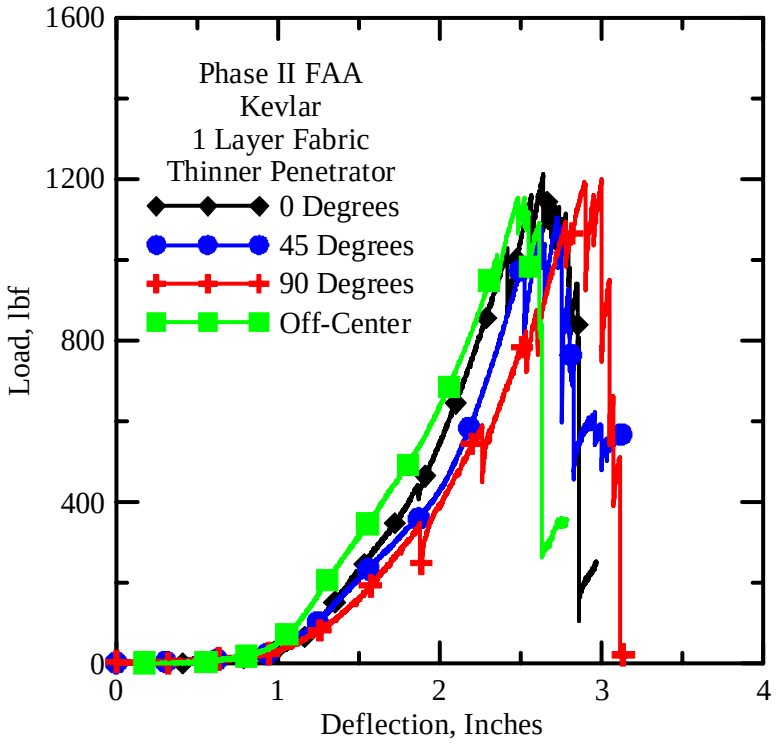

Figure 3.26: Load Deflection for various orientations of thinner blunt nose with one Layer Kevlar

The above plot shows that for the thinner penetrator, the maximum load at failure occurs at the 90 degree orientation. The stiffness (lb/in) is maximum for the zero degree orientation of the blunt nose and minimum at 90 degrees orientation. The 45 degree orientation stiffness lies midway between the other two stiffness values. Similar results for the stiffness were obtained for multi-layered Kevlar fabrics using the thinner penetrator. These plots for the multi-layered Kevlar fabric for different orientations are shown in figures 3.27 and 3.28. Table 3.3 shows the values of the maximum loads and stiffness for the thinner penetrator.

Table 3.3: Maximum Load & Stiffness for Kevlar for Thinner Penetrator

Layers	Orientation	Maximum Load	Stiffness, lb/in
1	0	1211	1037
1	45	1104	1031
1	90	1198	951
1	Off	1154	980
4	0	5169	4605
4	45	4552	4468
4	90	4511	4093
4	Off	5181	4285
8	0	9095	8391
8	45	8257	8266
8	90	9575	7671
8	Off	8796	8154

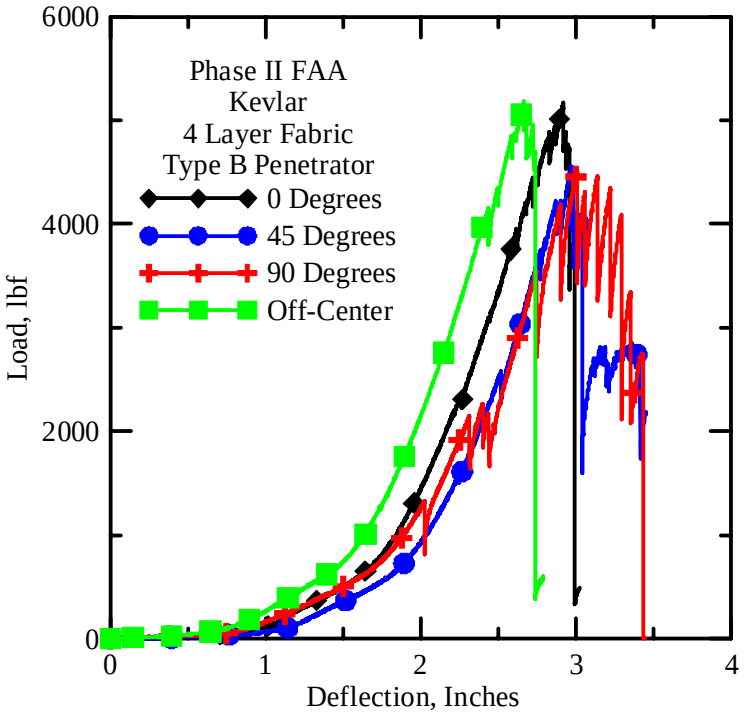

Figure 3.27: Various Orientations of thinner blunt nose - 4 Layer Kevlar Fabric

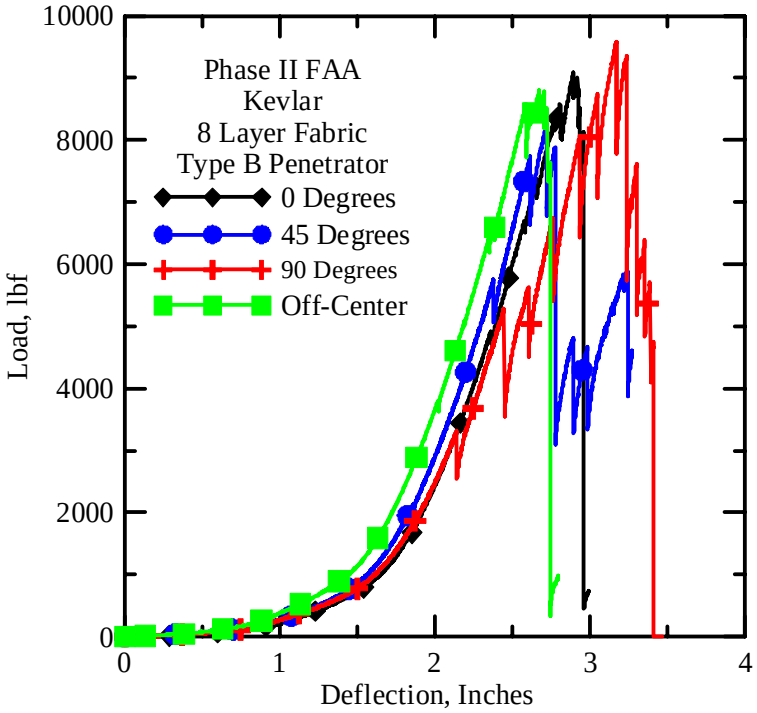

Figure 3.28: Various Orientations of thinner blunt nose - 8 Layer Kevlar Fabric

The energy absorbed/areal density and normalized energy absorbed/areal density graphs for Kevlar samples using the thinner penetrator are plotted in figures 3.29 and 3.30. Although, the energy-absorbed graphs predict the fabric capacities as near linear in nature but there is a significant variation in the normalized energy absorbed capacity for the different orientations. The graph of the peak load versus number of plies for Kevlar using the Type B Penetrator is shown in figure 3.31. The figure indicates that the peak loads for 90 degree orientations are significantly higher as compared to the other orientations. These can be attributed to the inverted V shape of the blunt nose and comparatively lower contact area of the blunt nose. Figure 3.32 represents the peak load normalized by areal density for the tested Kevlar samples. Figure 3.33 represents the stiffness versus number of plies as well as linearly extrapolated stiffness values for Kevlar samples using the thinner blunt nose. Figure 3.34 shows stiffness versus number of plies as well as linearly extrapolated stiffness values for Kevlar samples using the thinner blunt nose with the stiffness value normalized with the areal density for Kevlar. The figures 3.33 and 3.34 indicate that the linear extrapolation of stiffness gives a fair value of the actual stiffness as obtained from the tests.

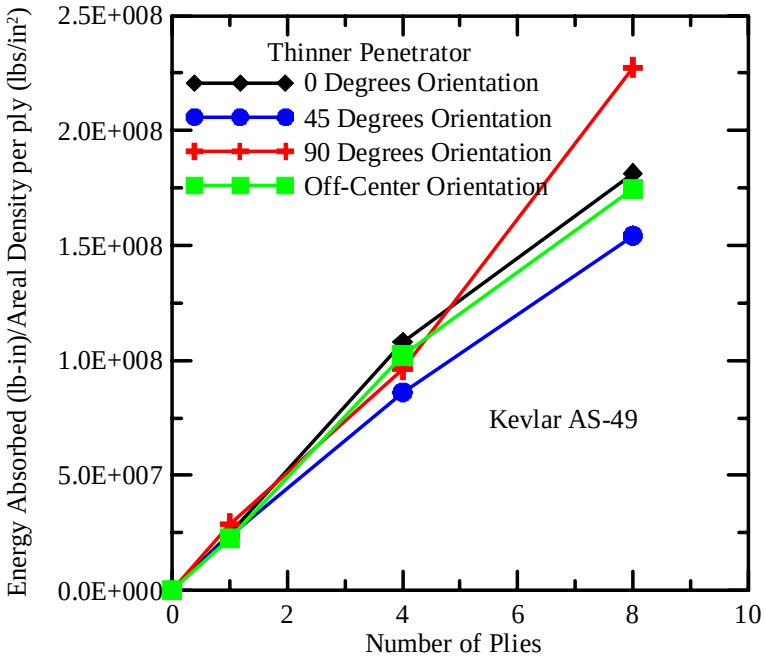

Figure 3.29: Energy absorbed/areal density graphs of 1, 4 and 8 ply Kevlar for thinner penetrator

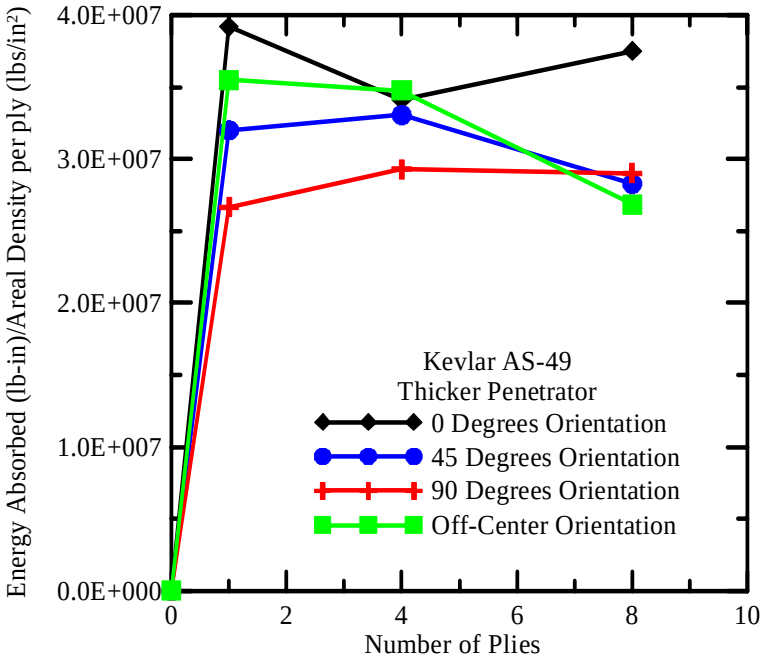

Figure 3.30: Energy absorbed/areal density graphs of 1, 4 and 8 ply Kevlar samples normalized by no of plies for thinner penetrator

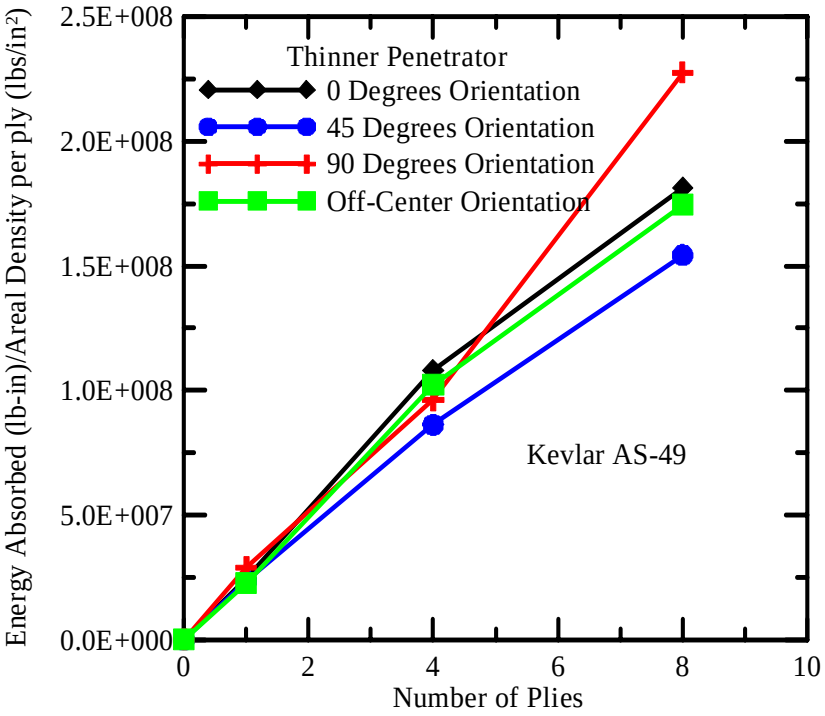

Figure 3.31: Number of plies vs. peak load for Kevlar using thinner penetrator

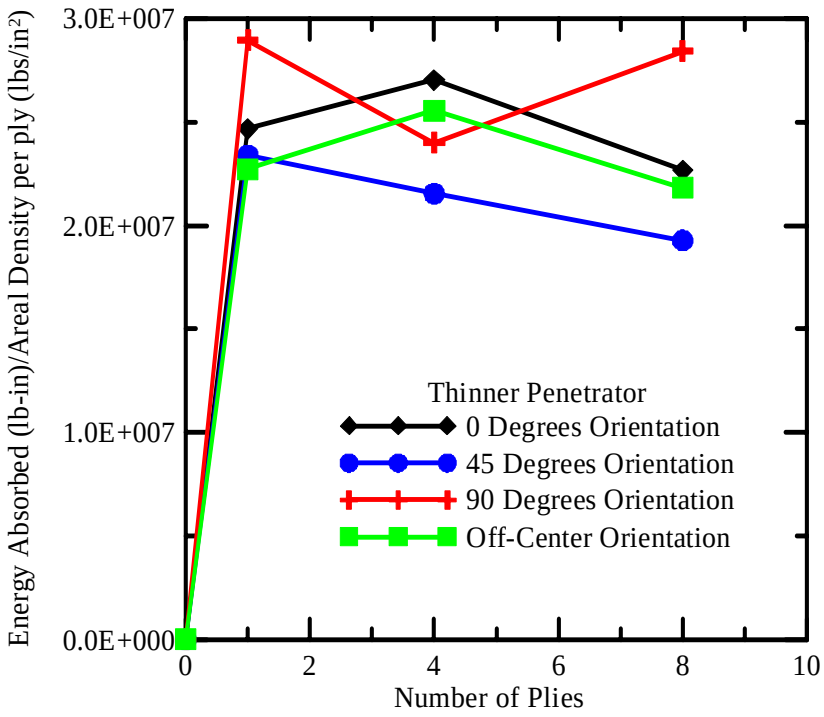

Figure 3.32: Number of plies vs. normalized peak load for Kevlar using thinner penetrator

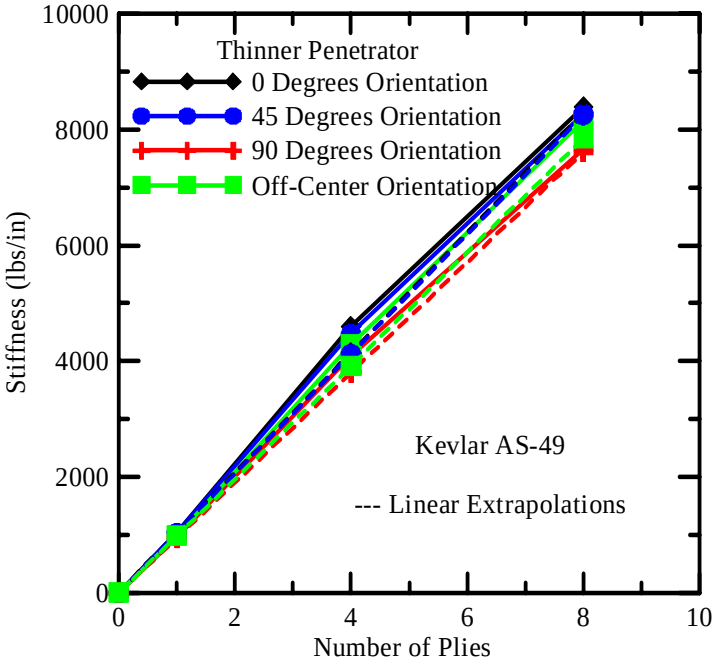

Figure 3.33: Number of plies vs. stiffness for Kevlar using thinner penetrator (actual and linearly extrapolated)

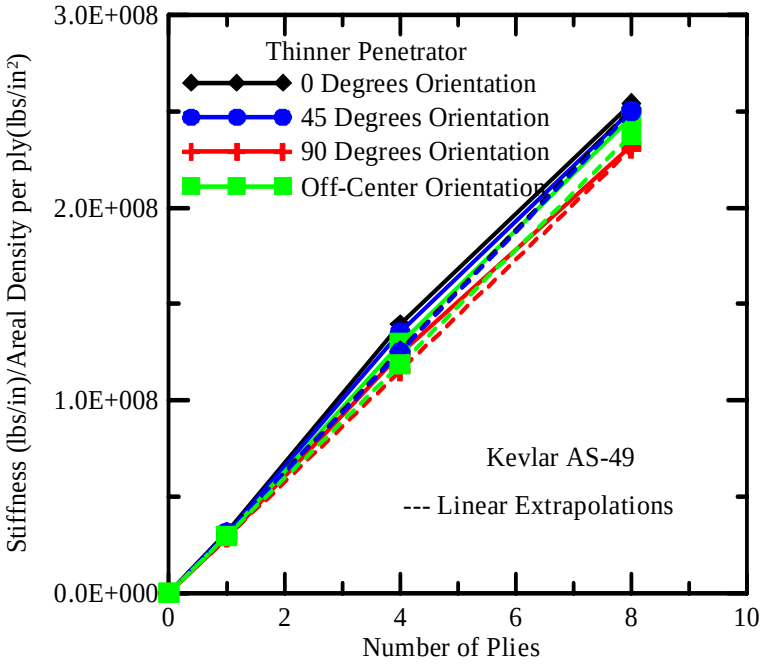

Figure 3.34: Number of plies vs. normalized stiffness for Kevlar using thinner penetrator (actual and linearly extrapolated)

Penetrator (Blunt Nose) Comparison

Slack Adjustment

The figures 3.35 and 3.36 show the typical load defection curve obtained for a Kevlar AS-49 sample tested at 45 degrees orientation using the thicker(Type A) and thinner(Type B) penetrator.

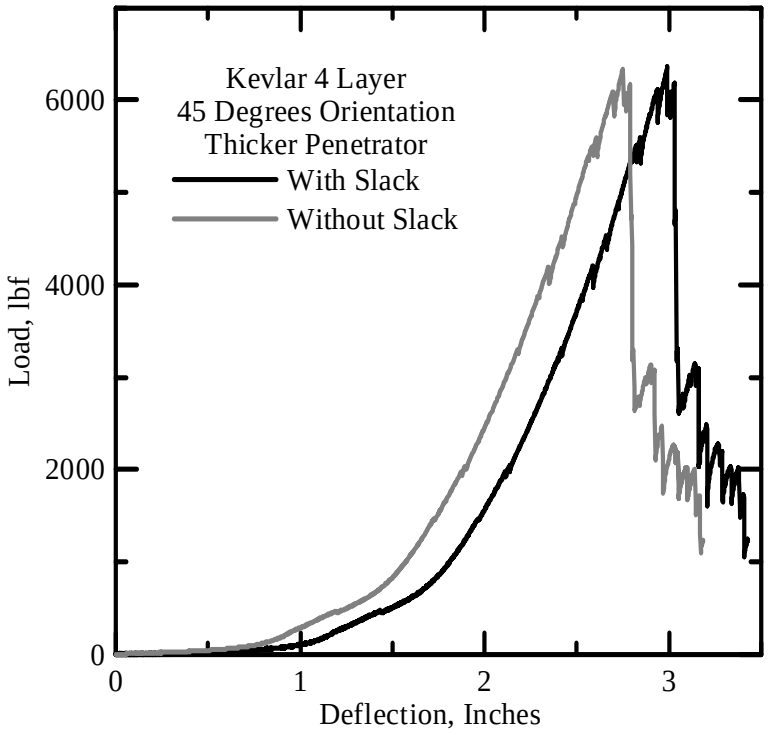

Figure 3.35: Load-deformation response of four layer Kevlar specimen with and without slack adjustment with thicker penetrator.

The slack adjustment was achieved by shifting the raw data load deflection curves along the x-axis so that the curve obtained would coincide with initial portion of the load deflection curve obtained from finite element analysis models prepared as simulations for the static ring tests for various orientations of the blunt nose. For the particular specimens shown above the slack adjustment was of 0.239 inches and 0.479 inches

respectively. It was observed that a higher slack adjustment was to be applied using the thicker penetrator for a better comparison with the simulations.

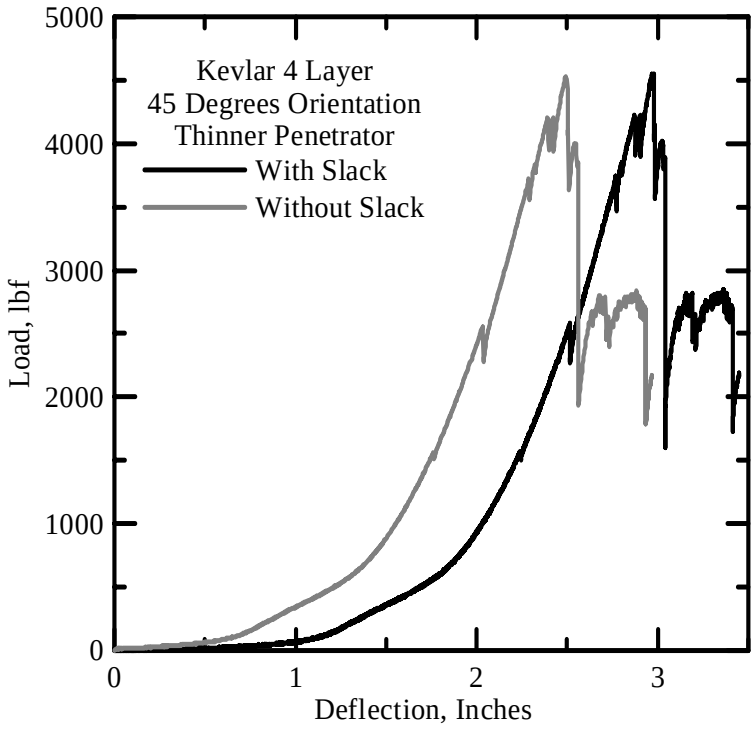

Figure 3.36: Load-deformation response of four layer Kevlar specimen with and without slack adjustment with thinner penetrator

Load Deflection Responses

The load deflection curves using the two different penetrators are plotted below show the comparison of the results for the same number of layers with the same orientation using the two different penetrators**.**

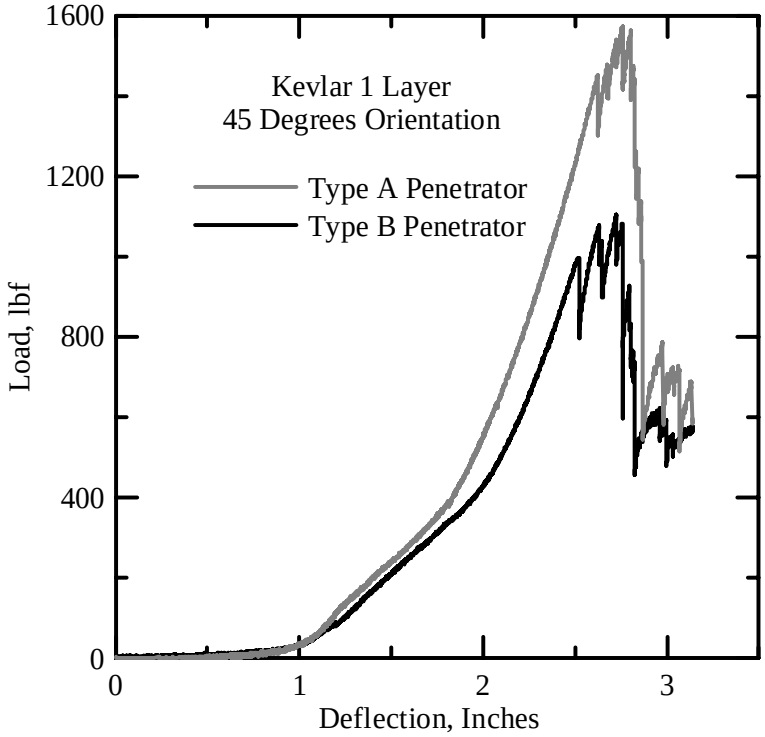

Figure 3.37: One Layer Kevlar – 45 Degrees Orientation – Both Penetrators

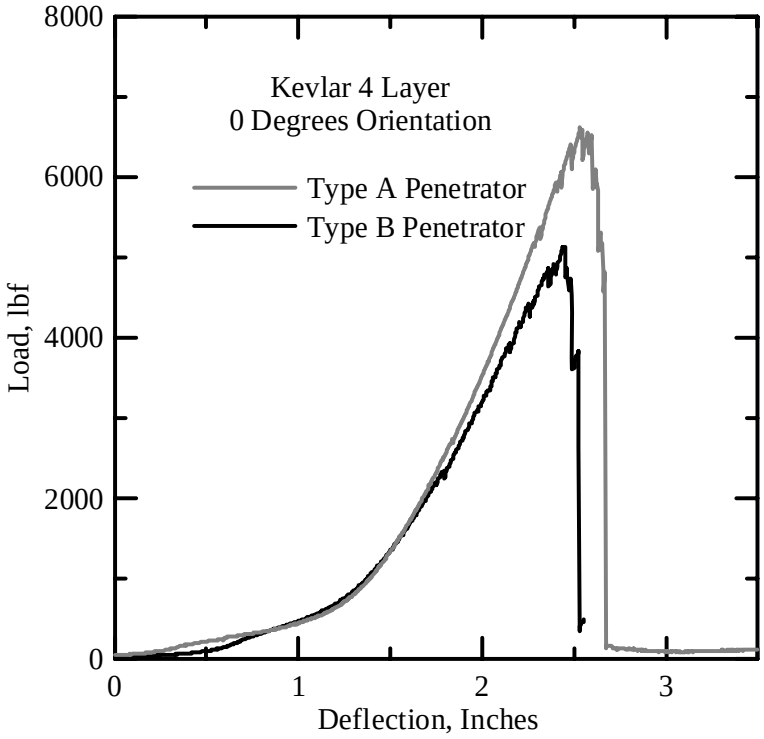

Figure 3.38: Four Layer Kevlar – 0 Degrees Orientation – Both Penetrators

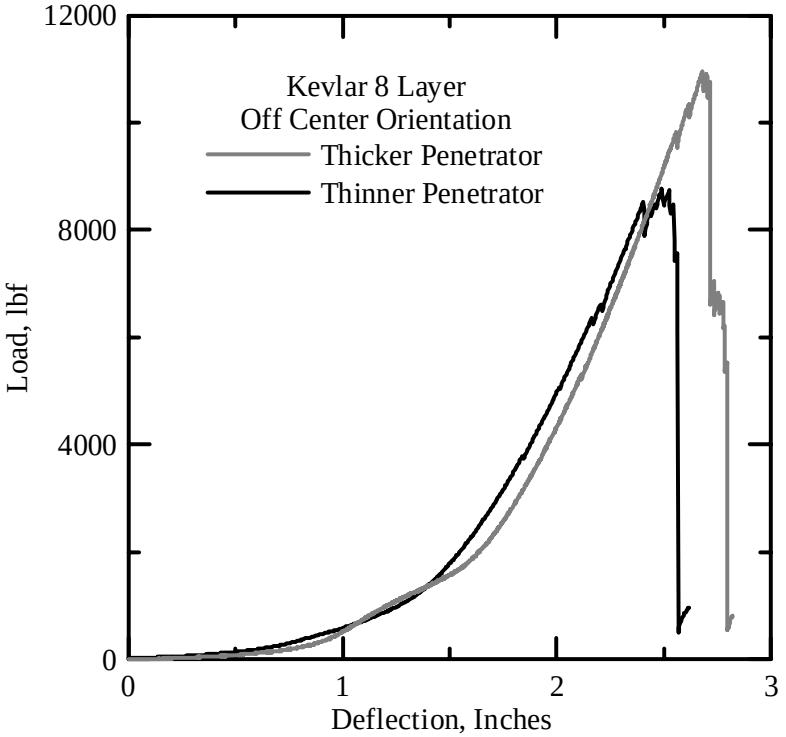

Figure 3.39: Eight Layer Kevlar – Off Center Orientation – Both Penetrators

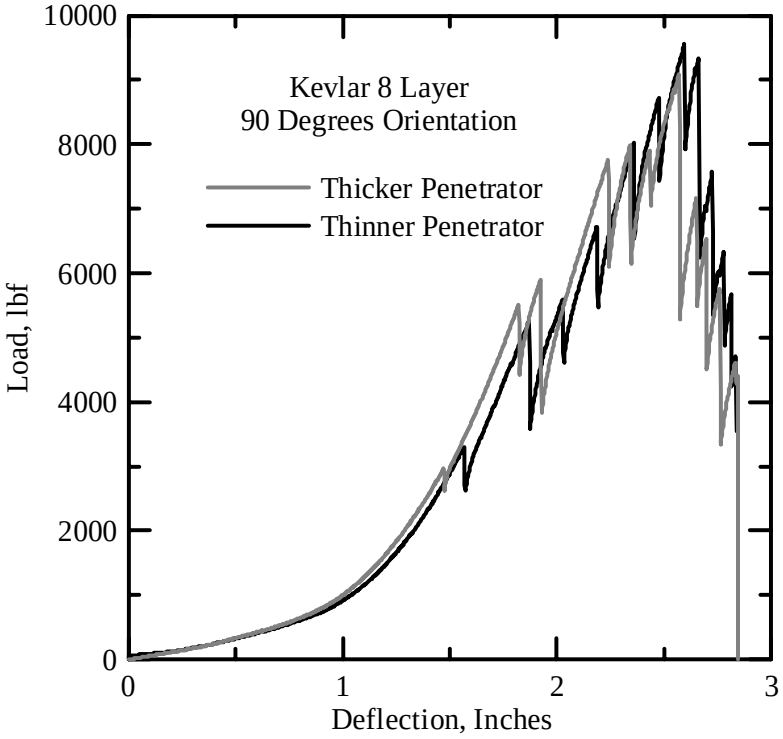

Figure 3.40: Eight Layer Kevlar – 90 Degrees Orientation – Both Penetrators

The figures 3.37, 3.38 and 3.39 shows that the maximum load obtained for the thinner penetrator is less than the maximum load obtained for the thicker penetrator. Similarly, the stiffness of the Kevlar with the thicker penetrator is higher than the stiffness with the thinner penetrator. It was obtained that the peak loads and highest stiffness for Kevlar samples using the thicker (Type A) penetrator was generally higher than that obtained for the thinner (Type B) penetrator specimens. A difference in this trend was observed in the 90 orientation as shown in figure 3.40. The maximum loads obtained with both the penetrators differ marginally for the 90 degree orientation. This may be attributed to the shear loading of the Kevlar specimens in the 90 degrees orientation as well as the inverted V Shape configuration of the blunt nose.

3.2.2 Kevlar Static Tests Result Summary

The table 3.4 the results of static ring tests conducted on Kevlar AS-49 for various orientations of the blunt nose using the thicker penetrator for different number of layers (1, 4 and 8). Table 3.5 summarizes the results for the thinner penetrator. The tables clearly indicate that the 90 degree orientation have the least apparent load at first failure. The tables also show that as the number of layers increase for a constant orientation, the post peak response gradually increases. Tables 3.4 and 3.5 also indicate that the strokes at peak loads become fairly constant as the number of layers increases for the same orientation

3.4: Kevlar Static Ring Test Results for Thicker (Type A) Penetrator

Blunt Nose Orientation	No of layers	Load at First Failure (lb)	Stroke at First Failure (lb)	Peak Load (lb)	Stroke at Peak Load (in)	Stiffness (lb/in)	Area under the curve (lb/in)	
							Pre Peak	Post Peak
0	1	1755	2.79	1858	2.90	1715	1293	219
0	4	6333	3.18	6625	3.23	5909	4503	889
0	8	8269	3.11	13231	3.62	11025	9907	1036
45	1	1439	2.61	1573	2.76	1418	1056	334
45	4	4181	2.58	6363	2.99	5271	4363	1156
45	8	5271	2.78	11796	2.99	10618	7461	2398
90	1	663	2.12	1228	2.73	1080	880	328
90	4	2693	2.33	4925	3.05	4790	3867	479
90	8	2895	2.24	9110	3.35	8340	7657	1484
Off	1	1335	2.11	1642	2.38	1307	1171	244
Off	4	4532	2.27	6202	2.61	5079	4587	622
Off	8	9810	2.56	10967	2.68	9770	7093	940

For all the twenty one tests, the blunt nose end conditions were fixed-fixed and clamps were used during testing for all cases.

3.5: Kevlar Static Ring Test Results for Thinner (Type B) Penetrator

Blunt Nose Orientation	No of layers	Load at First Failure (lb)	Stroke at First Failure (lb)	Peak Load (lb)	Stroke at Peak Load (in)	Stiffness (lb/in)	Area under the curve (lb/in)	
							Pre Peak	Post Peak
0	1	425	1.86	1211	2.64	1037	814	252
0	4	2285	2.25	5169	2.92	4605	3567	346
0	8	4789	2.36	9095	2.89	8391	5987	604
45	1	993	2.52	1104	2.72	1031	772	265
45	4	2553	2.51	4552	2.97	4468	2844	1329
45	8	5697	2.38	8257	2.72	8266	5091	2708
90	1	351	1.88	1198	3.00	951	956	79
90	4	1325	2.04	4511	3.01	4093	3170	1495
90	8	3281	2.13	9575	3.17	7671	7506	1649
Off	1	1006	2.35	1154	2.35	980	750	211
Off	4	4148	2.44	5181	2.66	4285	3373	407
Off	8	6354	2.35	8796	2.67	8154	5759	643

3.2.3 Zylon AS-500 Test Results

Multi-Ply, Multi-Orientation & Same Blunt Nose Comparison

The following section deals with the comparison of the results of the static ring test for Zylon AS-500 for different number of layers (1, 4 and 8) and orientations using the same kind of penetrator.

Thicker Penetrator

The plot 3.41 hereafter shows the load deflection curves for 1, 4, and 8 layer Zylon AS-500 specimens for off center orientation for the thicker penetrator.

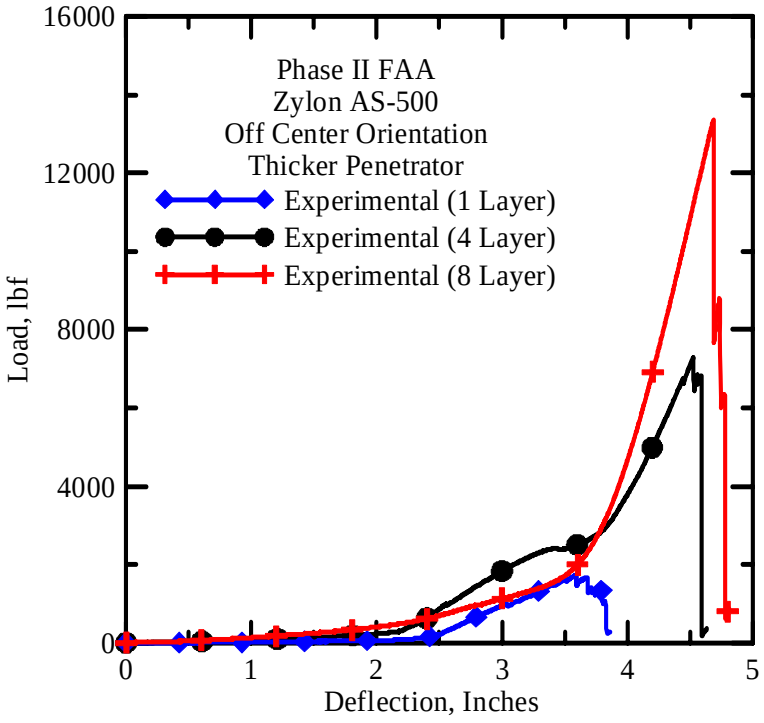

Figure 3.41: Load Deflection response of Zylon AS-500 for same orientation of thicker blunt nose for multi-layer specimens

The peak loads for off center degrees orientation with the thicker blunt nose were 1716, 7276 and 13349 lbs for 1, 4 and 8 layers Zylon AS-500 fabric respectively. These peak loads seem to increase non-linearly according to the number of layers of the Zylon fabric tested.

The figure 3.42 below shows the load deflection response of one layer Zylon fabric for different orientations of the thicker blunt nose.

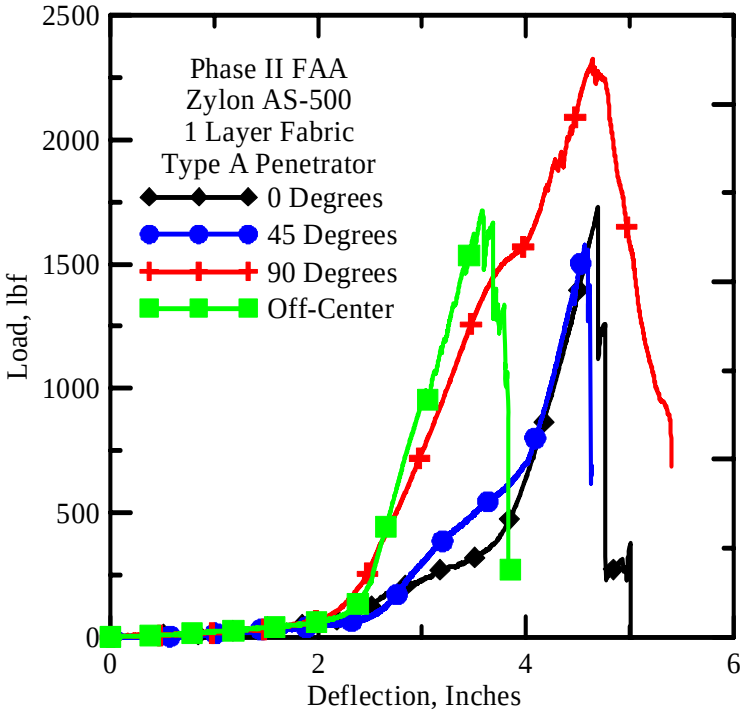

Figure 3.42: Load Deflection for various orientations of thicker blunt nose with one Layer Zylon AS-500

Examination of figure 3.42 indicates that maximum loads at failure differ for various orientations of blunt nose for the same number of layers. The load is maximum at 90 degrees orientation of the blunt nose and is fairly constant at all the other orientations.

However, the 90 degree orientation has the least stiffness value while the 45 degree orientation has the maximum stiffness value. The figure also shows that stiffness of Zylon (lb/in) remains fairly constant up to the fracture of the first yarn of the fabric. Table 3.6 shows the stiffness values for multi layered Zylon specimens for various orientations of the thicker penetrator. The maximum load for the off-center orientation of the blunt nose lies closer to the maximum load of the 0 degrees orientation with deviations of 14, 87 and 59 lbs for 1, 4 and 8 layer respectively. The stiffness for the off-center orientation lies between the 45 and 90 degree orientation stiffness.

Table 3.6: Maximum Load & Stiffness for Zylon AS-500 for Thicker Penetrator

Layers	**Orientation**	**Maximum Load**	**Stiffness, lb/in**
1	0	1730	1609
1	45	1577	1740
1	90	2324	975
1	Off	1716	1459
4	0	7363	5692
4	45	6279	7349
4	90	8957	5669
4	Off	7276	6647
8	0	13290	11382
8	45	9952	12436
8	90	15669	10025
8	Off	13349	11645

The responses for 4 and 8 layers of Zylon AS-500 fabric using the thicker penetrator are plotted in figures 3.43 and 3.44 respectively. These responses are similar to the one layer results for Zylon.

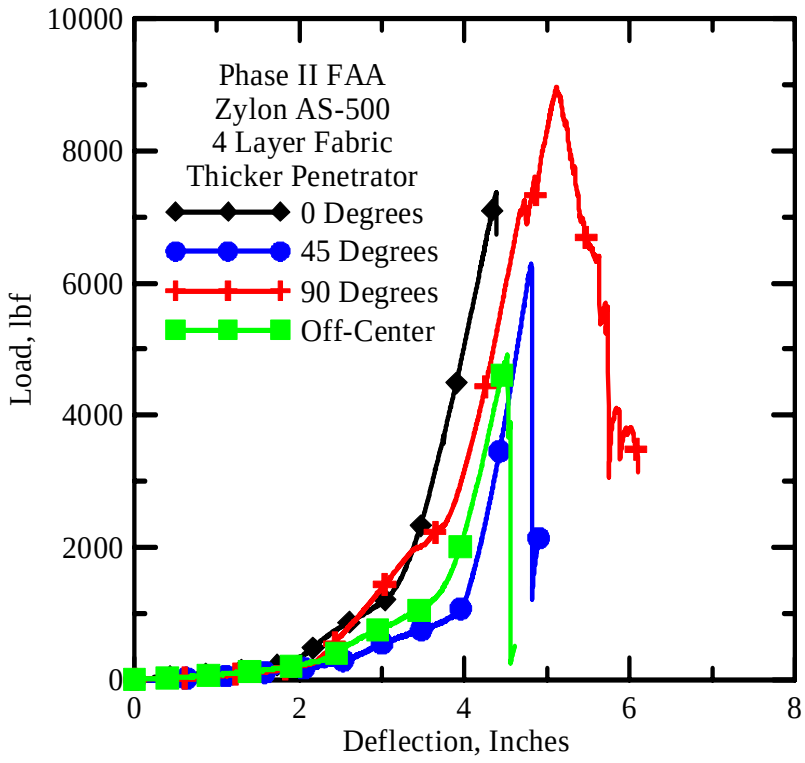

Figure 3.43: Various Orientations of thicker blunt nose - 4 Layer Zylon Fabric

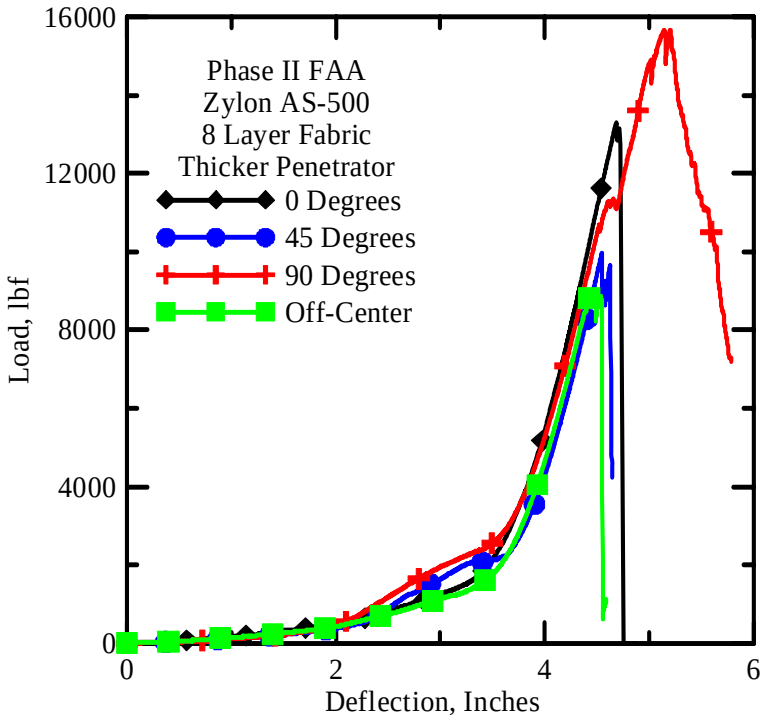

Figure 3.44: Various Orientations of thicker blunt nose - 8 Layer Zylon Fabric

The figures 3.45 and 3.46 show that for the energy absorbed/areal density and normalized energy absorbed/areal density graphs for Zylon AS-500 samples tested using the type A penetrator, the 90 degree orientation is most predominant while the off center orientation is fairly similar to the 0 degree orientation. The 45 degree orientation shows the least energy absorption. Figure 3.47 and 3.48 indicate the peak load versus number of plies and peak load normalized by areal density versus the number of plies respectively. This trend is similar to the energy absorption capacity discussed above. Figure 3.49 and 3.50 show the stiffness versus number of plies as well as linearly extrapolated stiffness values specific stiffness versus the number of plies respectively. The linear extrapolations agree significantly with the experimental values except for the 90 degree orientation.

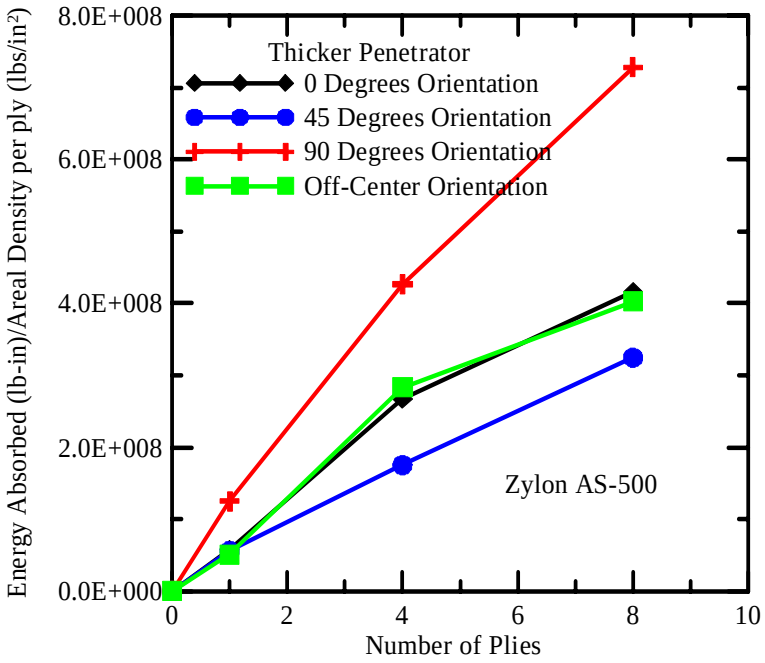

Figure 3.45: Energy absorbed/areal density graphs of 1, 4 and 8 ply Zylon for thicker penetrator

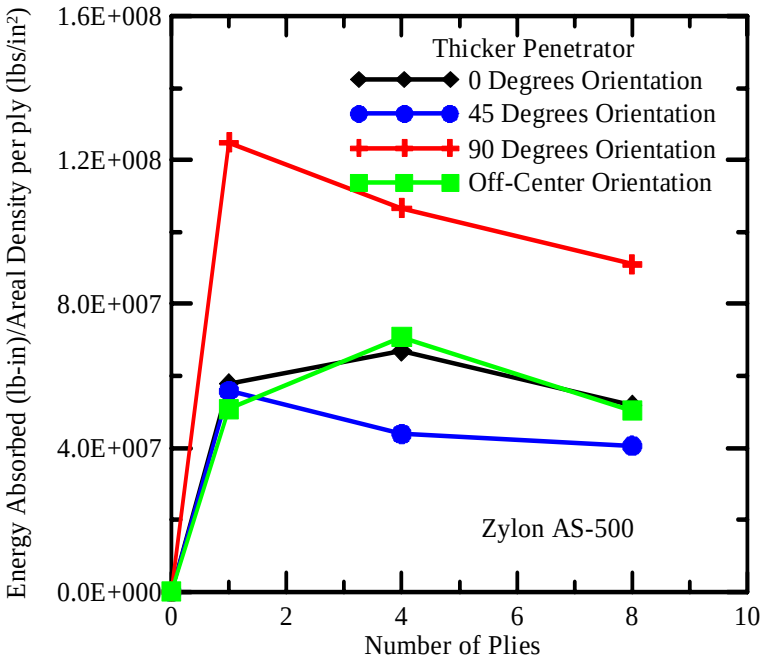

Figure 3.46: Energy absorbed/areal density graphs of 1, 4 and 8 ply Zylon samples normalized by no of plies for thicker penetrator

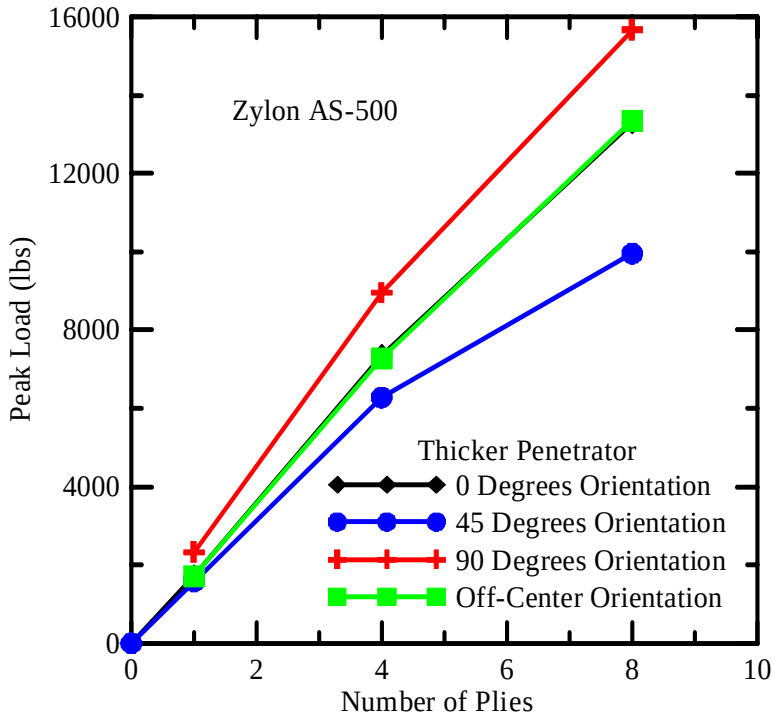

Figure 3.47: Number of plies vs. peak load for Zylon using thicker penetrator

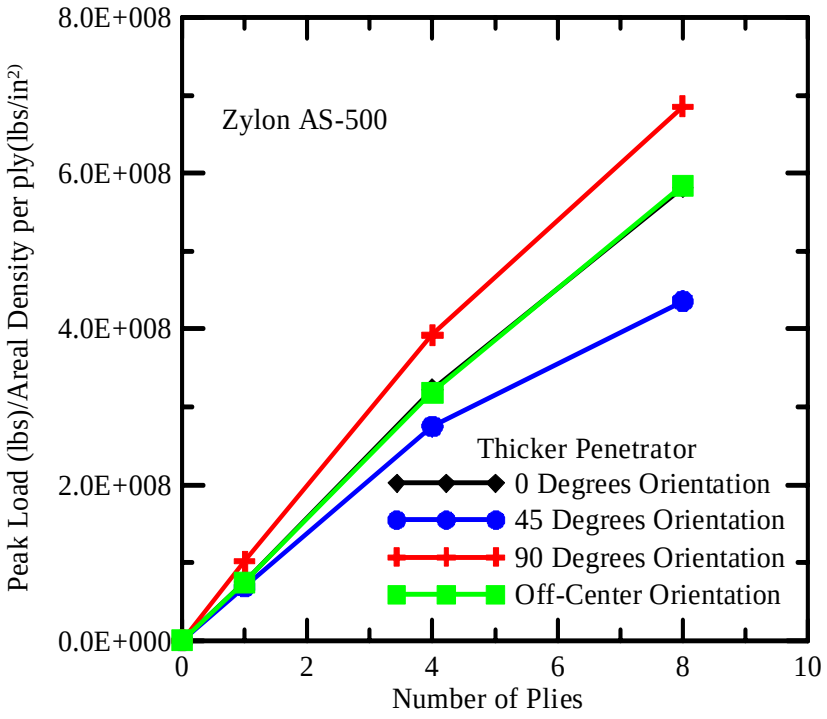

Figure 3.48: Number of plies vs. normalized peak load for Zylon using thicker penetrator

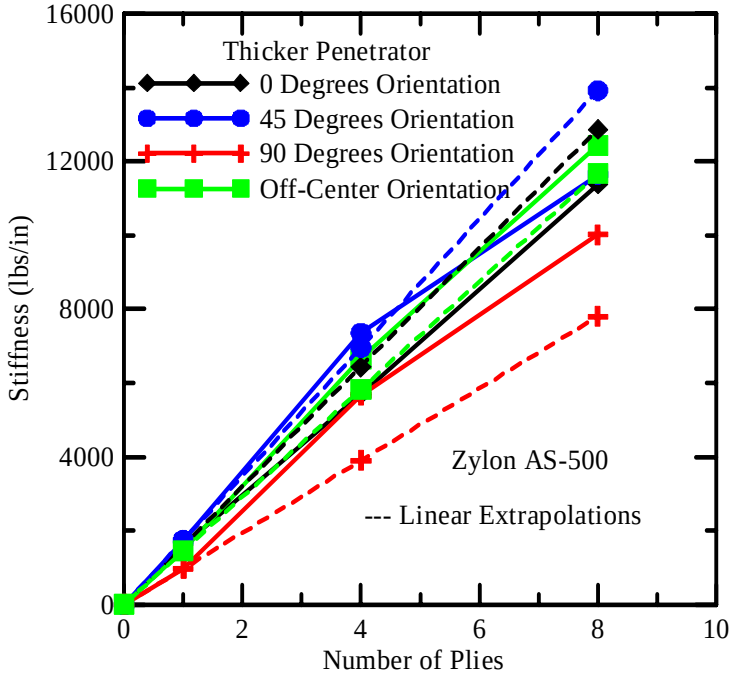

Figure 3.49: Number of plies vs. stiffness for Zylon using thicker penetrator (actual and linearly extrapolated)

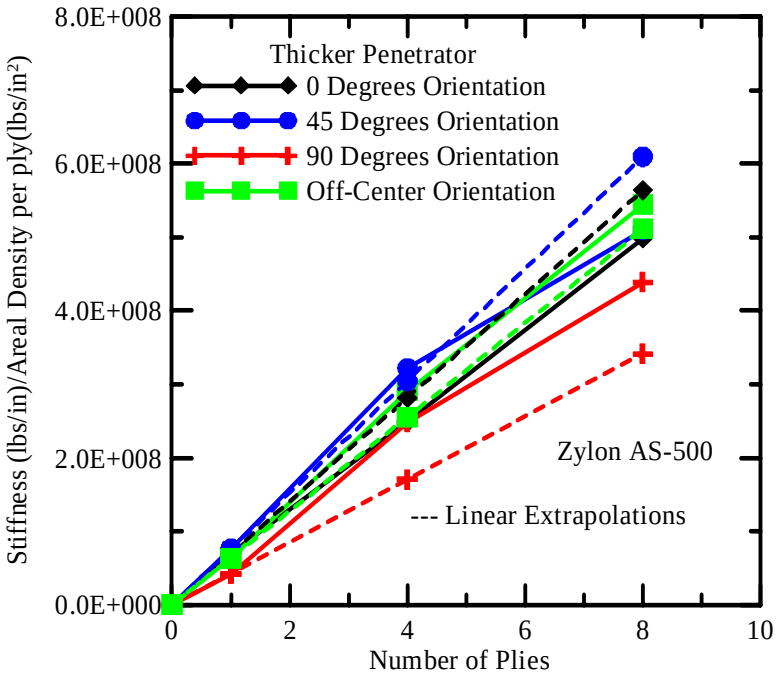

Figure 3.50: Number of plies vs. normalized stiffness for Zylon using thicker penetrator (actual and linearly extrapolated)

Thinner Penetrator

The load deflection curves for 1, 4, and 8 layer Zylon AS-500 specimens for the off center orientation using the thinner penetrator are shown in figure 3.51.

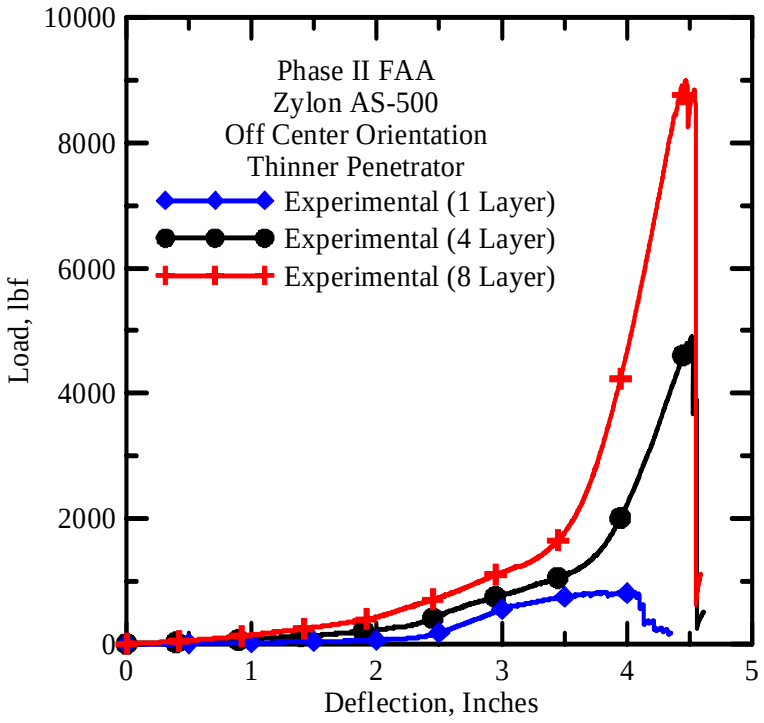

Figure 3.51: Load Deflection response of Zylon As-500 for same orientation of thinner blunt nose for multi-layer specimens

837, 4916 and 9000 lbs are the peak loads with the thinner penetrator were for 1, 4 and 8 layers respectively. The figure 3.52 shows load-deflection plot for various orientations of thinner blunt nose with one layer of Zylon AS-500.

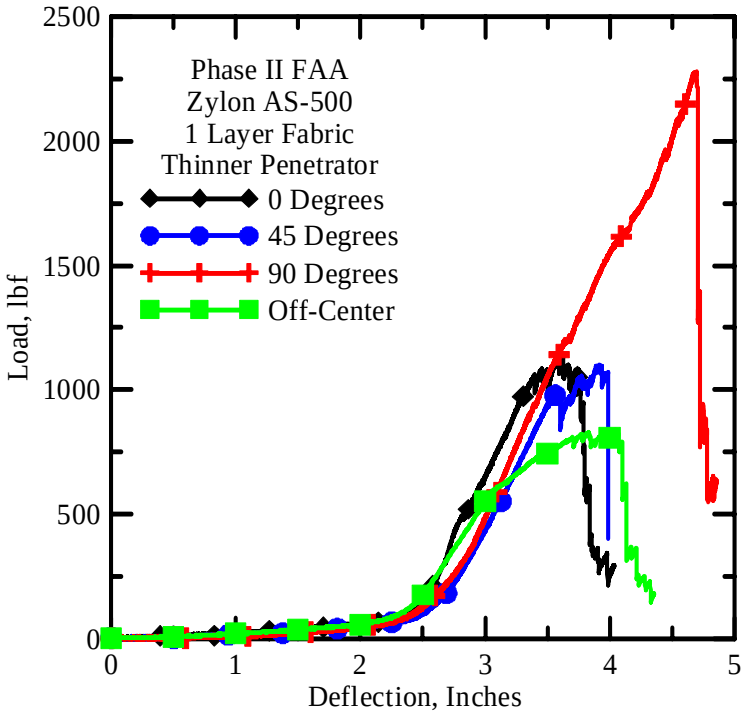

Figure 3.52: Load Deflection for various orientations of thinner blunt nose with one Layer Zylon AS-500

The above plot shows that for the thinner penetrator, the maximum load at failure occurs at the 90 degree orientation. Maximum stiffness occurs for the 90 degree orientation of the blunt nose and is minimum at the off center orientation. The 90 degree orientation peak load is about 2.5 times higher than the minimum peak load. For multi-layered Zylon AS-500 fabrics using the thinner penetrator, similar results as the one layer were obtained. These plots for the multi-layered Zylon AS-500 fabric for different orientations are shown in figures 3.53 and 3.54. Table 3.7 shows the values of the maximum loads and stiffness for the thinner penetrator.

Table 3.6: Maximum Load & Stiffness for Zylon AS-500 for Thinner Penetrator

Layers	Orientation	Maximum Load	Stiffness, lb/in
1	0	1138	1013
1	45	1100	1034
1	90	2278	1148
1	Off	837	755
4	0	5173	5096
4	45	7380	5151
4	90	8729	5499
4	Off	4916	4658
8	0	9446	10149
8	45	12948	8820
8	90	16649	13525
8	Off	9000	8394

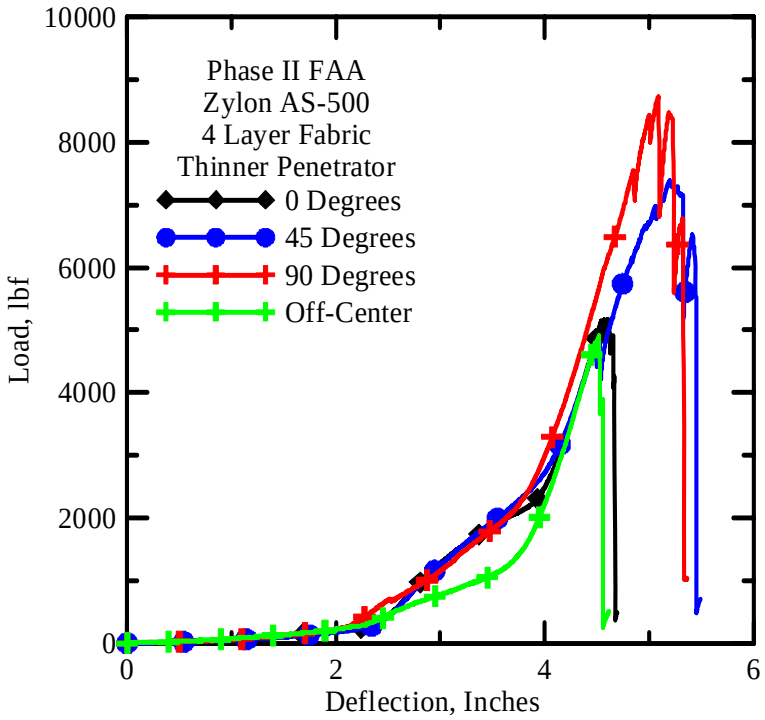

Figure 3.55: Various Orientations of thinner blunt nose - 4 Layer Zylon AS-500 Fabric

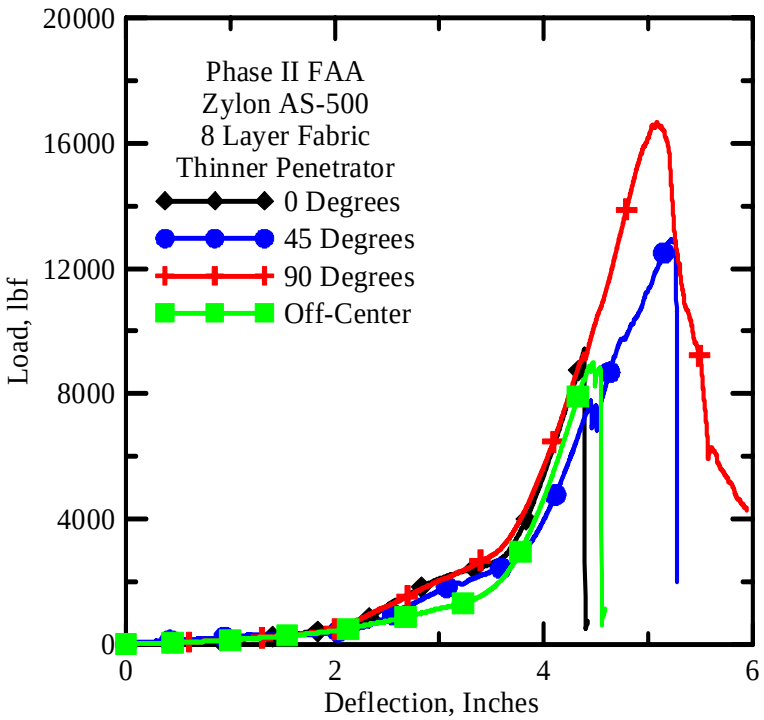

Figure 3.56: Various Orientations of thinner blunt nose - 8 Layer Zylon AS-500 Fabric

The energy absorbed/areal density and normalized energy absorbed/areal density graphs for Zylon AS-500 samples using the thinner penetrator are plotted in figures 3.57 and 3.58. The off center orientation shows the least energy absorption capacity while the angled orientations (45 and 90) show the greatest energy absorption capacity. There is a significant non linearity in normalized specific energy. The graph of the peak load versus number of plies for Zylon AS-500 using the Type B Penetrator shown in figure 3.59 indicate linear increase in the peak load with increase in the number of layers. The figure indicates that the peak loads for 90 degree orientations are significantly higher as compared to the other orientations. Figure 3.60 represents the peak load normalized by areal density for the tested Zylon AS-500 samples. Figure 3.61 represents the stiffness versus number of plies as well as linearly extrapolated stiffness values for Zylon AS-500 samples using the thinner blunt nose. Figure 3.62 shows stiffness versus number of plies as well as linearly extrapolated stiffness values for Zylon AS-500 samples using the thinner blunt nose with the stiffness value normalized with the areal density for Zylon AS-500. The figures 3.61 and 3.62 indicate that the linear extrapolation of stiffness grossly under predicts the actual stiffness for the 90 degree orientation and the off center orientation.

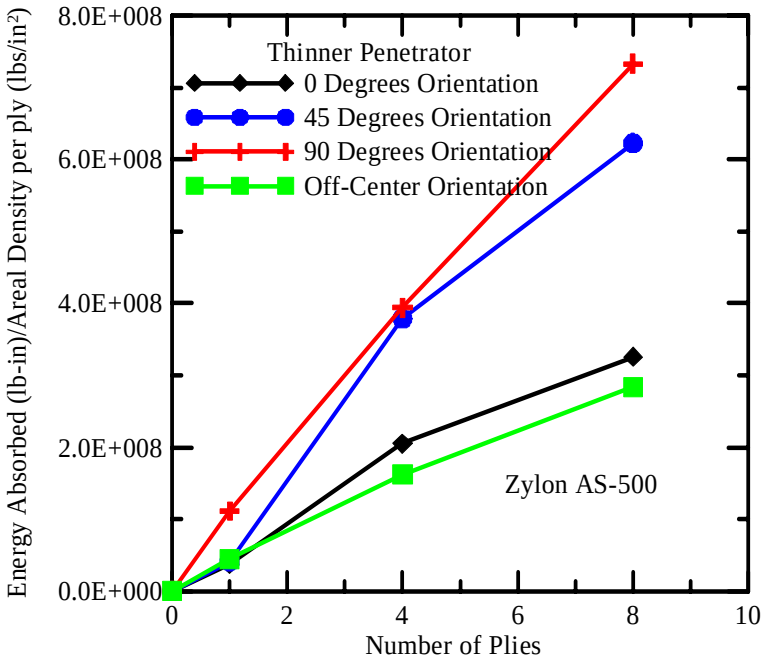

Figure 3.57: Energy absorbed/areal density graphs of 1, 4 and 8 ply Zylon for thinner penetrator.

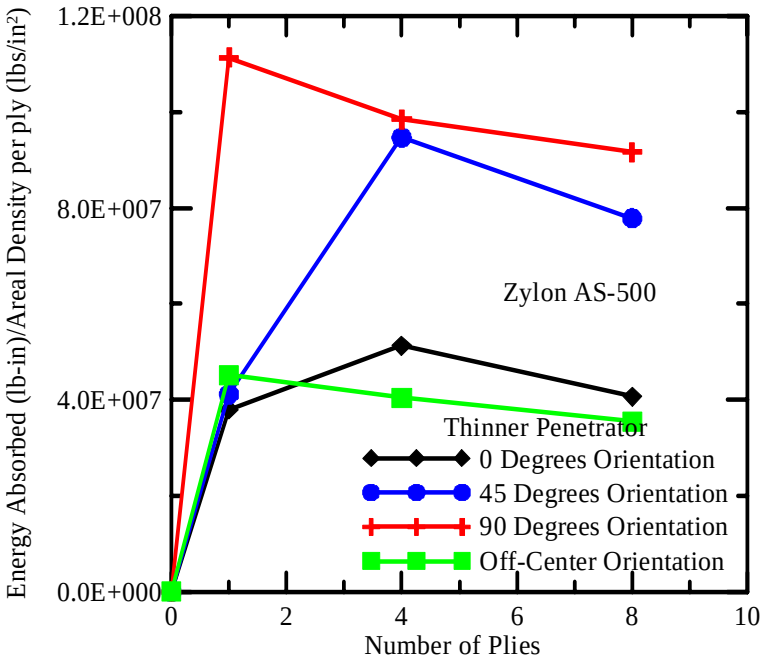

Figure 3.58: Energy absorbed/areal density graphs of 1, 4 and 8 ply Zylon samples normalized by Number of plies for thinner penetrator

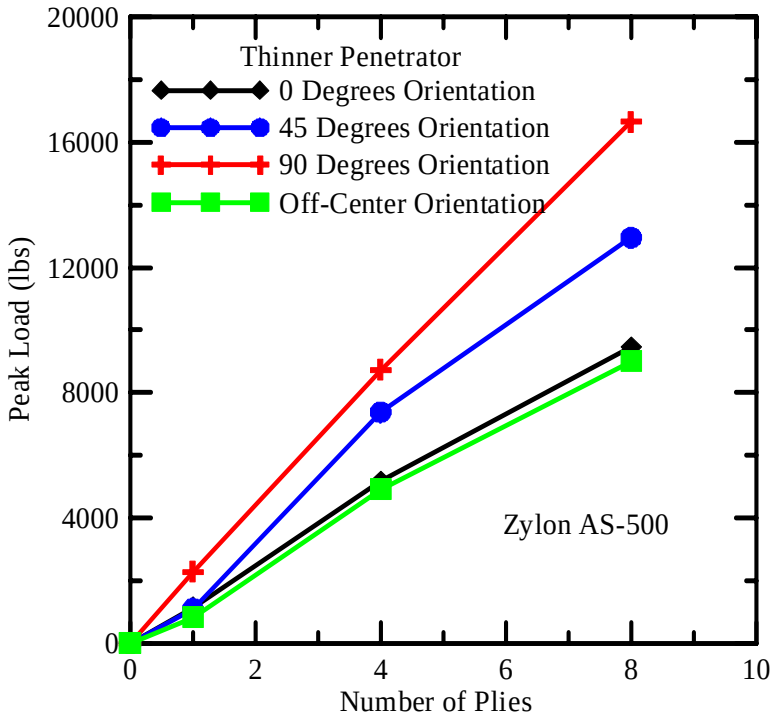

Figure 3.59: Number of plies vs. peak load for Zylon using thinner penetrator

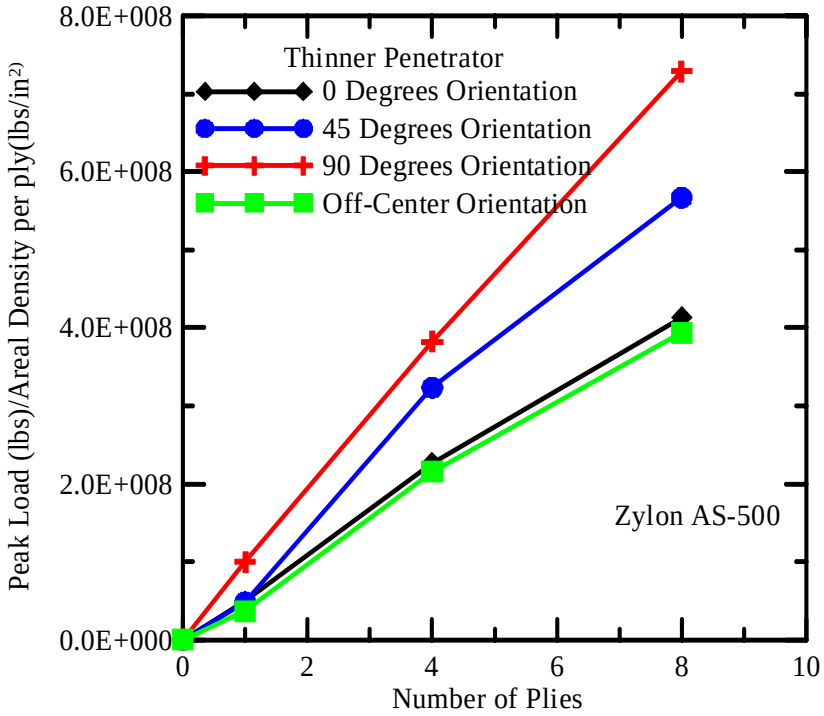

Figure 3.60: Number of plies vs. normalized peak load for Zylon using thinner penetrator

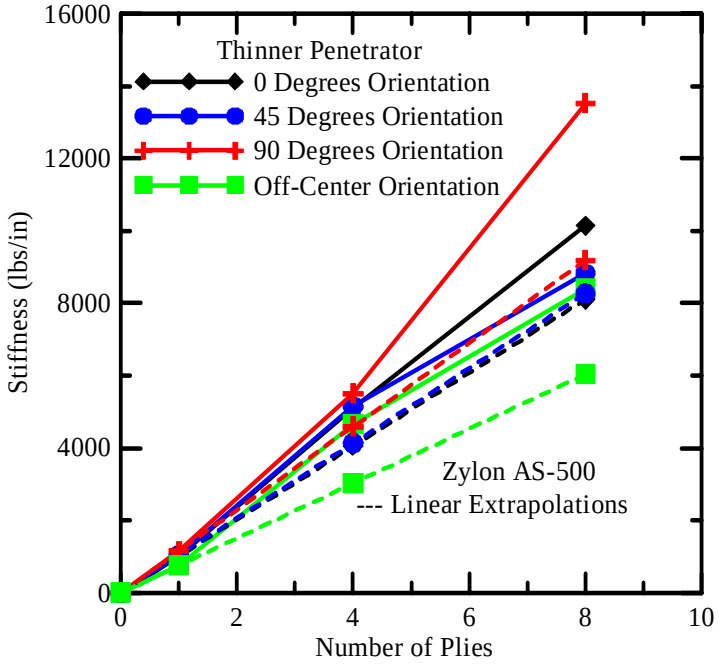

Figure 3.61: Number of plies vs. stiffness for Zylon using thinner penetrator (actual and linearly extrapolated)

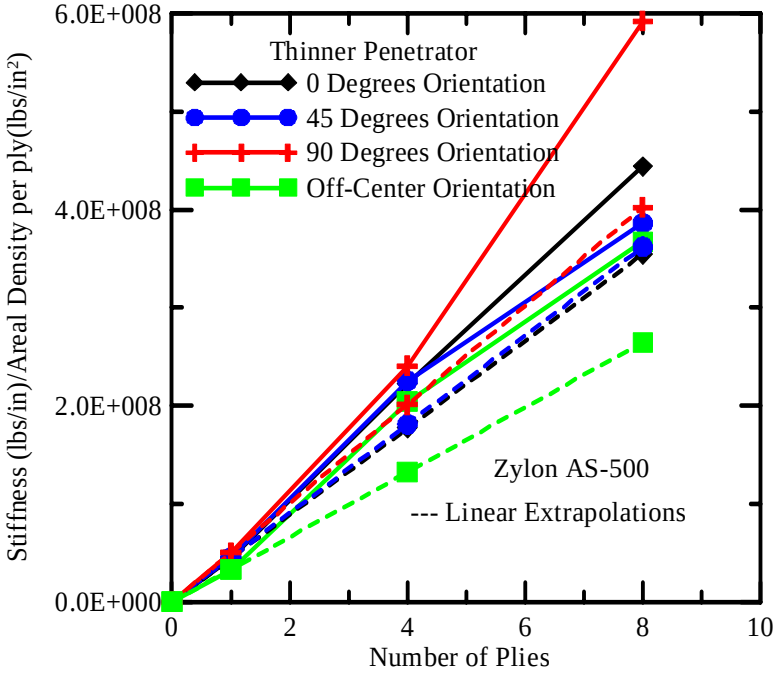

Figure 3.62: Number of plies vs. normalized stiffness for Zylon using thinner penetrator (actual and linearly extrapolated)

Penetrator (Blunt Nose) Comparison

Slack Adjustment

The figures 3.63 and 3.64 show the typical load defection curve obtained for a Zylon AS-500 sample tested at 45 degrees orientation using the thicker(Type A) and thinner(Type B) penetrator.

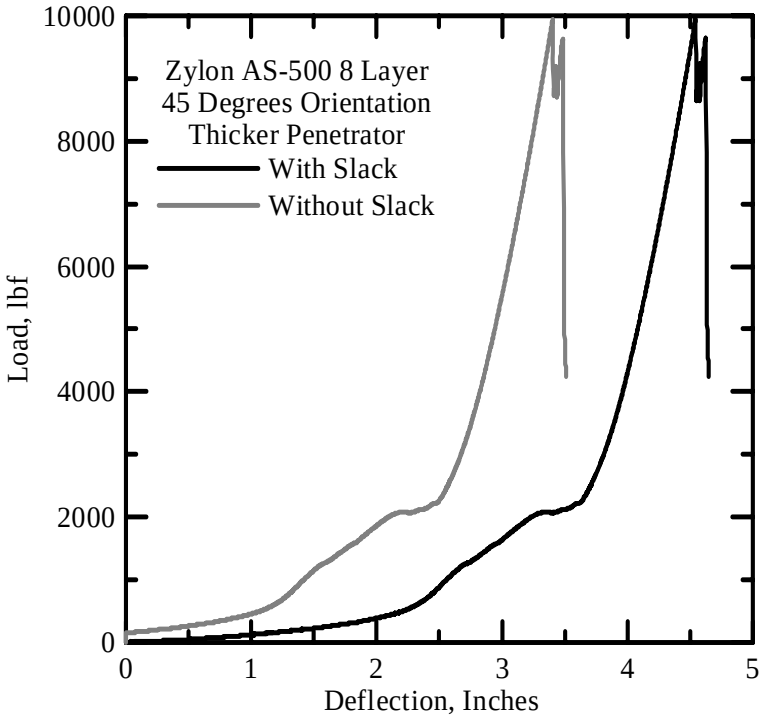

Figure 3.63: Load-deformation response of eight layer Zylon AS-500 specimen with and without slack adjustment with thicker penetrator.

The slack adjustment was achieved by shifting the raw data load deflection curves along the x-axis so that the curve obtained would coincide with initial portion of the load deflection curve obtained from finite element analysis models prepared as simulations for the static ring tests for various orientations of the blunt nose. Both these curves have

been slack shifted by 1.1397 and 0.6061 inches respectively to match the displacements obtained through the finite element model.

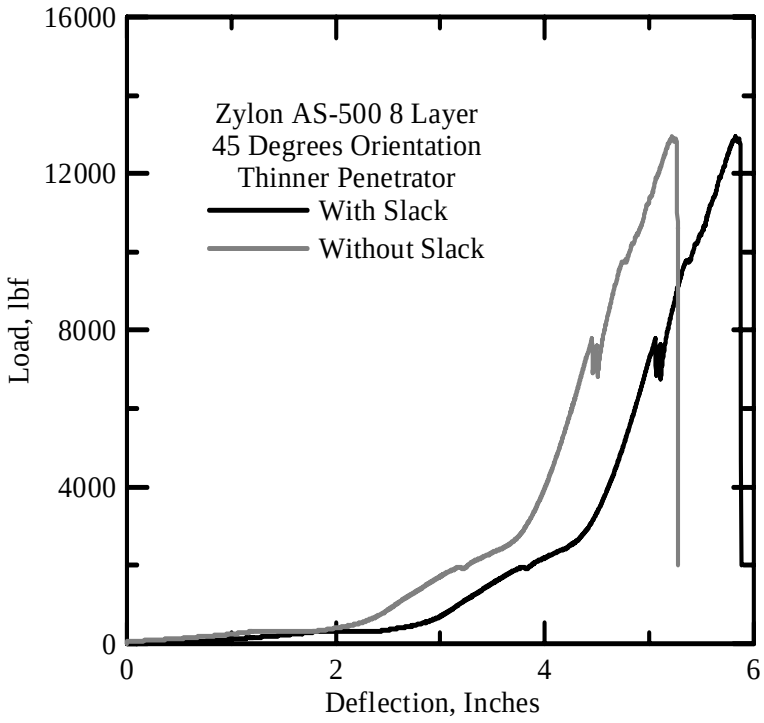

Figure 3.64: Load-deformation response of eight layer Zylon AS-500 specimen with and without slack adjustment with thinner penetrator

Load Deflection Responses

The load deflection responses using the two different penetrators are plotted in the following section. They show the comparison of the results for the same number of layers with the same orientation using different penetrators.

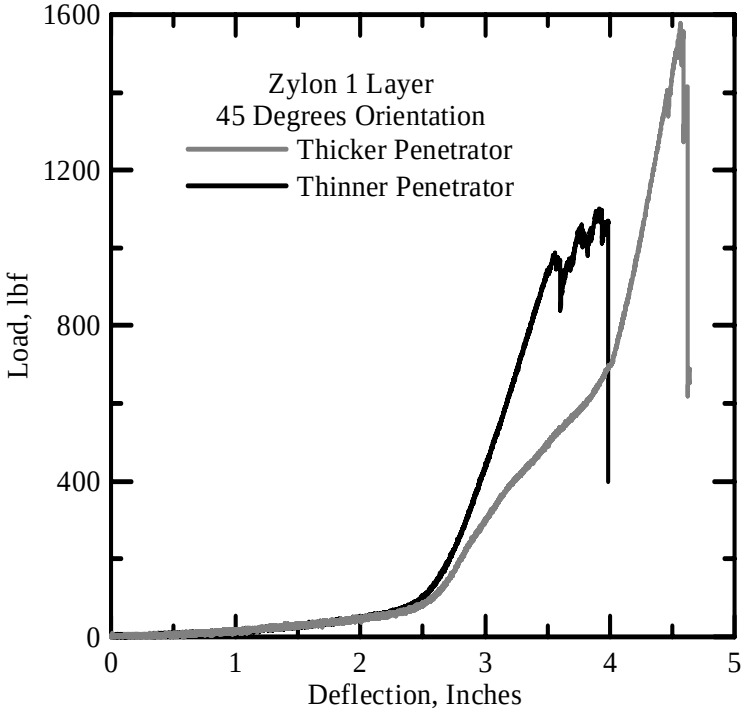

Figure 3.65: One Layer Zylon – 45 Degrees Orientation – Both Penetrators

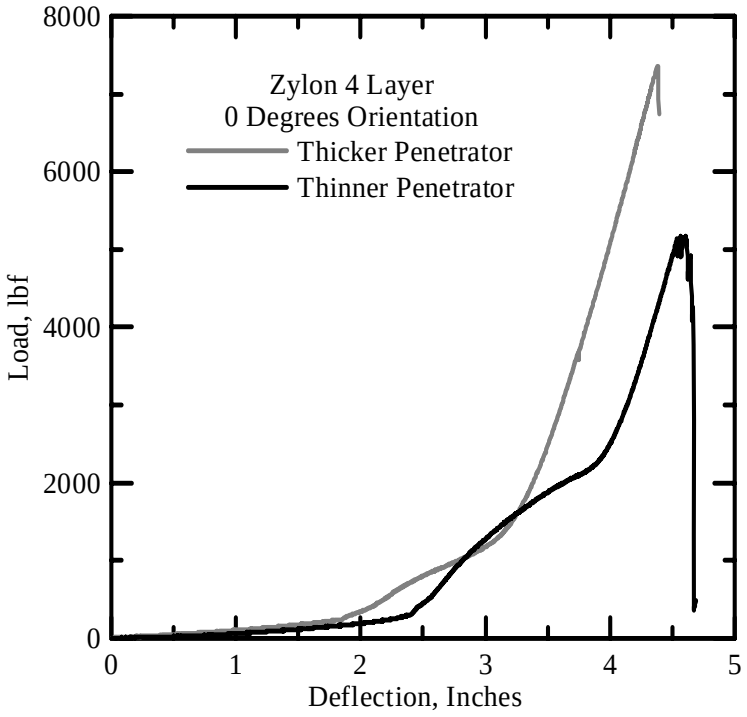

Figure 3.66: Four Layer Zylon – 0 Degrees Orientation – Both Penetrators

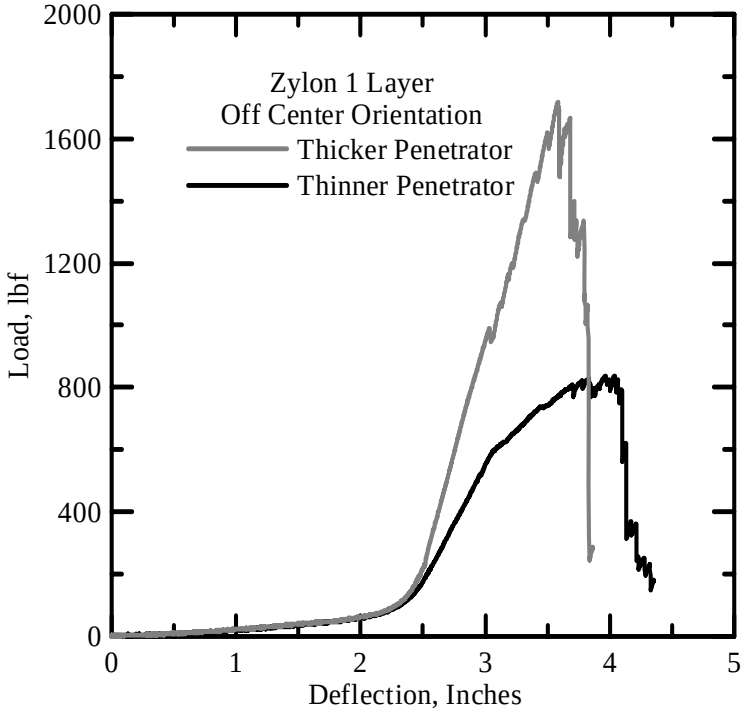

Figure 3.67: One Layer Zylon – Off Center Orientation – Both Penetrators

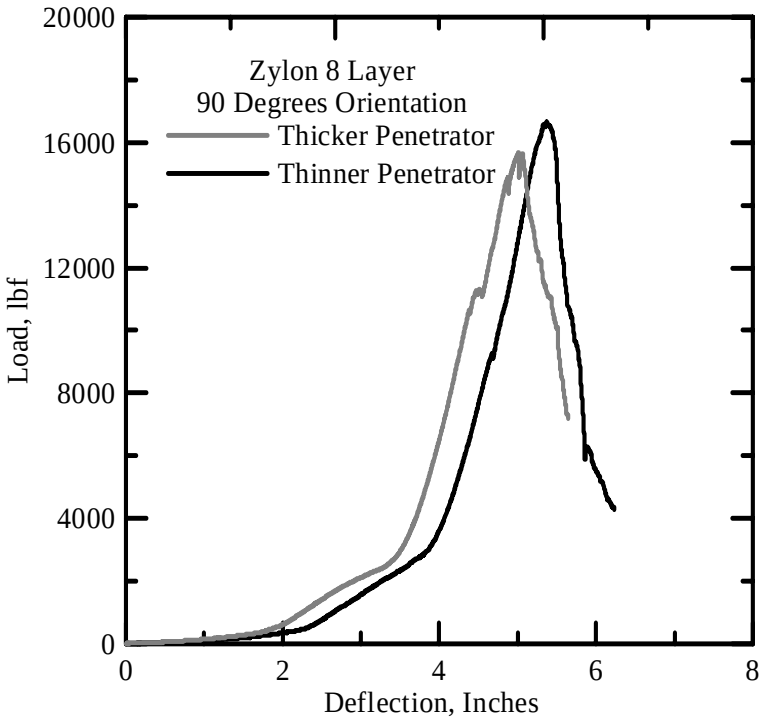

Figure 3.68: Eight Layer Zylon – 90 Degrees Orientation – Both Penetrators

The figures 3.65, 3.66 and 3.67 shows that the maximum load obtained for the thinner penetrator is less than the maximum load obtained for the thicker penetrator. Similarly, the stiffness of the Zylon AS-500 with the thicker penetrator is higher than the stiffness with the thinner penetrator. It was obtained that the peak loads and highest stiffness for Zylon AS-500 samples using the thicker (Type A) penetrator was generally higher than that obtained for the thinner (Type B) penetrator specimens. A difference in this trend was observed in the 90 orientation as shown in figure 3.68. The maximum loads obtained with both the penetrators differ marginally for the 90 degree orientation. This may be attributed to the shear loading of the Zylon AS-500 specimens in the 90 degrees orientation as well as the inverted V Shape configuration of the blunt nose.

3.2.4 Zylon AS-500 Static Tests Result Summary

The table 3.8 the results of static ring tests conducted on Kevlar AS-49 for various orientations of the blunt nose using the thicker penetrator for different number of layers (1, 4 and 8). Table 3.9 summarizes the results for the thinner penetrator. The tables clearly indicate that the 90 degree orientation have the least apparent load at first failure. The tables also show that as the number of layers increase for a constant orientation, the post peak response gradually increases. Tables 3.4 and 3.5 also indicate that the strokes at peak loads become fairly constant as the number of layers increases for the same orientation

3.8: Zylon AS-500 Static Ring Test Results for Thicker (Type A) Penetrator

Blunt Nose Orientation	No of layers	Load at First Failure (lb)	Stroke at First Failure (lb)	Peak Load (lb)	Stroke at Peak Load (in)	Stiffness (lb/in)	Area under the curve (lb/in)	
							Pre Peak	Post Peak
0	1	1730	4.69	1730	4.69	1609	1323	162
0	4	7363	4.39	7363	4.39	5692	6105	56
0	8	13290	4.69	13290	4.69	11382	9499	410
45	1	1397	4.47	1577	4.57	1740	1274	86
45	4	6216	4.80	6279	4.81	7349	4003	191
45	8	9877	4.53	9952	4.55	11645	7414	875
90	1	1917	4.28	2324	4.64	975	2853	1179
90	4	7143	4.71	8957	5.12	5669	9745	5778
90	8	11289	4.64	15669	5.15	10025	16629	7480
Off	1	984	3.03	1716	3.58	1459	1159	353
Off	4	6750	4.44	7276	4.52	6647	6469	465
Off	8	13243	4.67	13349	4.69	12436	9192	735

For all the twenty one tests, the blunt nose end conditions were fixed-fixed and clamps were used during testing for all cases. A preload of 250 lbs was applied in case of all the samples to account for the 3” limit to the actuator movement.

3.9: Zylon AS-500 Static Ring Test Results for Thicker (Type B) Penetrator

Blunt Nose Orientation	No of layers	Load at First Failure (lb)	Stroke at First Failure (lb)	Peak Load (lb)	Stroke at Peak Load (in)	Stiffness (lb/in)	Area under the curve (lb/in)	
							Pre Peak	Post Peak
0	1	973	3.31	1138	3.62	1013	869	265
0	4	5048	4.58	5173	4.57	5096	4694	514
0	8	9386	4.52	9446	4.52	10149	7441	40
45	1	977	3.56	1100	3.92	1034	940	76
45	4	4750	4.51	7380	5.19	5151	8651	1731
45	8	7708	5.05	12948	5.83	8820	14225	1879
90	1	2268	4.68	2278	4.70	1148	2543	118
90	4	7523	5.14	8729	5.37	5499	9003	1802
90	8	9140	4.65	16649	5.37	13525	16744	7900
Off	1	807	3.71	837	4.04	755	1033	126
Off	4	4788	4.49	4916	4.52	4658	3700	175
Off	8	8868	4.45	9000	4.47	8394	6490	768

3.3 Static Ring Test Observations

The following inferences can be drawn from the static ring tests

1) The initial portion of the graphs represents the force required to overcome the crimp in the fabric. The “knee” in the Static Test results represents the slippage that occurs in the Static Test. This phenomenon is more prominent in Zylon AS-500 as compared to Kevlar AS-49.

2) Zylon AS-500 results show more energy absorption capacity than the corresponding Kevlar AS-49 specimens.
3) The effect of the inverted V shape configuration of the blunt nose is predominant to a greater extent in Zylon AS-500.
4) Zylon AS-500 samples show more slack and crimp as compared to the Kevlar AS-49 specimens.
5) The 90 degree orientations of the blunt nose show results that deviate from possible accepted results.
6) The peak loads and stiffness are higher for the thicker (Type A) penetrator.

Chapter 4: Friction Tests

4.1 Introduction to the Friction Tests

Static ring tests were run on Kevlar AS-49 and Zylon AS-500 specimens for various orientations of the blunt nose and for various number of fabric layers. The figure 4.1 shows the load deflection response of 1, 2, 4, 8 and 24 ply Kevlar samples that were tested with the thicker penetrator for the zero degrees orientation.

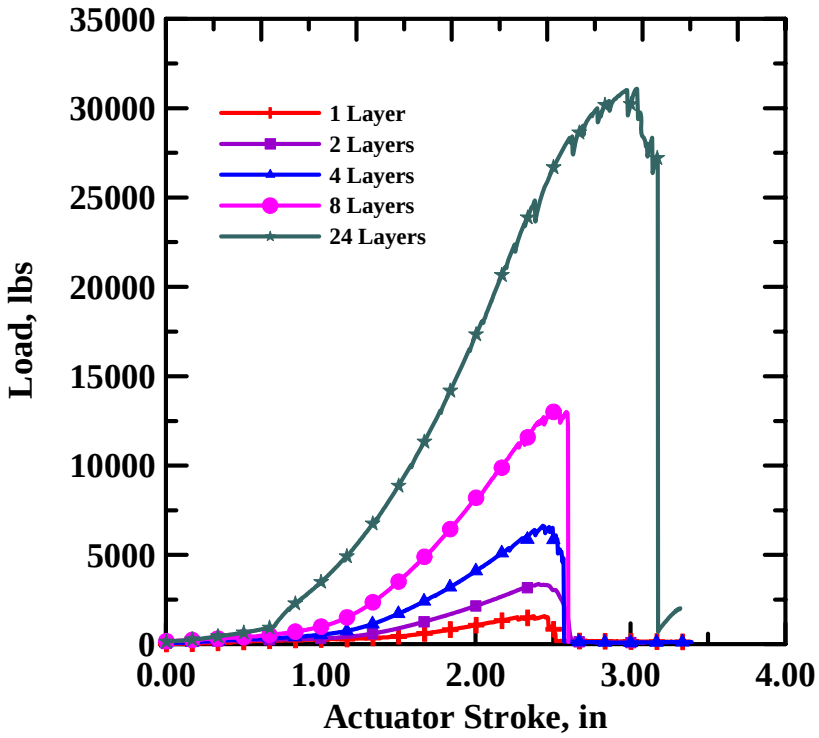

Figure 4.1: Load-deformation response of 1, 2, 4, 8 and 24 ply Kevlar samples

Although the peak load seems to scale proportional to the number of plies (up to eight plies), these responses may be viewed as highly nonlinear due to the progressive mechanism of failure that is operational in these specimens. It is observed that the two-

ply specimen deviates from the one ply curve at about 1000 lbs, approximately 65 % of the ultimate strength of a single ply. The four-ply specimen deviates from the two-ply at about 1400 lbs, and the eight ply deviates from four plies at about 2000 lbs. This indicates that the contribution of outer plies to the stiffness of the overall assembly does not directly start at the start of the loading cycle. Significant displacement of the inner plies must take place before the outer plies are able to carry the load. This also indicates the importance of parameters such as the coefficient of friction between the plies, which is responsible for the mechanical interlock and thus the transfer of load from one ply onto the other one.

In addition, a number of finite element simulations were run to simulate the experimental static ring tests. These models were on commercial finite element package ABAQUS/Standard. Most of the finite element models were consistent with their experimental counterparts. However, some of the simulations, mainly those run with the 90 degree and 45 degree orientation specimens deviated from the experimental results. This can be attributed to some extent to the contribution of coefficient of friction that exists between the multi-ply specimens.

A series of friction tests were therefore run to compute the coefficient of friction for the three fabrics.

4.1.1 Objectives

The primary objective of static tests is to compute the coefficients of static and dynamic friction between two layers of the same fabric. These tests were conducted by

pulling a sample fabric sandwiched between two fabrics of the same type at a constant rate and at a constant normal load.

4.1.2 Specimen Preparation Procedure

All the three fabrics: Kevlar AS-49, Zylon AS-500 and Zylon AS-1500 were tested to determine the coefficient of friction. Two fabric specimens were required for testing the coefficient of friction. The sample to be tested had dimensions of 2.5" by 30". The other fabric specimen was used 2.5" wide and 60" in length. A wood block 2.75" wide, 5.5" in length and 1.5" in height was used to apply the normal load uniformly over the test area.

4.1.3 Test Procedure

Tests were conducted with help of two test machines namely a 22 Kips and 55 Kips servo-hydraulic test frames operated under closed-loop control. The test procedure was a displacement control test with the rate of displacement of actuator (stroke) set at 2"/min and 6"/min. Digital data acquisition was used to collect data at every 0.5 second from both the actuators. The test was continued until the horizontal actuator traveled its full possible length of 6". The load-deformation results were used to calculate the coefficients of frictions. The schematic setup for the test is shown in figure 4.2.

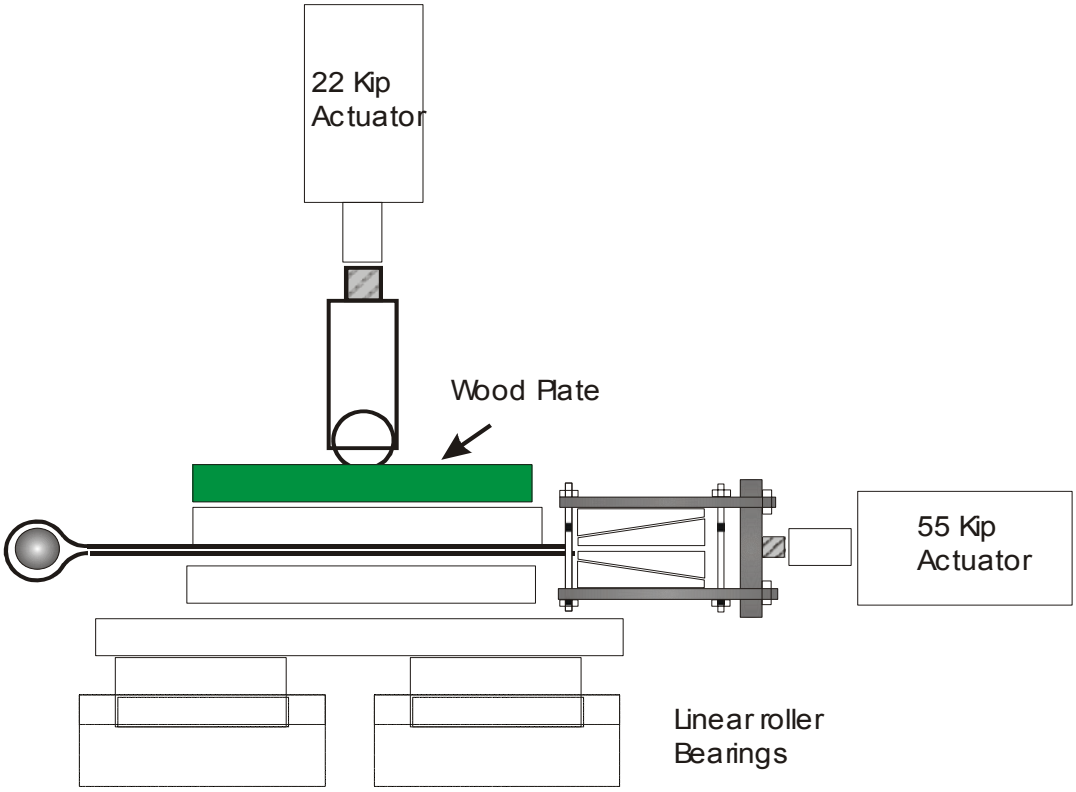

Figure 4.2: Schematic Setup for Friction test

The grip assembly consisted of two steel plates that interlaid the test specimen. The test specimen was held in the assembly through mechanical pressure that was obtained by tightening four threaded rods on the steel plates as shown in the figure 4.3. To avoid damage to the test specimen, the steel plates were covered with rubber so that in the actual experiment, the test specimen was interlaid between two rubber pieces that in turn were fixed on the steel plates.

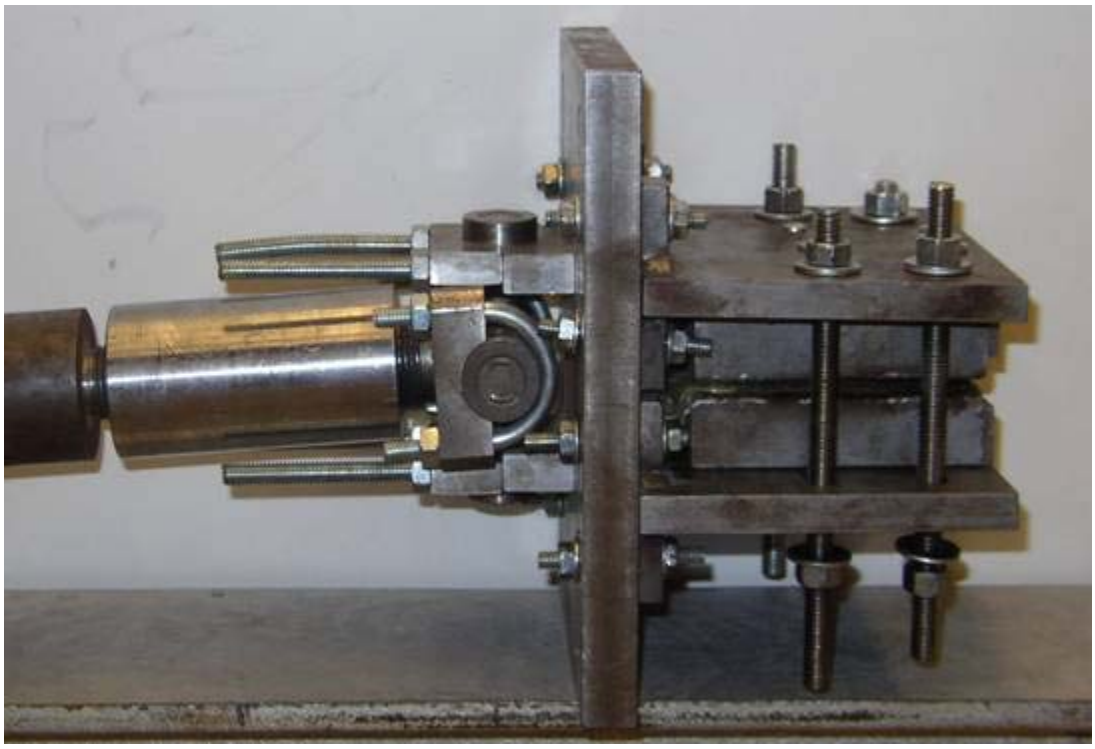

Figure 4.3: Friction Test Gripping Assembly

The testing setup is shown in figure 4.4. The normal loads were applied through another actuator mounted vertically on an I beam resting on to channel sections connected to the four columns as shown in figure 4.4. The second layer of fabric was allowed to move using zinc ball joint rod ends that were fixed to another I beam .This beam was attached to two column sections as seen in the same figure. The fabric was placed on a wooden frame. The wooden frame was allowed to move horizontal along two linear roller bearings that were fixed to the ground.

For the particular experiment, a layer of Kevlar AS-49 fabric was pulled using a 55 kip horizontal actuator and a normal load of 800 pounds was applied throughout the period of the experiment.

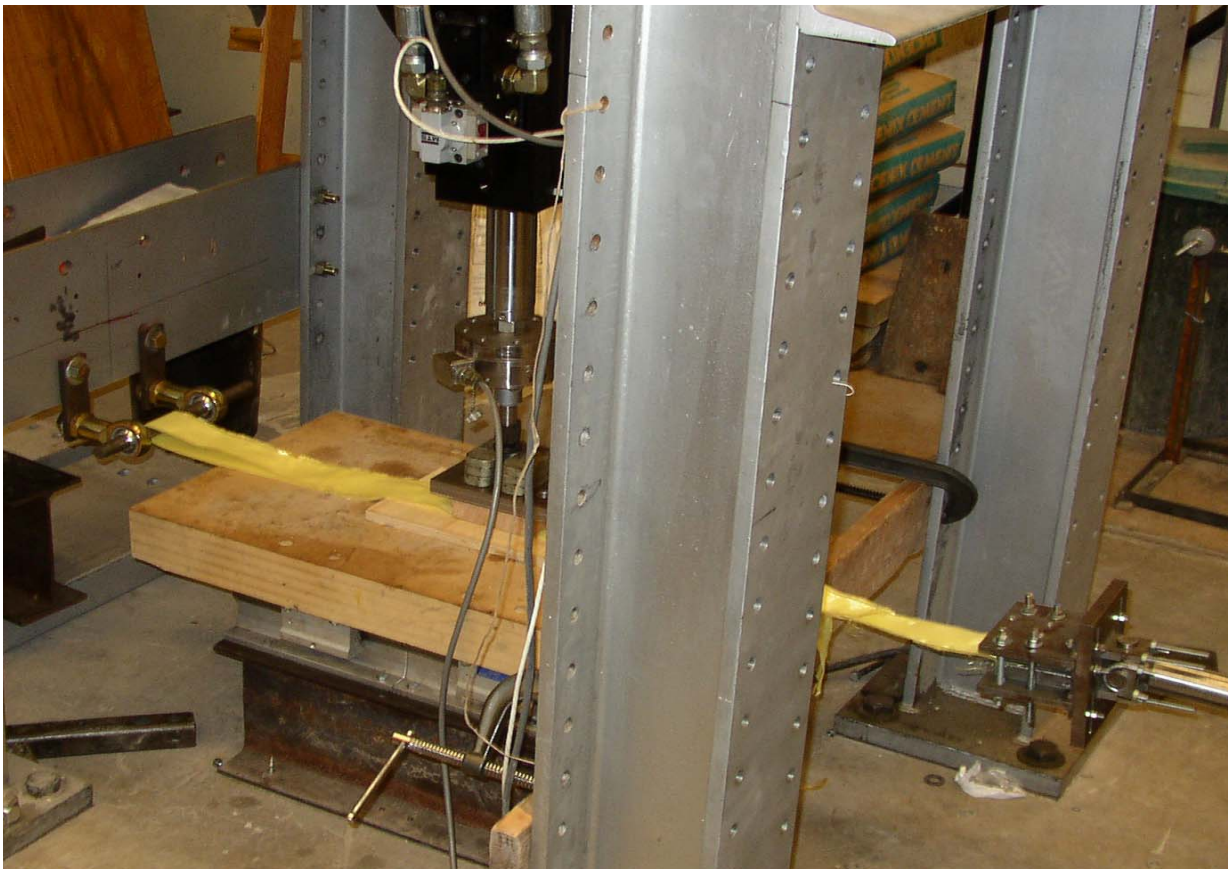

Figure 4.4: The Testing Apparatus

The coefficient of friction was computed by applying these series of normal loads at loading rates of 2.0 in/min and 6.0 in/min. The coefficient of static friction was computed by plotting the maximum pull for each normal load against the respective normal loads. The coefficient of dynamic friction was computed by plotting the average pull for each normal load against the respective normal loads. A typical output from a friction test is shown in figure 4.5

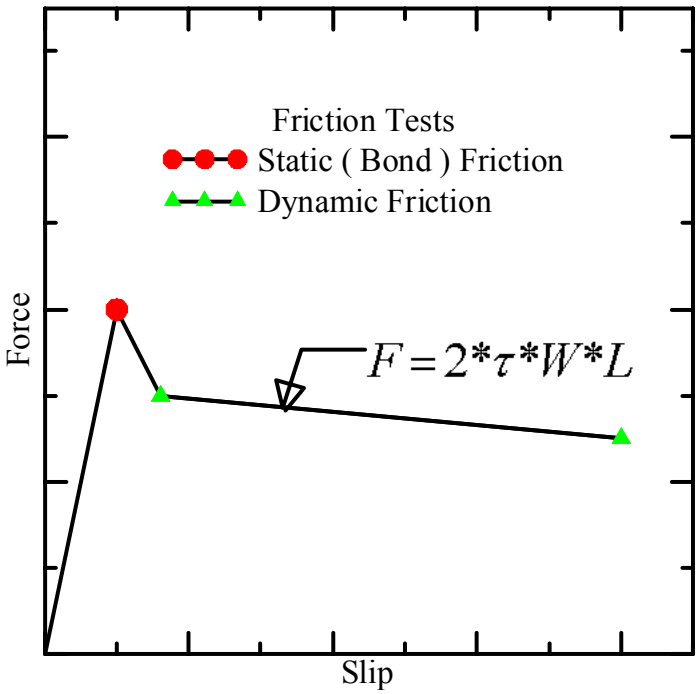

Figure 4.4: A Typical Friction Test Output

4.2 Friction Test Results

The friction tests were run on all three fabrics by varying the displacement rate or pull from 2"/min. to 6"/min. The normal loads applied were 150 lbs, 300 lbs, 500 lbs and 800 lbs for the displacement rates. These normal loads were applied on a contact area of 13.75 square inches. A total number of eight representative tests were run for each fabric with additional six preliminary tests on Kevlar AS-49 and Zylon AS-500 at very low normal loads (15 to 80 lbs).

4.2.1 Kevlar AS-49 Friction Test Results

The following are the results of the friction tests carried out on Kevlar. Figure 4.5 shows the force displacement response of 10 Kevlar samples at 2"/min displacement rate.

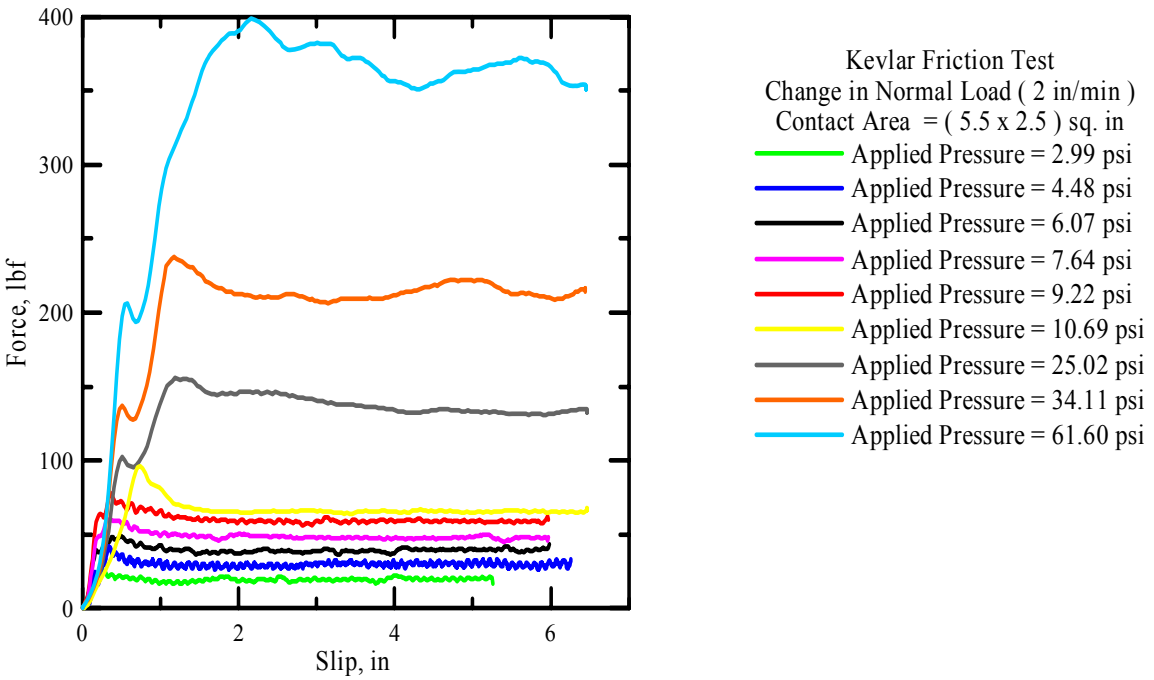

Figure 4.5: Kevlar Friction Tests for Loading Rate of 2.0 in/min.

The following graph shows the coefficient of the friction for samples tested with a loading rate of 2.0 inches per minute. The coefficients of static and dynamic friction are computed taking into account the peak load in the initial part of the test and a constant load towards the end of the test. The friction coefficients are calculated as the slopes of the lines obtained by plotting the average pull loads (both peak and constant) against the normal loads applied.

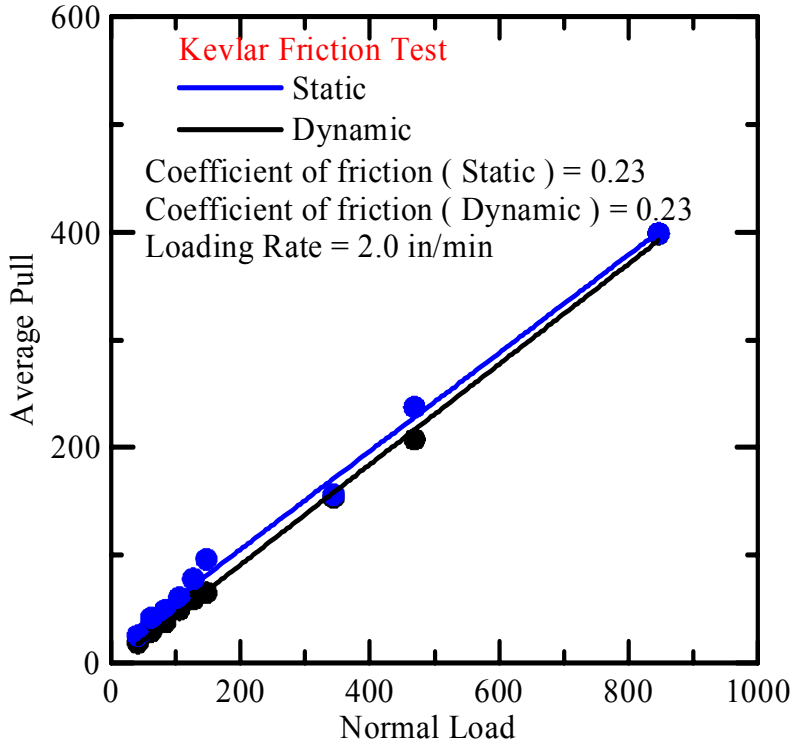

Figure 4.6: Coefficient Of Friction for Kevlar for Loading Rate of 2.0 in/min.

The figure 4.7 shows the results for Kevlar friction test for a loading rate of 6.0 in/min.

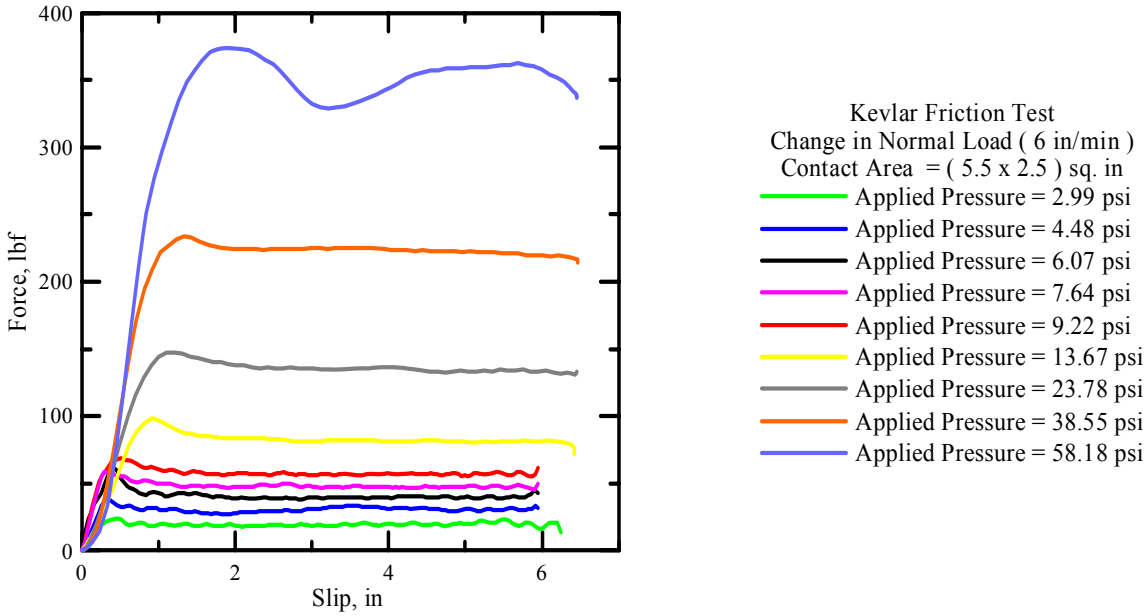

Figure 4.7: Kevlar Friction Tests for Loading Rate of 6.0 in/min.

The coefficients of friction for a loading rate of 6.0 inches per minute are plotted in figure 4.8.

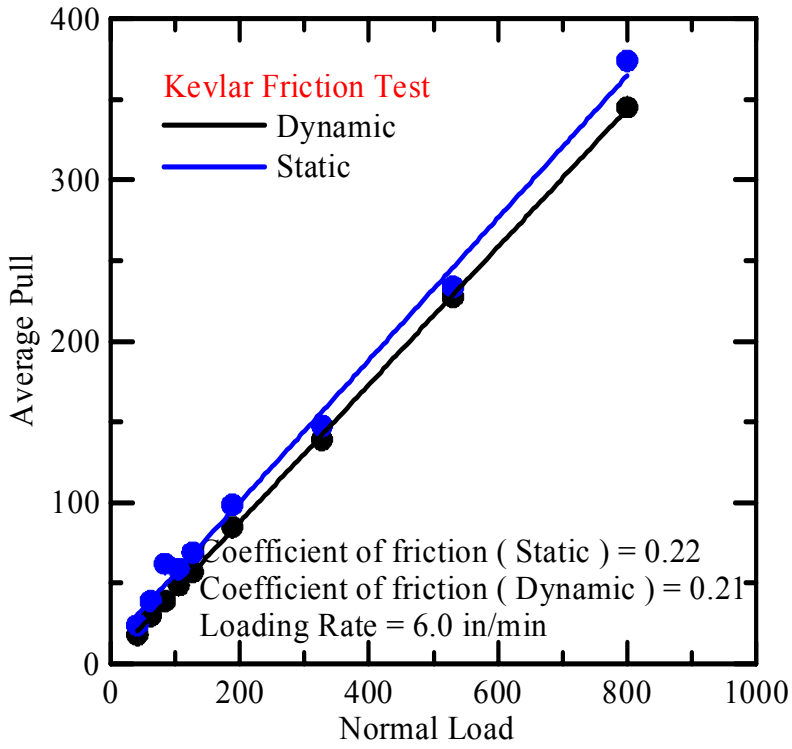

Figure 4.8: Coefficient Of Friction for Kevlar for Loading Rate of 6.0 in/min

The figure 4.9 and 4.10 show the comparison of the static and dynamic coefficient of friction obtained through the Kevlar friction tests for the two different loading rates. The table 4.1 shows the coefficients of friction for the different loading rates

Table 4.1: Comparison of Friction Coefficients for Kevlar AS-49.

Loading Rate	Coefficient of Static Friction	Coefficient of Dynamic Friction
2.0	0.233	0.228
6.0	0.221	0.213

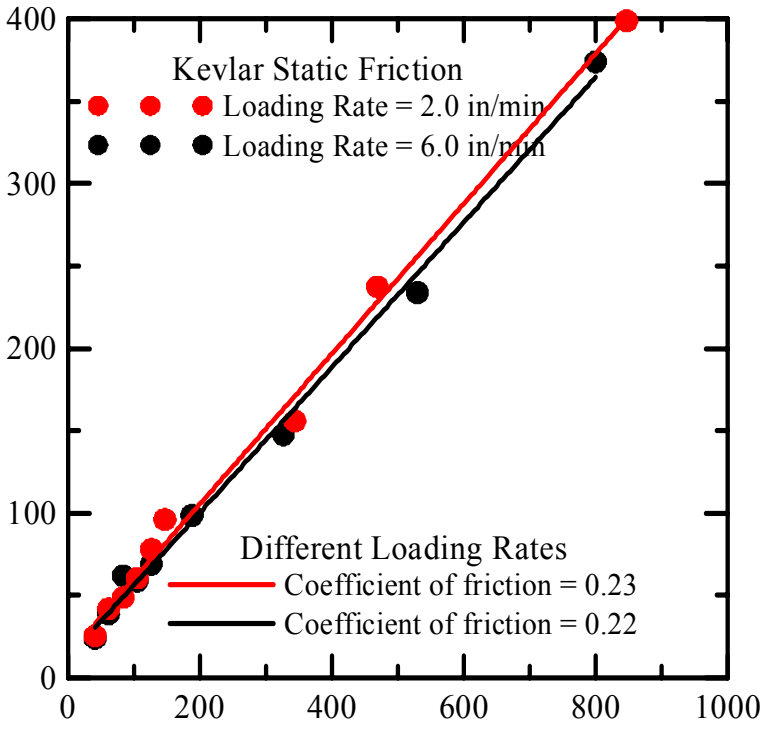

Figure 4.9: Coefficient of Static Friction for Kevlar

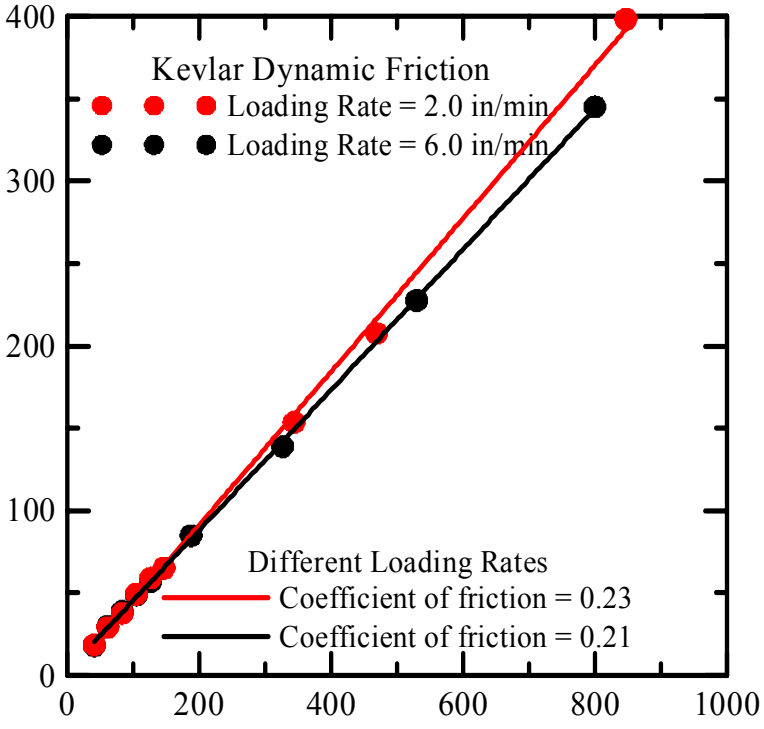

Figure 4.10: Coefficient of Dynamic Friction for Kevlar

4.2.2 Zylon AS-500 Friction Test Results

The following are the results of the friction tests carried out on Zylon AS-500. Figure 4.11 shows the force displacement response of ten Zylon samples.

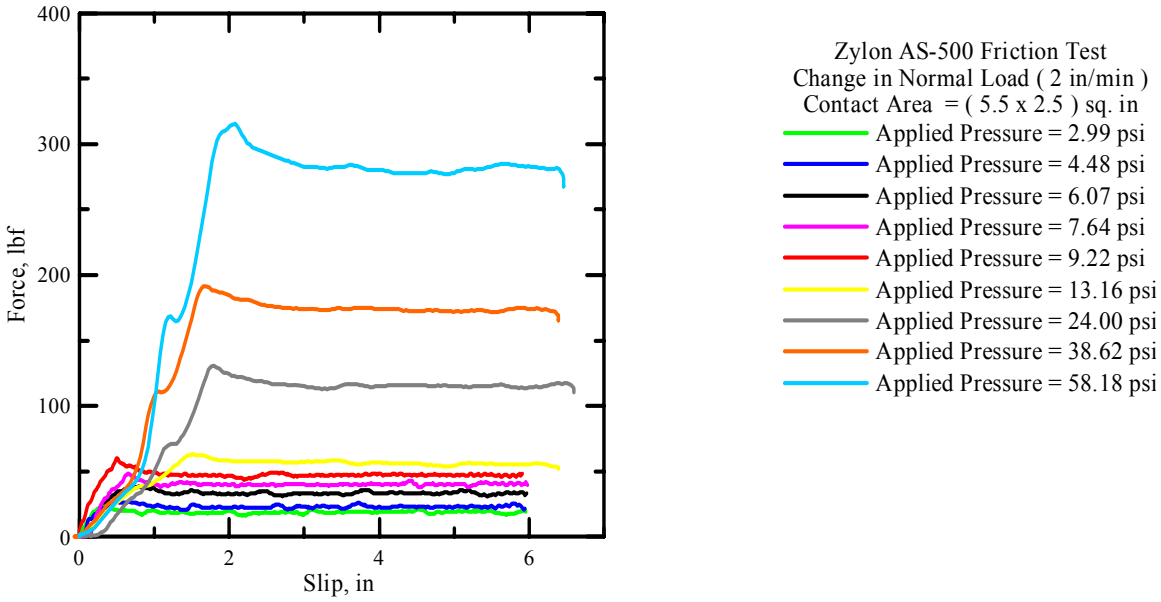

Figure 4.11: Zylon AS-500 Friction Tests for Loading Rate of 2.0 in/min.

The graph 4.12 shows the coefficient of the friction for Zylon AS-500 tested with a loading rate of 2.0 inches per minute. The figure 4.13 shows the results for Zylon AS-500 friction test for a loading rate of 6.0 in/min.

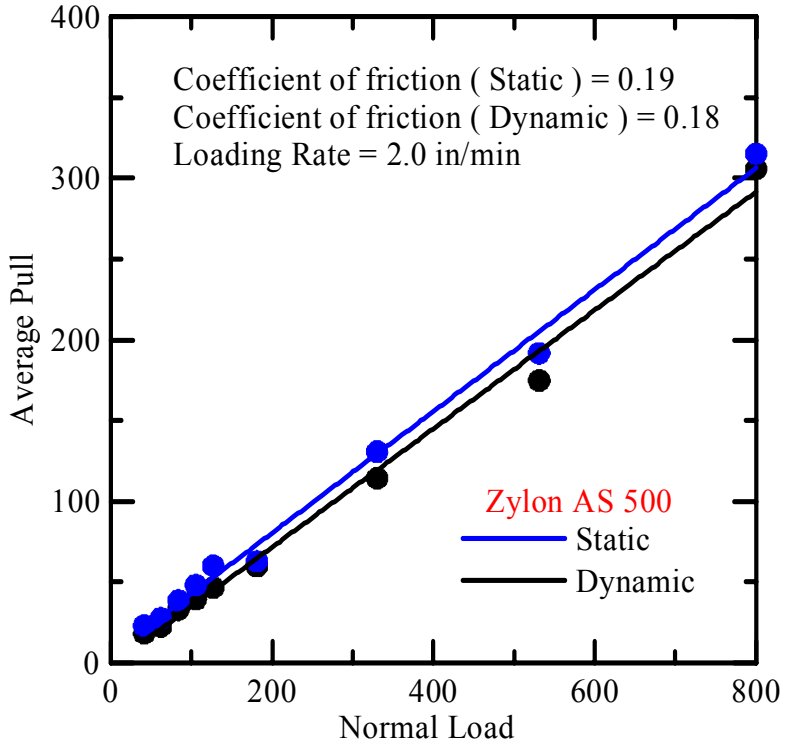

Figure 4.12: Coefficient of friction for Zylon AS-500 for Loading Rate of 2.0 in/min

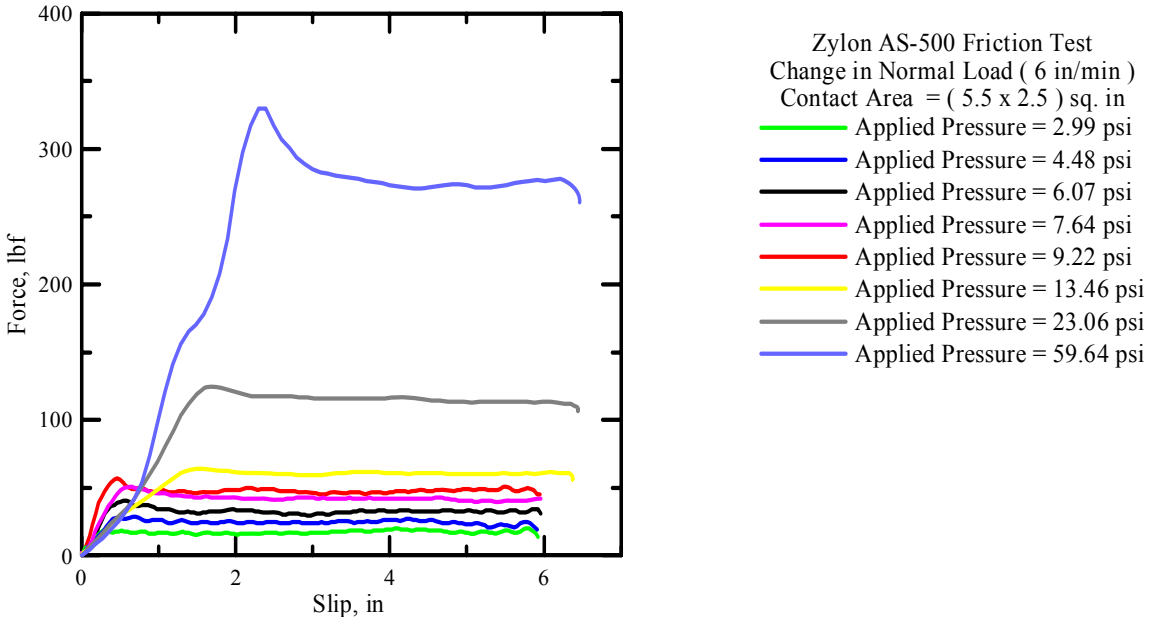

Figure 4.13: Zylon AS-500 Friction Tests for Loading Rate of 6.0 in/min.

The coefficients of friction for a loading rate of 6.0 inches per minute are plotted in figure 4.14.

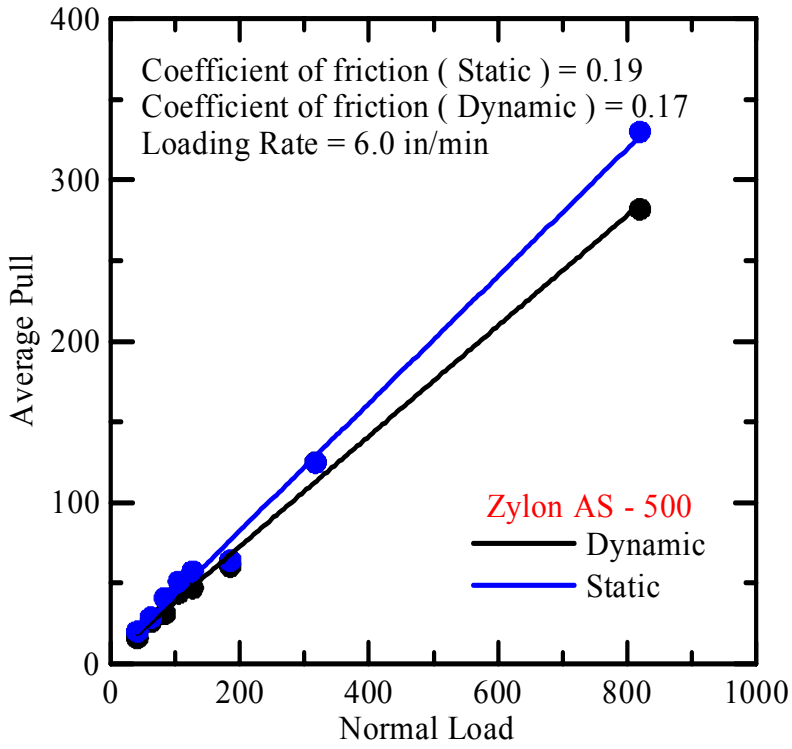

Figure 4.14: Coefficient of Friction for Zylon AS-500 for Loading Rate of 6.0 in/min.

The figure 4.15 and 4.16 show the comparison of the static and dynamic coefficient of friction obtained through the Zylon friction tests for the two different loading rates.

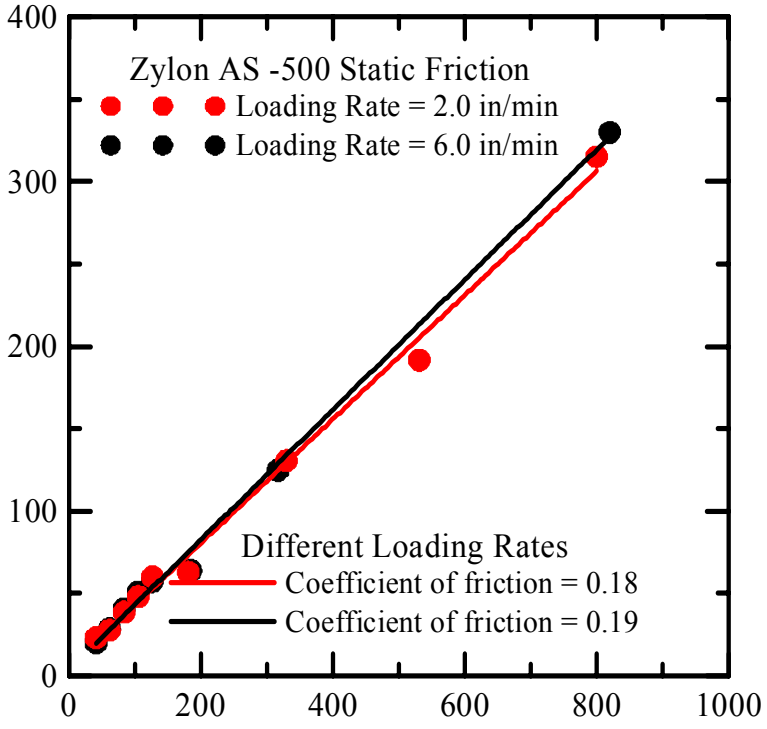

Figure 4.15: Coefficient of Static Friction for Zylon AS-500

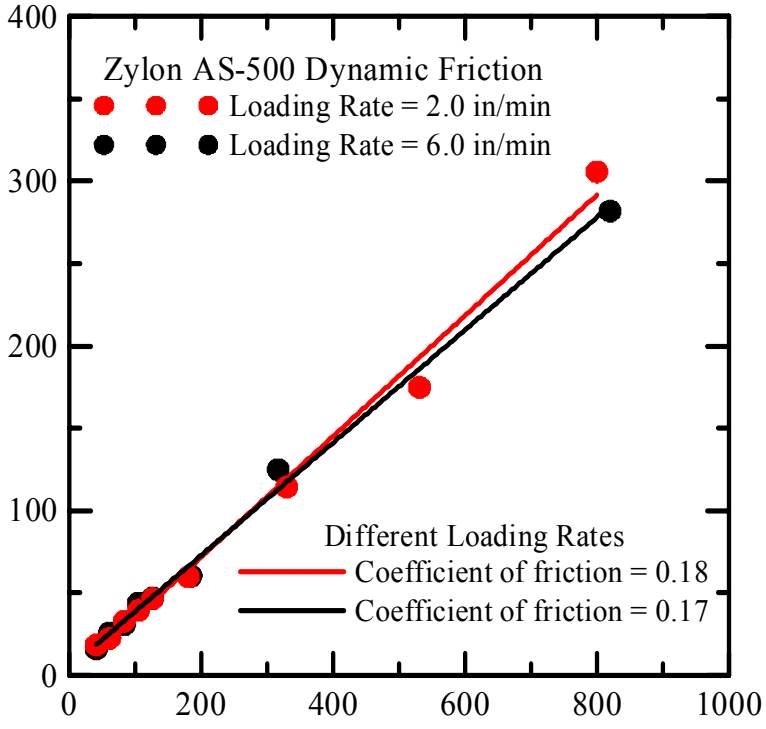

Figure 4.16: Coefficient of Dynamic Friction for Zylon AS-500

The table 4.2 shows the coefficients of static and dynamic friction for the different loading rates for Zylon AS-500.

Table 4.2: Comparison of Friction Coefficients for Zylon AS-500

Loading Rate	Coefficient of Static Friction	Coefficient of Dynamic Friction
2.0	0.188	0.183
6.0	0.194	0.171

4.2.3 Zylon AS-1500 Friction Test Results

The following are the results of the friction tests carried out on Zylon AS-1500. Figure 4.17 shows the force displacement response of five Zylon AS-1500 samples.

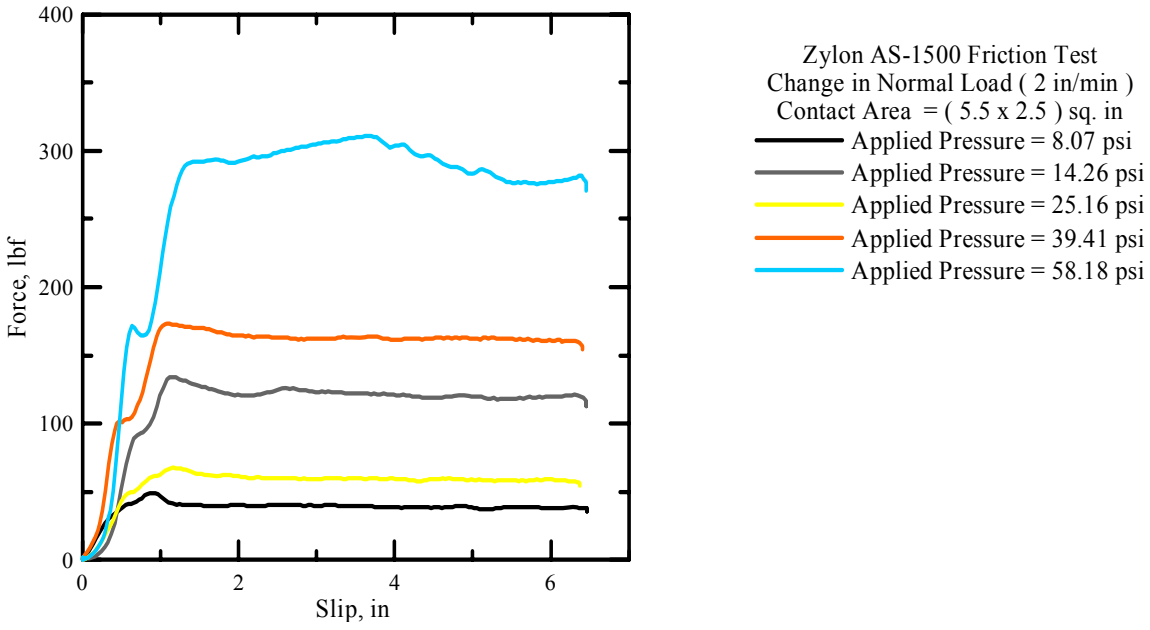

Figure 4.17: Zylon AS-1500 Friction Tests for Loading Rate of 2.0 in/min.

The following graph 4.18 shows the coefficient of the friction for Zylon AS-1500 tested with a loading rate of 2.0 inches per minute.

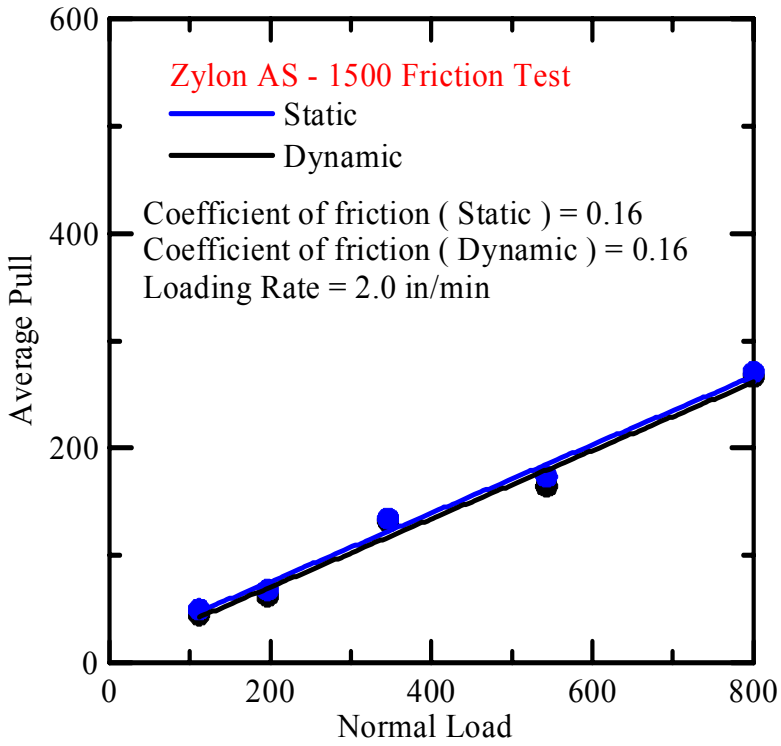

Figure 4.18: Coefficient Of Friction for Zylon AS-1500 for Loading Rate of 2.0 in/min.

The figure 4.19 shows the results for Zylon AS-1500 friction test for a loading rate of 6.0 in/min. The coefficients of friction for a loading rate of 6.0 inches per minute are plotted in figure 4.20. The figures 4.21 and 4.22 show the comparison of the static and dynamic coefficient of friction obtained through the Zylon AS-1500 friction tests for different loading rates.

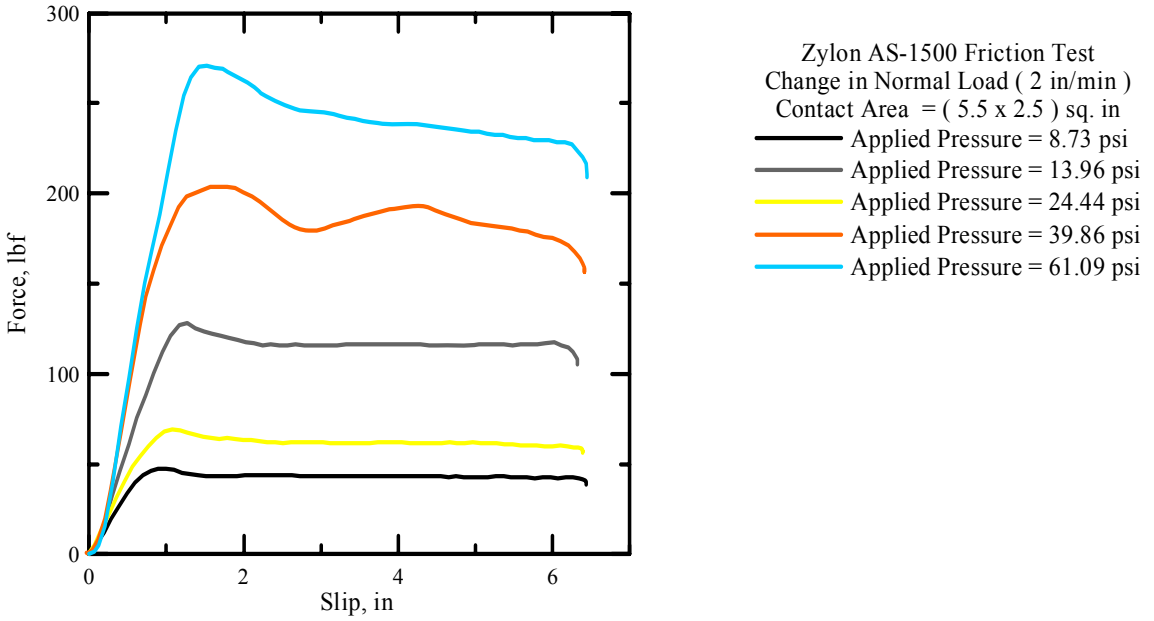

Figure 4.19: Zylon AS-1500 Friction Tests for Loading Rate of 6.0 in/min.

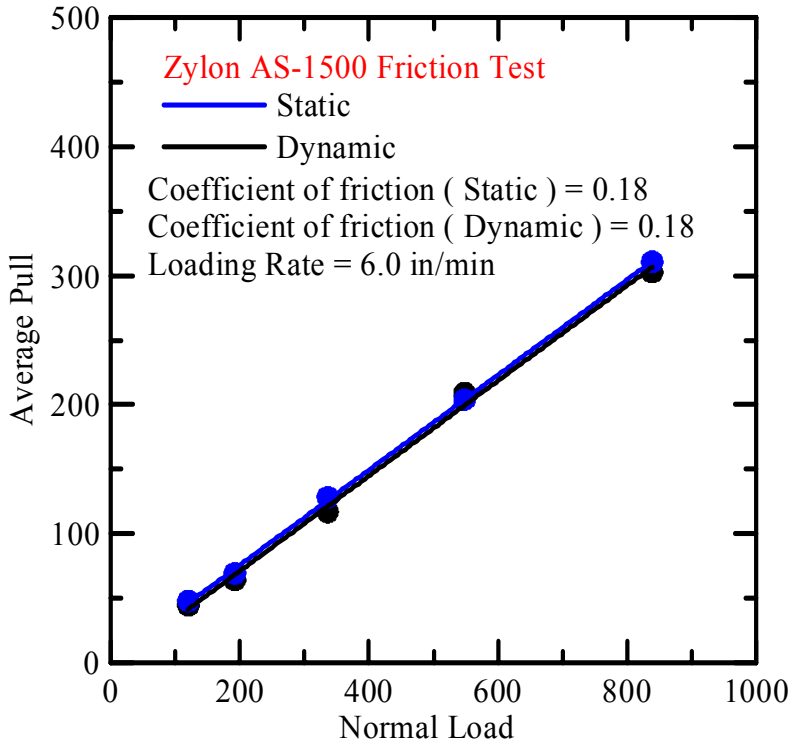

Figure 4.20: Coefficient of Friction for Zylon AS-1500 for Loading Rate of 6.0 in/min.

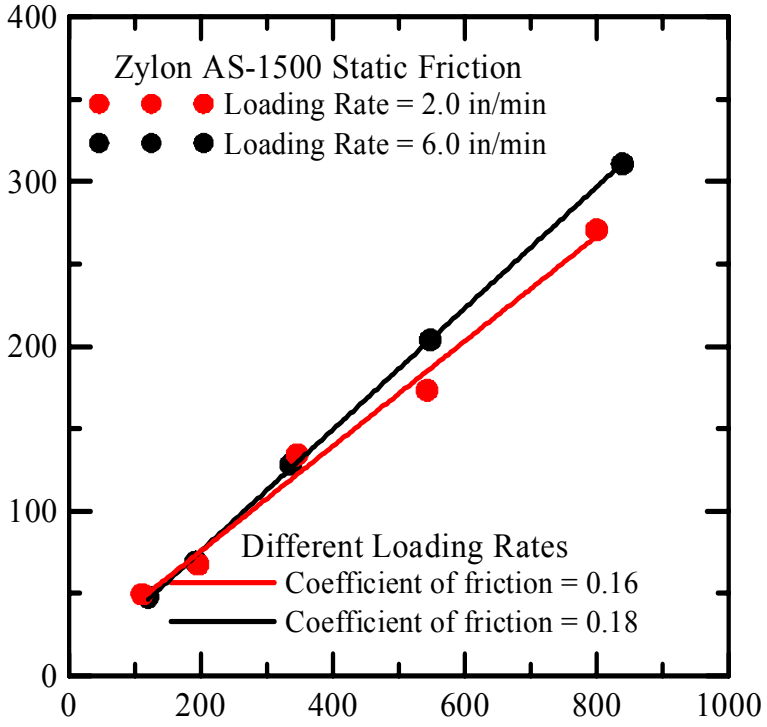

Figure 4.21: Coefficient of Static Friction for Zylon AS-1500.

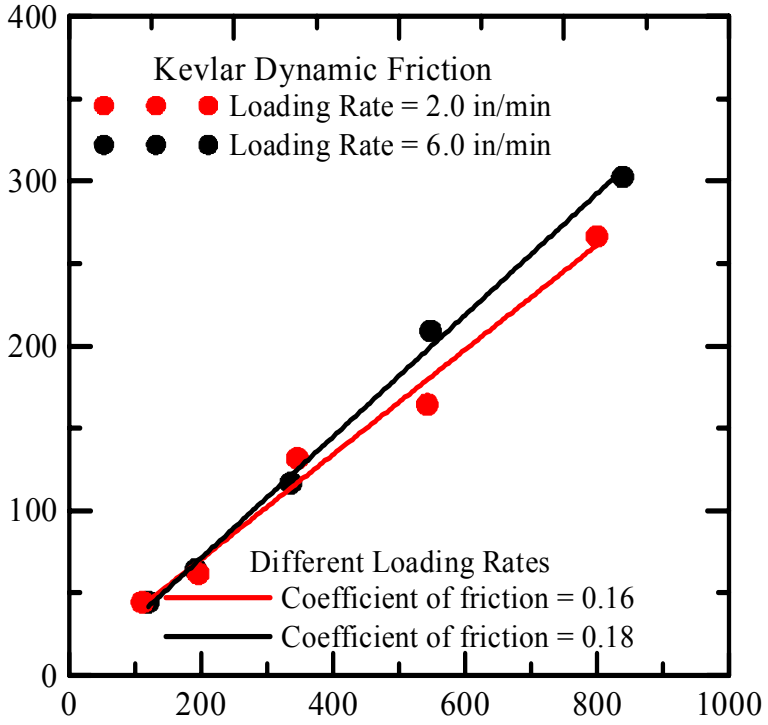

Figure 4.22: Coefficient of Dynamic Friction for Zylon AS-1500.

The table 4.3 shows the coefficients of friction for the different loading rates. The table indicates that the coefficients of friction are constant at a particular loading rate and increase with increase in the loading rate.

Table 4.3: Comparison of Friction Coefficients for Zylon AS-1500

Loading Rate	Coefficient of Static Friction	Coefficient of Dynamic Friction
2.0	0.159	0.159
6.0	0.184	0.184

4.3 Mechanics of Material (MM) approach

The coefficients of friction for Kevlar AS-49 and Zylon AS-500 fabrics were determined through the friction test discussed in the preceding sections. The purpose of this formulation is to develop a mechanics of materials approach which would allow for the prediction of load-deformation response of multi- layer Static Ring Tests conducted as per chapter 2.considering the effects of layer-to-layer friction. The free body diagram of a multi-layer fabric system is used. A general constitutive response is introduced to accommodate for the friction between two fabric layers. This friction is a coulomb type friction measure and its magnitude is dependent on the amount of load transferred between the two layers. In the absence of friction, all the layers would participate equally in carrying the load. In the presence of friction, it is expected that outer layers would be carrying a smaller magnitude of force. Using this information, it is possible to predict the response of multi-layer fabric systems and compare the experimental data with simulated response. Figure 4.23 shows the various forces acting on a one layer fabric test.

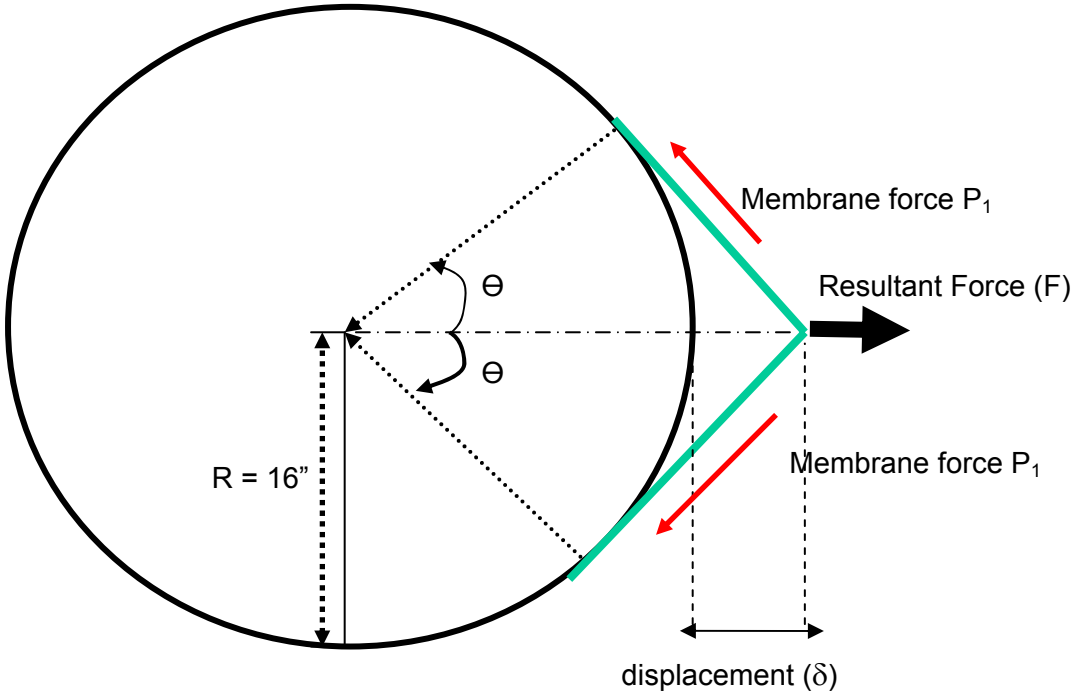

Figure 4.23: Static Ring apparatus with one layer of fabric

The various assumptions made to facilitate the computations of the load deflection responses for the static ring tests.

1) The primary mode of load transfer is friction between the blunt nose-fabric, fabric-fabric, and finally, fabric-steel ring. This results in load transfer from the blunt nose to the fabric layers and back to the ring.
2) The angle θ is same for all layers of the fabric during the test.
3) The angle θ can be related to the displacement of the blunt nose using basic geometrical relationships. It changes as a function of δ during a test.
4) The axial load is transferred from one layer to the other in the form of a concentrated point load.

5) The stress concentrations at the vicinity of the blunt nose and shear deformations are ignored.
6) The friction coefficient between each layer is the same. The friction force is a function of the normal load transmitted between each two layers.

The various notations that were used in this section are as follows.

n Layer number, n starts from the bottom (the first layer that is in contact with the blunt nose at the beginning of the test)

P_n Membrane force in layer n.

k_i Ratio of membrane force in layer $i+1$ to layer i.

F_n Contact force between layer n and $n+1$, e.g. F_2 – Force between layer two and layer three.

α_i Ratio of contact force in layer $i+1$ to layer i

μ Coefficient of friction between any two layers

Analysis of Test Results Based on a No-Friction Condition

Under this assumption that there is no friction between the layers and the response of all the layers can be adjusted by the response of a single layer multiplied by the number of layer, one would obtain a single layer approach. The relationship between the angle θ and the blunt nose displacement δ, as shown in figure 4.23 is

$$\cos\theta = \frac{R}{R+\delta} \tag{1}$$

Using equilibrium of forces in the x-direction, the membrane force in a layer is

$$P_1 = \frac{F}{2\sin\theta} \tag{2}$$

It is furthermore assumed that the entire length of the fabric material is subjected to uniform stretching. The initial length L_0 and final length L are calculated from geometrical considerations. If θ is in radians then

$$L_0 = 2\pi R \tag{3}$$

$$L = 2R\left[\pi - \theta + \tan\theta\right] \tag{4}$$

Therefore, the (engineering) strain can be computed as

$$\varepsilon = \frac{\tan\theta - \theta}{\pi} \tag{5}$$

The relation between the applied forces and the deformation can be normalized in the context of a "derived" stress-strain response. The blunt nose force is converted to the in-plane fabric force and considering the effective thickness of the layer, it is represented as the stress in the layer. The displacement of the blunt nose is converted to the strain in the lamina as well. The net stress-strain response obtained from the Static Ring test is calculated for several multi layer composites.

The graph in figure 4.24 shows the normalized stress-strain plots for 1, 4 and 8 layer Kevlar Static Ring test for the thinner (thickness = 0.235 in, Type B) penetrator. The complete width of the fabric (4") has been considered in determining the cross sectional area, which results in significant underestimation of the strength. A better approach is to use the contact width (1.5") of the blunt nose as the effective width of the specimen. The results from this assumption are shown in figure 1-3. However, the procedure over predicts the value of the maximum stress indicating that additional

material beyond the width of the blunt nose is active in carrying the force. Note that when the data from 4 and 8 layer fabrics are normalized using this procedure, the strain value computed is significantly higher than the tensile strain measurements. This indicates that the stiffness offered by a fabric with n layers is less than the value of n multiplied by the stiffness of a single layer.

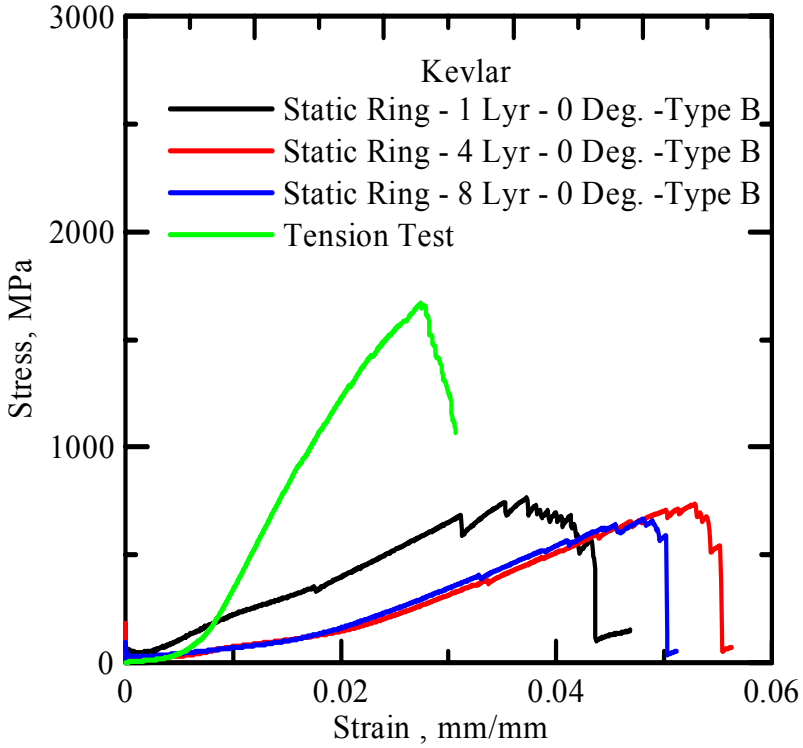

Figure 4.24: Normalized Stress-Strain Plots For Static Ring Tests Compared With the Experimental Tension Test (Effective Width = Fabric Width)

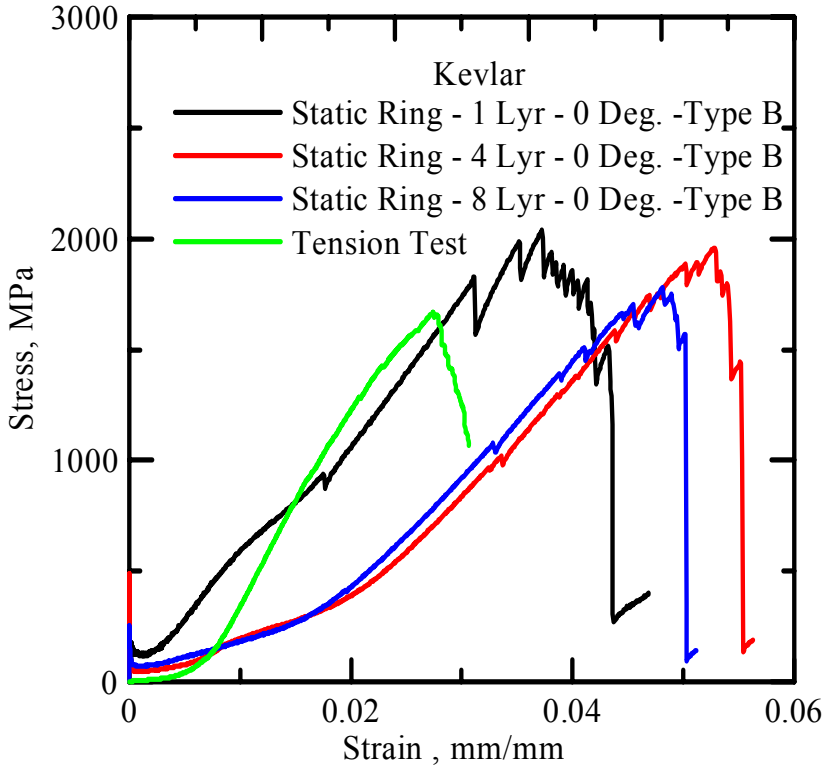

Figure 4.25: Normalized Stress-Strain Plots For Static Ring Tests Compared With the Experimental Tension Test (Effective Width = Width of the Blunt Nose)

Figure 4.25 shows the load-deformation curves for the Zylon AS-500 fabric and different number of layers. It should be noted that the peak deflection for the varying samples is in a narrow range indicating that the stiffness of the samples varies much more with the number of layers but not the overall ductility. A similar result has been obtained for Kevlar AS-49 as shown in figure 4.1.

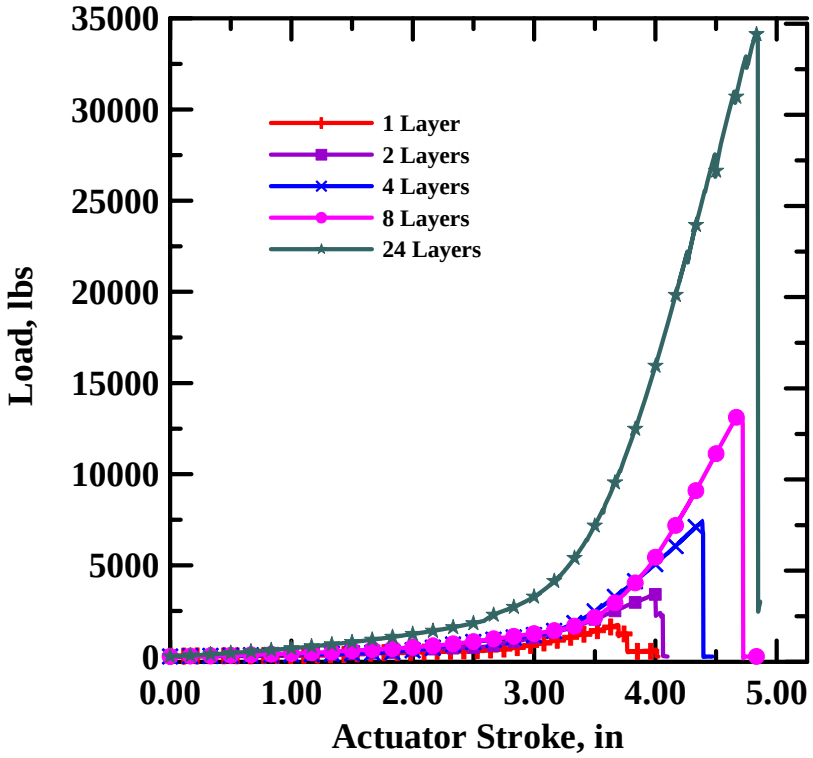

Figure 4.25: Load-deformation response of 1, 2, 4, 8 and 24 layer Zylon AS-500 samples

Two-Layer Static Ring Tests

Figure 4.26 shows the free body diagram for two layers of fabric. Assuming that the two layers act independent of one another, the two membrane forces are different. All the other assumptions stated previously are in effect. It is furthermore assumed that the mode of load transfer between the two layers is by means of the frictional force between the two layers. This friction force reduces the magnitude of the force that is transferred from one layer of fabric to the next directly at the vicinity of the blunt nose.

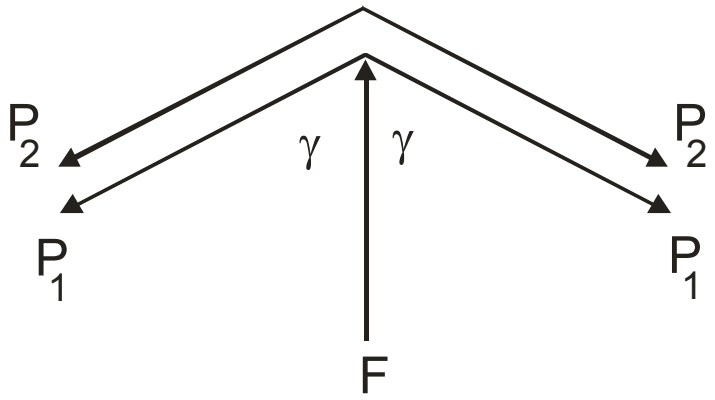

Figure 4.26: FBD for two-layer fabric system (External Equilibrium)

Considering equilibrium in the y–direction (Figure 2-1) and noting that $\gamma = 90 - \theta$, we have

$$F = 2\sin\theta\left(P_1 + P_2\right) \tag{6}$$

Figures 4.27 through 4.28 show the free body diagram for the internal equilibrium, the various forces in layer two and layer one, respectively.

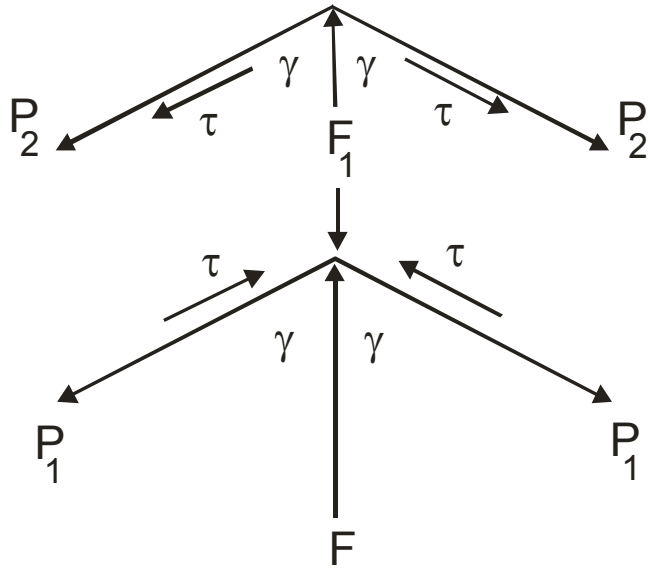

Figure 4.27: FBD for two-layer fabric system (Internal Equilibrium)

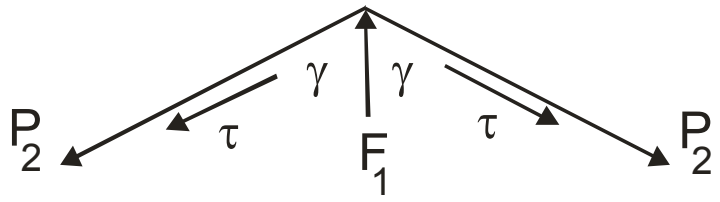

Figure 4.28: FBD for two-layer fabric system (Second Layer)

Considering the second layer of fabric and defining the friction as

$$\tau = \mu F_1 \tag{7}$$

The equilibrium in the y-direction can be written as

$$F_1 = 2P_2 \sin\theta + 2\mu F_1 \sin\theta \tag{8}$$

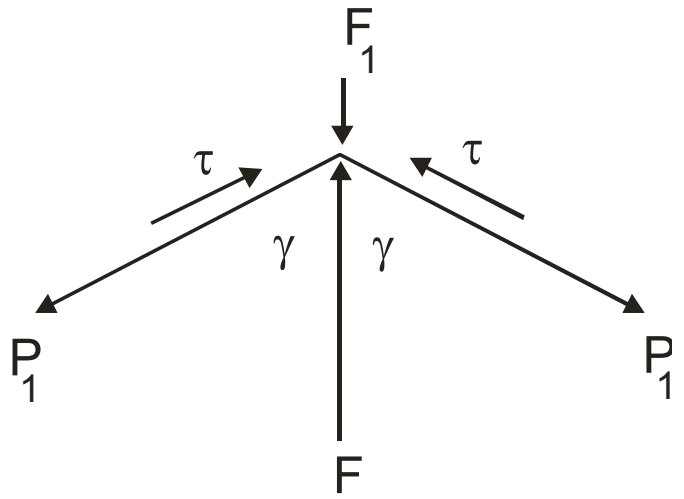

Figure 4.29: FBD for two-layer fabric system (First Layer)

Similarly, considering the equilibrium in the y-direction for the first layer of fabric

$$F - F_1 = 2P_1 \sin\theta - 2\mu F_1 \sin\theta \tag{9}$$

If we denote the fraction of the load transferred at the contact point as a variable α such that

$$F_1 = \alpha_1 F$$

(10)

The forces in the two layers can be represented as

$$P_1 = \frac{F\left(1-\alpha_1+2\mu\sin\theta\right)}{2\sin\theta} \tag{11}$$

$$P_2 = \frac{\alpha_1 F\left(1-2\mu\sin\theta\right)}{2\sin\theta} \tag{12}$$

Note that by designating $\alpha_1 = 0.5$, one would have the same membrane force in each layer (equal load sharing rule). We can now compute the ratio of the two membrane forces as

$$k_1 = \frac{\alpha_1\left(2\mu\sin\theta-1\right)}{1-\alpha_1+2\mu\alpha_1\sin\theta} \tag{13}$$

For various values of coefficient of friction, μ and α_1, and the results obtained from the one-layer Static Ring Test and the Tension Tests, we can now calculate the (simulated) response for the 2-layer Static Ring Test as follows.

(1) Assume a value for the coefficient of friction, μ.

(2) Assume a value for α_1.

(3) Loop through the load increments for the one-layer Static Ring test starting with $F = 0$.

(4) For the current load value, F (from the 1-layer test result) determine its corresponding δ. Compute θ using Equation (1).

(5) Calculate P_1 using Equation (2).

(6) Compute k_1 using Equation (13).

(7) Now compute the actual net force, F in the 2-layer system using Equation (6) with $P_2 = k_1 P_1$.

(8) End load increment loop.

(9) Plot the load (from Step 7) versus the deflection (from Step 4).

This procedure is repeated for a number of combinations of μ $(0 \le \mu \le 0.3)$ and $\alpha_1 \left(0.4 \le \alpha_1 \le 0.8\right)$, the best fit (matching the max. stiffness of the simulated curve with the test result) is selected. The figures 4.30 and 4.31 show two typical results from this analysis.

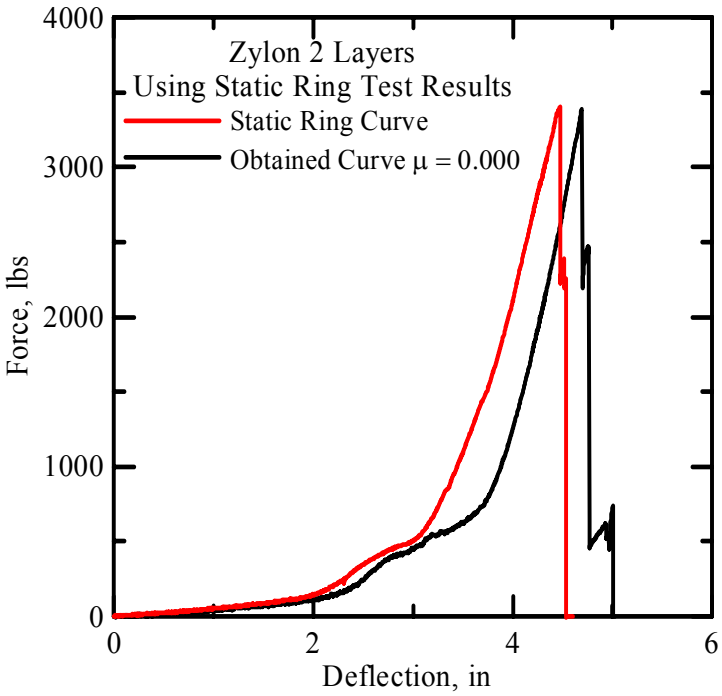

Figure 4.30: Zylon AS-500 2-Layer Static Ring Test simulation with $\mu = 0.0$ and $\alpha_1 = 0.49$

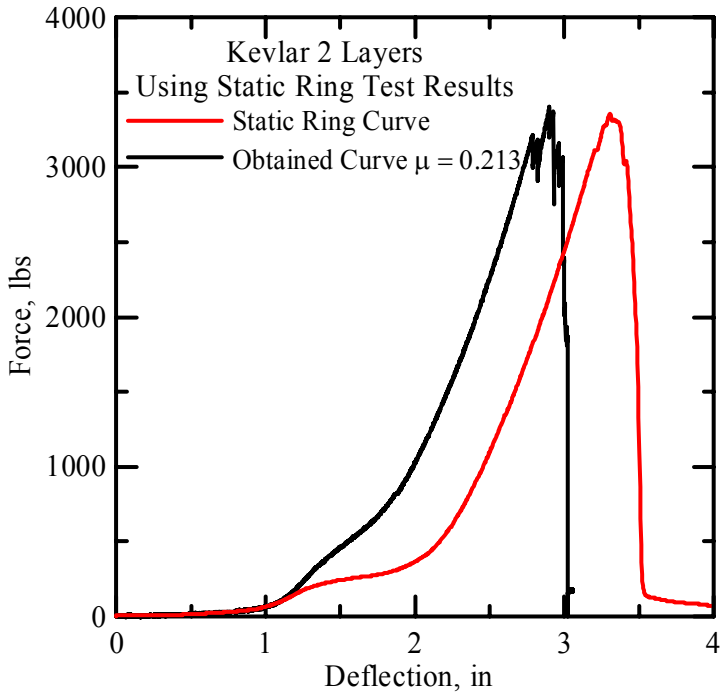

Figure 4.31: Kevlar 2-Layer Static Ring Test simulation with $\mu = 0.213$ and $\alpha_1 = 0.610$

When the tension test results (Chapter 2) are used in Step 5 (instead of Static Ring Test results – Chapter 3), the simulated curves predict the peak load relatively well but not the stiffness. Two samples results are shown in figures 4.32 and 4.33.

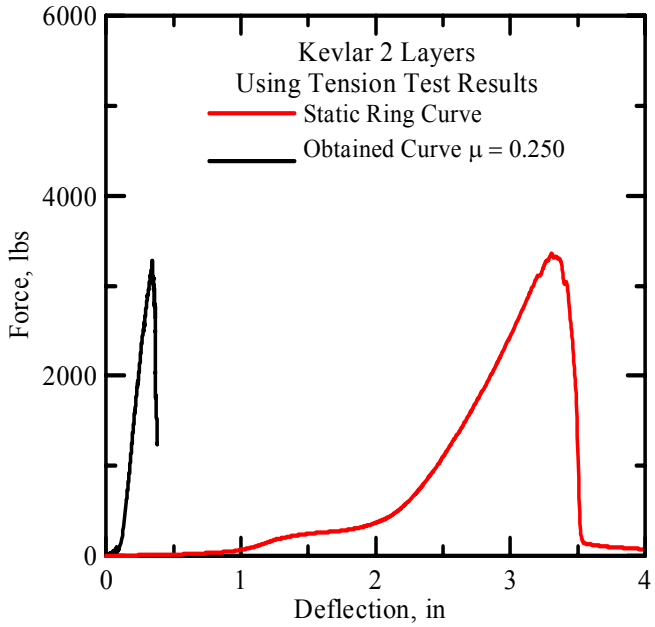

Figure 4.32: Kevlar AS-49 2-Layer Static Ring Test simulation with $\mu = 0.25$ and $\alpha_1 = 0.45$ using Tension Test results

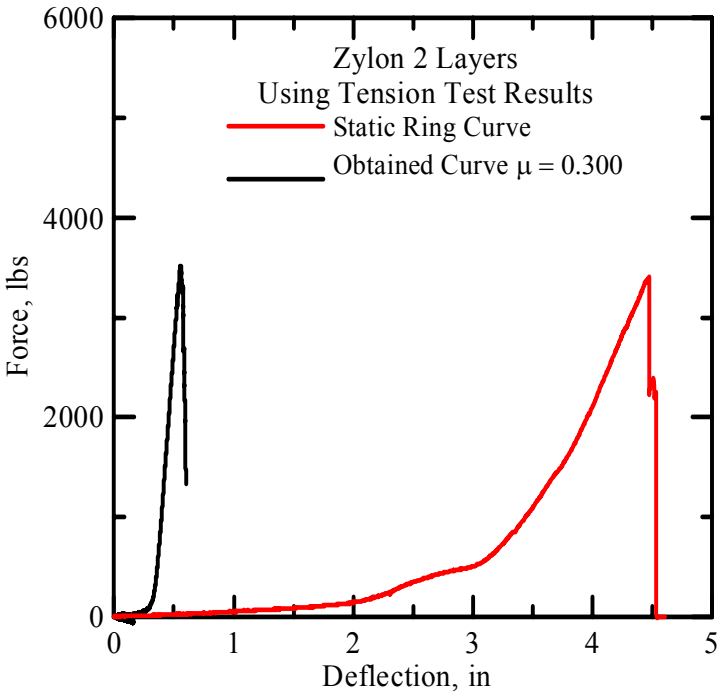

Figure 4.33: Zylon AS-500 2-Layer Static Ring Test simulation with $\mu = 0.3$ and $\alpha_1 = 0.34$ using Tension Test results

The "best fit" graphs are shown in table 4.4 and table 4.5 for Kevlar AS-49 and Zylon AS-500 respectively using the max. k_1 values.

Table 4.4: Best Fit Results for Kevlar AS-49

Coefficient of Friction	Using Static Ring Results		Using Tension Test Results	
μ	α_1	k_1	α_1	k_1
0.000	0.460	0.852	0.300	0.465
0.213	0.610	0.853	0.420	0.461
0.250	0.660	0.854	0.450	0.465
0.300	0.720	0.855	0.500	0.464

Table 4.5: Best Fit Results for Zylon AS-500

Coefficient of Friction	Using Static Ring Results		Using Tension Test Results	
μ	α_1	k_1	α_1	k_1
0.000	0.490	0.961	0.190	0.265
0.171	0.630	0.985	0.230	0.271
0.200	0.660	0.984	0.250	0.269
0.300	0.790	0.982	0.340	0.273

Tables 4.4 and 4.5 indicate that for a fairly constant value of the ratio k_1 with increase in the coefficient of friction, the contact force transferred from layer one to layer two for the both fabrics increases. A larger contact force is transferred if the results from the Static Ring Tests are considered as compared to the uniaxial Tension Tests.

Four-Layer Static Ring Tests

The derivation is similar to the two-layer case. Figure 4.34 shows the free body diagram for four layers of fabric.

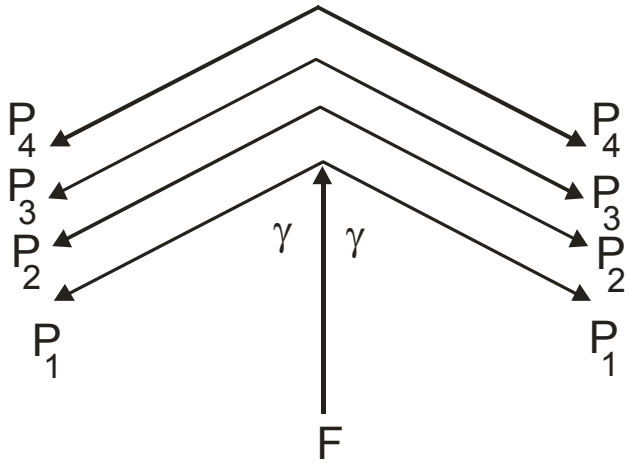

Figure 4.34: FBD for four-layer fabric system (External Equilibrium)

Considering only external forces

$$F = 2\sin\theta\left(P_1 + P_2 + P_3 + P_4\right) \tag{14}$$

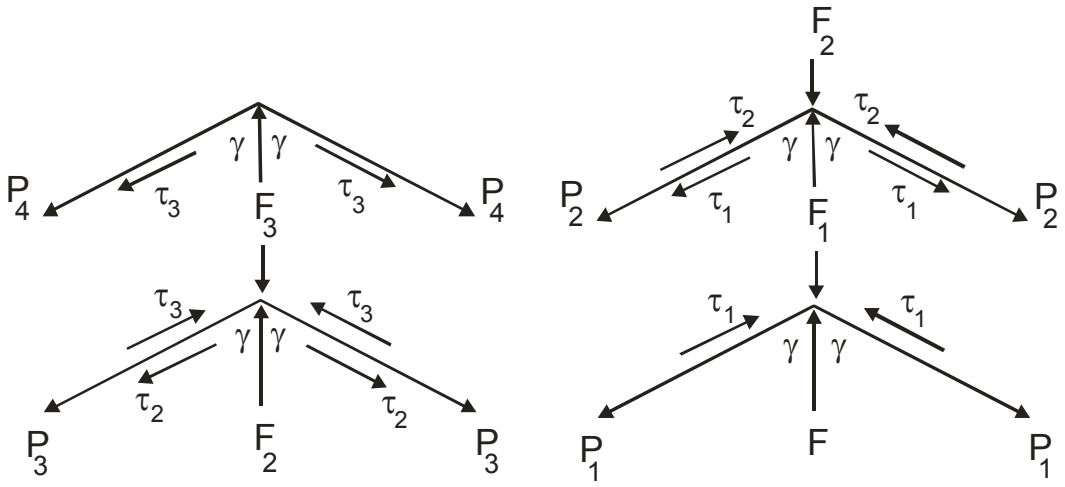

Figure 4.35: FBD for four-layer fabric system (Internal Equilibrium)

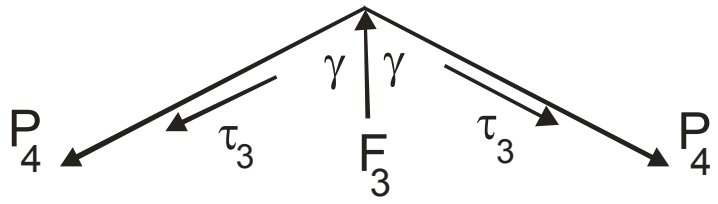

Figure 4.36: FBD of fourth layer of four-layer fabric system

Considering the equilibrium of the fourth layer of fabric, we have

$$F_3 = 2\sin\theta\left(\mu F_3 + P_4\right) \tag{15}$$

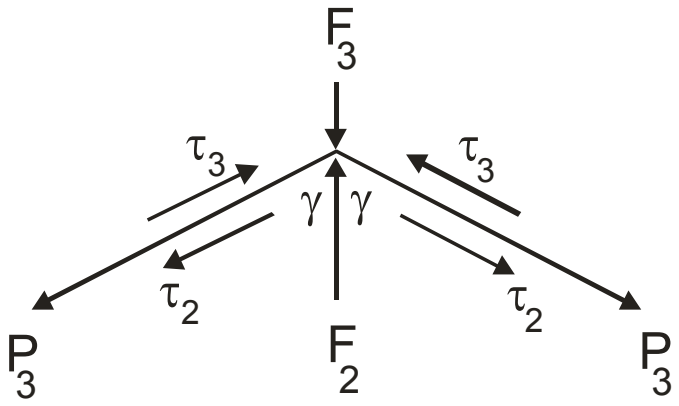

Figure 4.37: FBD of third layer of four-layer fabric system

Similarly, considering the equilibrium of the third layer of fabric, we have

$$F_2 - F_3 = 2\sin\theta\left(P_3 - \mu F_3 + \mu F_2\right) \tag{16}$$

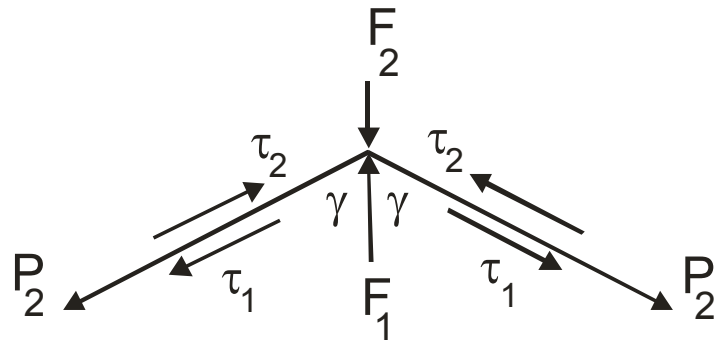

Figure 4.38: FBD of second layer of four-layer fabric system

Considering the equilibrium of the second layer of fabric, we have

$$F_1 - F_2 = 2\sin\theta\left(P_2 - \mu F_2 + \mu F_1\right) \tag{17}$$

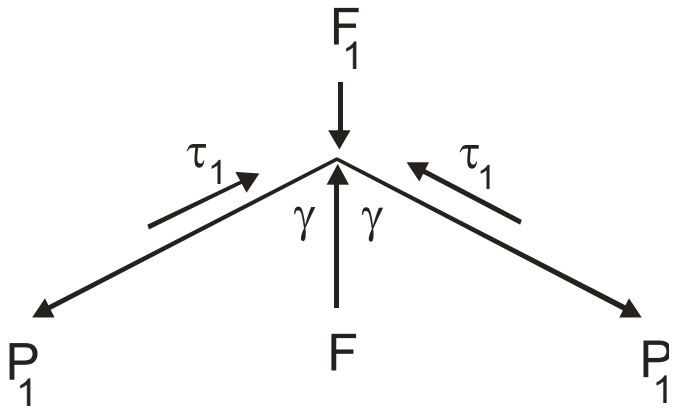

Figure 4.39: FBD of first layer of four-layer fabric system

Finally for the first layer of fabric

$$F - F_1 = 2\sin\theta\left(P_1 - \mu F_1\right) \tag{18}$$

Solving the above equations, we have the following conditions.

$$P_1 = \frac{F - F_1 + 2\mu F_1 \sin\theta}{2\sin\theta} \tag{19}$$

$$P_2 = \frac{F_1 - F_2 + 2\mu\sin\theta\left(F_2 - F_1\right)}{2\sin\theta} \tag{20}$$

$$P_3 = \frac{F_2 - F_3 + 2\mu\sin\theta\left(F_3 - F_2\right)}{2\sin\theta} \tag{21}$$

$$P_4 = \frac{F_3\left(2\mu\sin\theta - 1\right)}{2\sin\theta} \tag{22}$$

If the relation between the contact forces is assumed as follows

$$F_1 = \alpha_1 F \tag{23}$$

$$F_2 = \alpha_2 F_1 \tag{24}$$

$$F_3 = \alpha_3 F_2 \tag{25}$$

The membrane forces for each layer can be calculated as shown below.

$$P_1 = \frac{F\left(1-\alpha_1+2\alpha_1\mu\sin\theta\right)}{2\sin\theta} \tag{26}$$

$$P_2 = \frac{F\alpha_1\left(1-\alpha_2+2\alpha_2\mu\sin\theta-2\mu\sin\theta\right)}{2\sin\theta} \tag{27}$$

$$P_3 = \frac{F\alpha_1\alpha_2\left(1-\alpha_3+2\alpha_3\mu\sin\theta-2\mu\sin\theta\right)}{2\sin\theta} \tag{28}$$

$$P_4 = \frac{F\alpha_1\alpha_2\alpha_3\left(1-2\mu\sin\theta\right)}{2\sin\theta} \tag{29}$$

We can now represent the ratios of the membrane forces as we did with the two-layer case.

$$k_1 = \frac{\alpha_1\left(1-\alpha_2+2\mu\alpha_2\sin\theta-2\mu\sin\theta\right)}{1-\alpha_1+2\mu\alpha_1\sin\theta} \tag{30}$$

$$k_2 = \frac{\alpha_2\left(\alpha_3-1\right)}{1-\alpha_2} \tag{31}$$

$$k_3 = \frac{\alpha_3}{\alpha_3-1} \tag{32}$$

For various values of coefficient of friction, μ and the set $\left(\alpha_1,\alpha_2,\alpha_3\right)$, and the results obtained from the one-layer Static Ring Test, we can now calculate the (simulated) response for the 4-layer Static Ring test as follows.

(1) Assume a value for the coefficient of friction, μ.

(2) Assume values for the components of the set $\left(\alpha_1,\alpha_2,\alpha_3\right)$.

(3) Loop through the load increments for the one-layer Static Ring test starting with $F = 0$.

(4) For the current load value, F (from the 1-layer test result) determine its corresponding δ. Compute θ using Equation (1).

(5) Compute $P_i, i = 2,3,4$ using Equation (27-29).

(6) Compute k_i using Equation (30-32).

(7) Now compute the actual net force, F in the 4-layer system using Equation (14).

(8) End load increment loop.

(9) Plot the load (from Step 7) versus the deflection (from Step 4).

This procedure is repeated for a number of combinations of μ $(0 \le \mu \le 0.3)$ and α_i, the best fit (matching the max. stiffness of the simulated curve with the test result) is selected. Note that the physical constraint on each of these constants is that they cannot exceed the value one. Also, the constant α_3 cannot have value greater than 0.5.

Table 4.6: Best Fit Results for Zylon AS-500

Coefficient of Friction	Fitted Values					
	α	α_1	α_2	k_1	k_2	k_3
μ = 0.000	0.500	0.600	0.400	0.400	0.900	0.667
Another good fit	0.480	0.600	0.400	0.369	0.900	0.667
μ = 0.171	0.600	0.500	0.500	0.456	0.500	1.000
Another good fit	0.600	0.500	0.400	0.456	0.600	0.667
μ = 0.270	0.700	0.500	0.500	0.447	0.500	1.000
Another good fit	0.700	0.600	0.500	0.358	0.750	1.000

The figures 4.40 and 4.41 show the graphs for Zylon AS-500 and Kevlar AS-49 for the four-layer analysis with the “best fit” values.

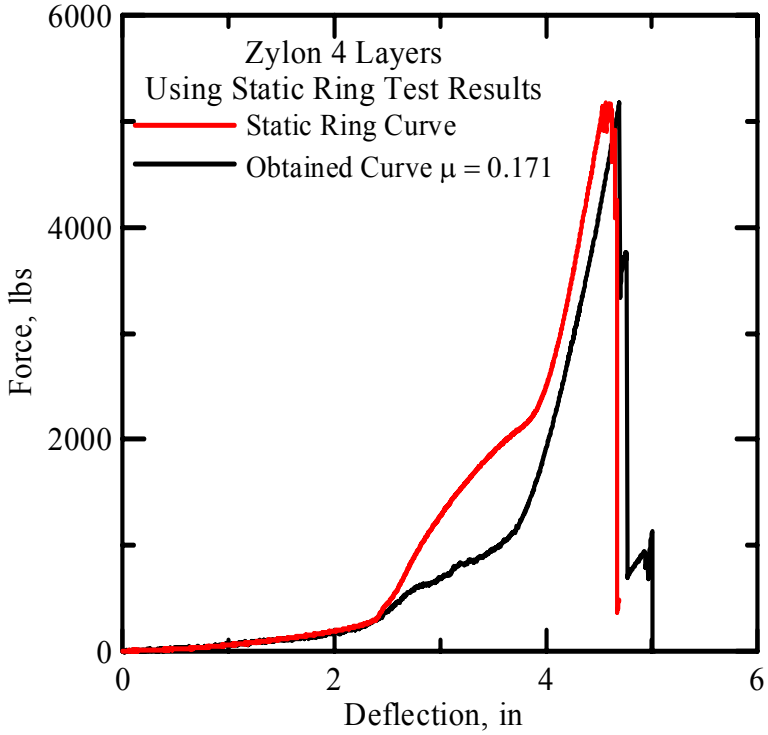

Figure 4.40: Zylon 4-Layer Static Ring Test simulation with $\mu = 0.171$

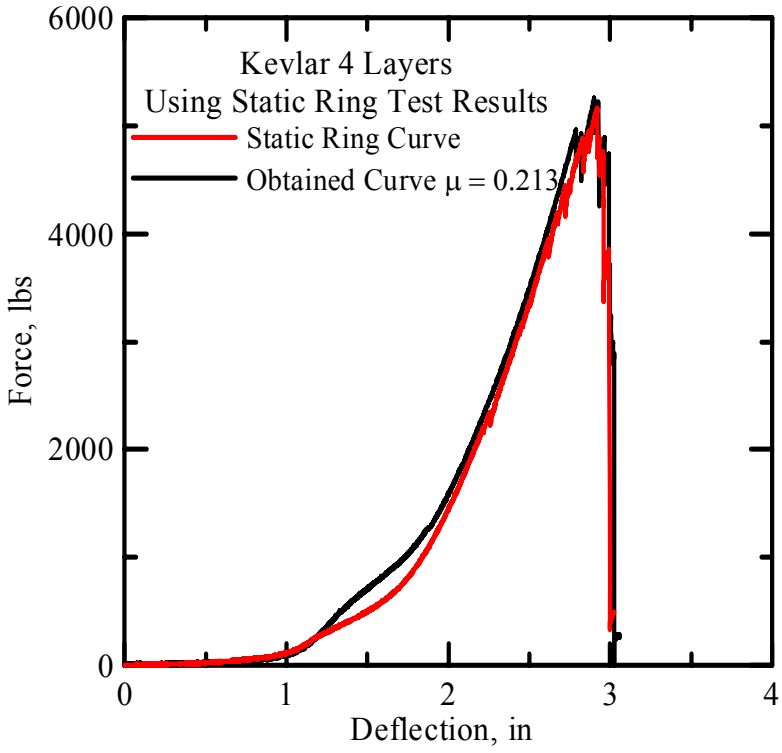

Figure 4.41: Kevlar 4-Layer Static Ring Test simulation with $\mu = 0.213$

A similar approach can be followed to determine the various coefficients in an eight layer static ring setup. It is seen that by using the mechanics of materials approach and incorporating the experimental friction values, it is possible to predict the load deflection response using the one layer static ring test results. This procedure can be optimized to predict optimum values of these defined coefficients and get a clearer perspective of the importance of the coefficient of friction in the static ring tests.

Chapter 5: Shear Tests

5.1 Introduction to Shear Tests

One of the important material properties required for the finite element models of Kevlar AS-49 and Zylon AS-500 for the static ring tests was the response of these fabrics to shear deformations. It was also observed that the 45 and 90 degree penetrator orientation, the photographs taken during the interval of a static ring test suggested the involvement of shear deformations. Thus, the determination of the shear properties of the fabrics was necessitated.

5.1.1 Objectives

The primary objective of shear tests is to determine the response of the three fabrics to shear deformations. These tested were conducting by running uniaxial tension tests on various kinds of specimens (different dimensions) and using modifications to the simple tension tests grips.

5.1.2 Specimen Preparation Procedure

Tests were run using three different kinds of specimens for three different kinds of tests. The three different test methods adopted were the off-axis tension tests, “cut” sample tests and the picture frame tests. For the off-axis, standard static ring specimens of 4”” width and varying lengths were used. Standard tension tests specimens of 2.5” width

and varying lengths were utilized for the "cut" sample tests. For the picture frame tests, specimens of 10" by 10" size were tested.

5.1.3 Test Procedure

All the different tests were conducted in a 22 Kips servo-hydraulic test frame operated under closed-loop control.

The test procedure was a displacement control test with the rate of displacement of actuator (stroke) set at 0.1"/min. Digital data acquisition was used to collect data at every 0.5 second. The test was continued until complete failure of the specimen was achieved. The load-deformation results were used to calculate the stress-strain response. The overall deformation of the specimen was measured by the stroke movement of the actuator.

5.2 Off-Axis Tension Tests

The off-axis tests were done only with Kevlar AS-49 and Zylon AS-500 fabrics. These tests were conducted with the principal directions of fabrics at 5, 10 and 15 degrees to the vertical.

5.2.1 Off-Axis Tests Specimens

The 4" width static ring samples were cut inclined at 85, 80 and 75 degrees to the horizontal and used for off-axis tests. An example of a sample cut at 80 degrees is illustrated in figure 5.1.These tests were continued until complete failure of the specimen

was achieved. The load-deformation results were used to calculate the stress-strain response.

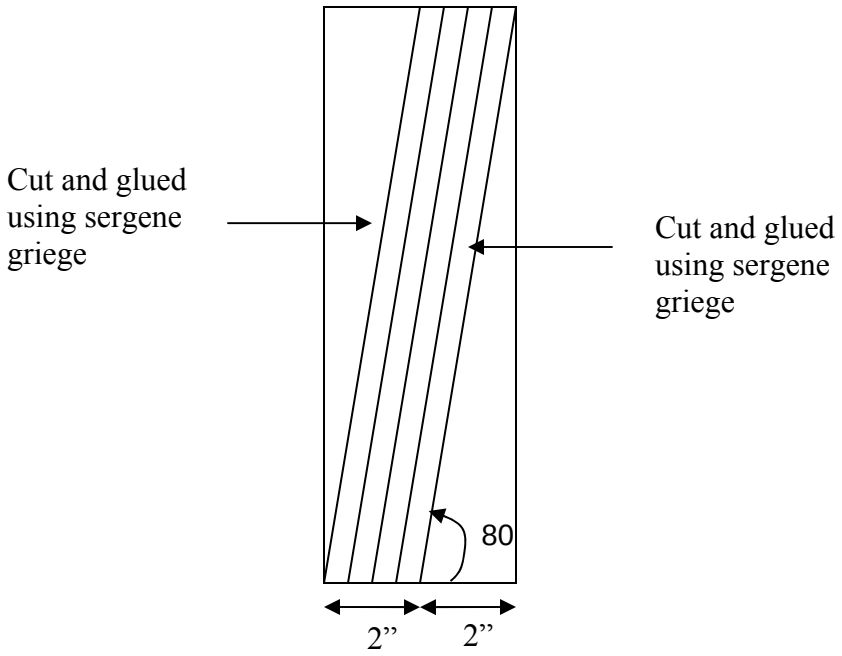

Figure 5.1: Off-Axis Test Specimen

5.2.2 Shear Modulus Determination

The shear modulus can be related to the axial modulus of elasticity, axial Poisson’s ratio and lateral modulus of elasticity by determining the modulus of elasticity in the particular loading direction. An expression relating all these constants was suggested by Jones (1975). The off-axis tension test stress strain response can be used to determine the “inclined” modulus of elasticity. Using the stress strain response from

these tests, the shear modulus G_{12} of Kevlar was calculated using the following orthotropic transformation equation

$$\frac{1}{G_{12}} = \frac{1}{\sin^2\theta * \cos^2\theta}\left(\frac{1}{E} - \frac{\cos^4\theta}{E_1} - \frac{\sin^4\theta}{E_2} + \frac{2\nu_{12}}{E_1}\sin^2\theta * \cos^2\theta\right) \qquad (1)$$

The following are the various notations used in equation (1).

G_{12} – Shear Modulus

E_1 – Stiffness in the Axial Direction

E_2 – Stiffness in the Lateral Direction

ν_{12} – Poisson's Ratio in the Axial Direction

E – Stiffness in the Load Direction

θ – Angle made by the load direction to the principal direction

All the known constants used in the above equation were taken from tables 2.17 to 2.19. A typical stress strain response of an off-axis test sample and a regular tension test is compared in figure 5.2. The off-axis sample is orientated at 80 degrees to the horizontal.

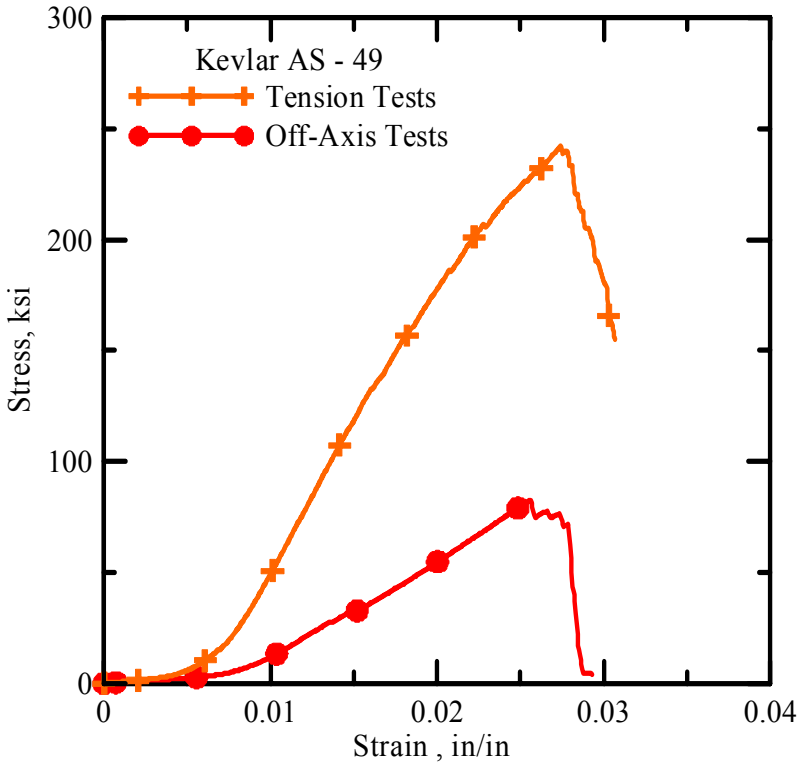

Figure 5.2: Comparison of Regular Tension Tests to Off Axis Tension Tests

5.2.3 Off-Axis Tests Results

Kevlar AS-49

The figure 5.3 and the table 5.1 shows the results of various off-axis tension tests run on Kevlar AS-49. All tested Kevlar and Zylon AS-500 samples had a band type of formation occurring in the middle of the sample as shown figure 5.4. The yarns in this band seemed to be interlocked very closely as compared to the original fabric. It was also observed that the slope of the stress strain curve obtained decreased with increase in the angle of orientation of the principal yarns to the vertical.

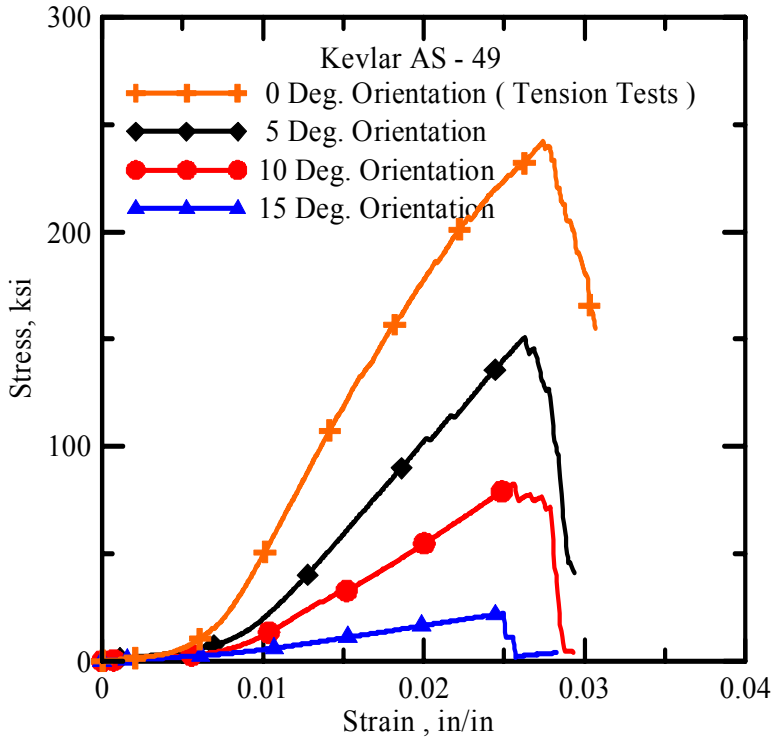

Figure 5.3: Kevlar AS-49 Off-Axis Tension Tests

Table 5.1: Kevlar AS-49 Off-Axis Tension Tests Results.

E_{11} Results for ν_{12}				G_{12} ,ksi		
Stress Range	Average Poisson's Ratio	E_{11},ksi	E_{22},ksi	5 Degrees Off-Axis	10 Degrees Off-Axis	15 Degrees Off-Axis
29-87 ksi	1.844	13468	15284	174	210	76
87-145 ksi	0.705	13468	15284	178	218	77
145-203 ksi	0.618	13468	15284	178	218	77

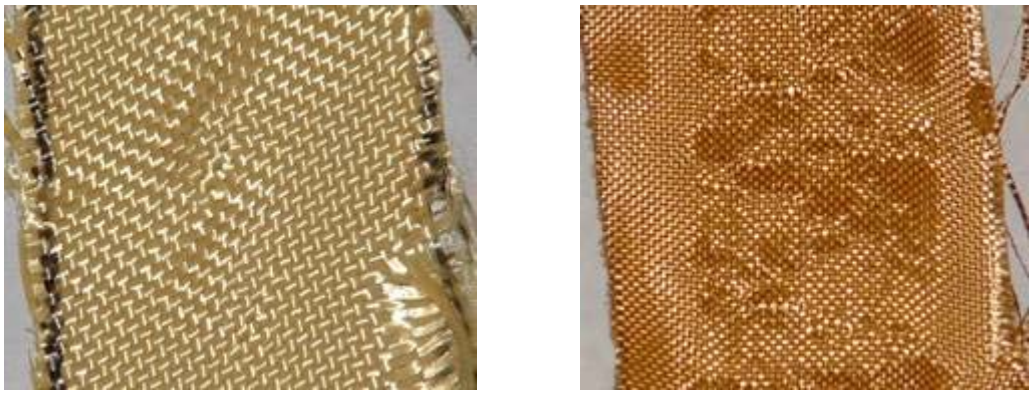

Figure 5.4: Band Type Formation

Zylon AS-500

The figure 5.5 shows the results of the off-axis tension tests for Zylon AS-500 for the three orientations of the principal axis of the fabric

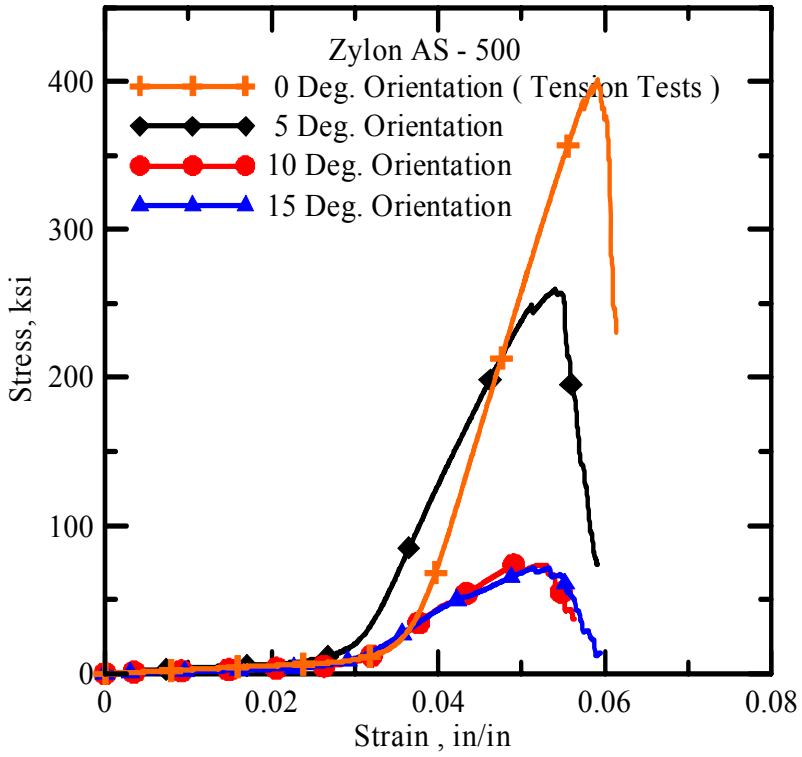

Figure 5.4: Zylon AS-500 Off-Axis Tension Tests

There is variation in the results obtained for Zylon AS-500 in the stress-strain graphs. For higher orientations (10 and 15 degrees), the stress strain graphs seem to converge and have the same peak load. The results obtained from these tests are tabulated in table 5.2

Table 5.2: Zylon AS-500 Off-Axis Tension Tests Results.

E_{11} Results for ν_{12}				G_{12} ,ksi		
Stress Range	Average Poisson's Ratio	E_{11},ksi	E_{22},ksi	5 Degrees Off-Axis	10 Degrees Off-Axis	15 Degrees Off-Axis
73-174 ksi	0.676	19310	19362	212	128	212
174-290 ksi	0.152	19310	19362	215	129	214
290-363 ksi	0.052	19310	19362	215	129	215

A band formation similar to Kevlar AS-49 was also observed in Zylon AS-500.

5.2.4 Off-Axis Tests Conclusions

The off-axis tests result report different values for the shear modulus G_{12} under different orientations of the principal axis to the horizontal. Also, all the yarns are not simultaneously held on either side of the tension grips. Hence, the value of the Young's Modulus obtained in the loaded direction (orientation) is not representative of its value in the same direction. Hence, the results obtained from the off-axis tension tests are unable to accurately predict the shear deformations of the fabrics under the various loads.

5.3 “Cut” Sample Tests

The “Cut” sample tests were done by cutting standard tension test samples along the width at certain defined positions. These tests required the development of an imaging program that could compute the displacements of various selected points on the sample as the test progressed. The displacement data obtained by the image analysis program was then used to compare to the displacement fields obtained for a similar finite element model using different shear modulus values.

5.3.1 “Cut” Tests Specimens

Standard tension test specimens of 2.5” width and 12.5” length were reduced to 1.75” width using a standard fabric cutter. The boundaries of the new developed sample were then glued using sergene griege. A grid of 1.5” width and 6” length (in general) was marked using a fine point black marker. The grid was drawn such that it lay midway, along the length of the sample. The size of the inner grid cells drawn was of 0.75” by 0.75”. It was observed that during the course of the test that there were sizeable out of plane displacements. Hence, the tension grips as described in chapter 2 were modified. Two aluminum plates were attached along the sides of the grips as shown in figure with the help of tightened black adhesive tape as shown in the figure 5.5. The aluminum plate used has two long grooves as shown in figure 5.6. These grooves allow two transparent Para glass pieces to slide into. These two glass pieces are separated by a distance of 3 mm and thereby prevent considerable out of plane movement of the test sample. The samples were then cut at two ends of the grid as shown in figure 5.7

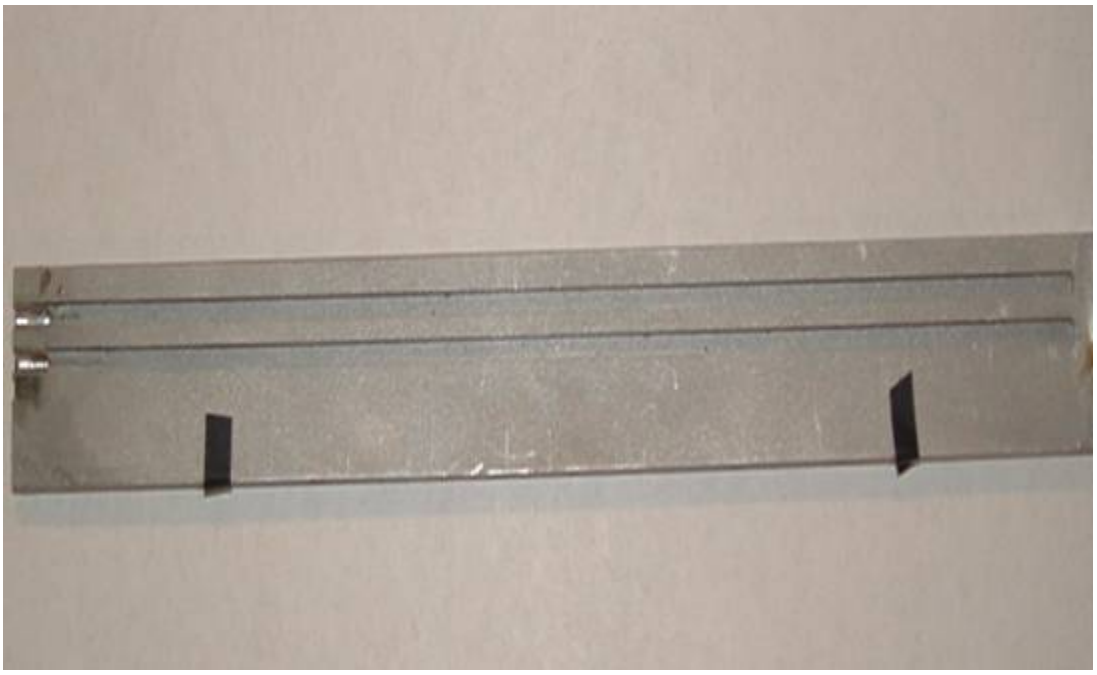

Figure 5.5: Aluminum plate with groves

Figure 5.6: Para Glass Sheet

Figure 5.7: Position of Cuts on the Sample

5.3.2 Image Analysis Program

An image analysis program was developed using the MATLAB digital processing tool box to predict the 2-D full displacement fields of structural woven fabrics. In order to capture the images for the program, a digital frame grabber was used. A monochromatic light source was used to illuminate the specimen while the images were captured at 1 to 15 second intervals.

The program computed the displacements of the 27 points on the 1.5" by 6" grid drawn on the sample. The captured images were processed to quantitatively measure the displacements of these points as a function of the applied strain. These images could be analyzed at various time intervals and magnifications. The image jump and the image resize factor were two variables used that considered varying time intervals and magnifications respectively. The algorithm for the program is as follows

- Input the Number of Images, Image Resize Factor and Image Jump.
- For each image select the area of interest. This area is the same for all analyzed images and is selected by considering three fixed points (no movement along these points during the course of the test). These points form three corners of a rectangle.
- For the cropped image select a datum point (fixed point on the machine or aluminum plates).
- Resize the cropped image using the Image Resize Factor.
- Select points on predefined grid (1.5 by 6 inches). Each pt forms a corner of 0.75 inch square.

- Store the values of pixel coordinates of each grid point for each point for each image.
- Compute the position of each point relative to the fixed datum point
- Compute the displacement of each point in every each image relative to its position in the first image.

Displacement Calibrations

The coordinates of the grid points per image obtained from the program are in terms of pixel coordinates. These need to be converted into standard units (inches or mm.) Figure 5.8 shows a photograph taken for calibration purposes. One can trace an exact known length along this using the pixval command of MATLAB. A small sub routine within the main program is employed to compute the calibration factor that needs to be used to convert the pixel values into known units. Table 5.3 summarizes a sample calibration done by using two fixed points on the aluminum plates with a known distance between them.

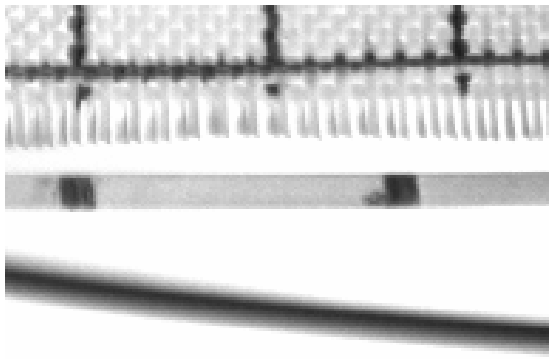

Figure 5.8: Photograph used for calibration

Table 5.3: Sample Calibration

Point 1 Pixel Coordinates X- Direction	Point 2 Pixel Coordinates X- Direction	Difference in Pixel Coordinates	Actual Distance Inches	Calibration Factor
539	339	200	1.3125	152.381

Procedure Validations

The image analysis program was used on an "uncut" sample (Simple tension test sample as discussed in Chapter 2) and its results were compared to the load displacement collected by the MTS system. This comparison was done to verify the feasibility and accuracy of the program in predicting the displacements.

The figure 5.9 shows the naming of grid points on "uncut" sample and the position of the x and y axes for the specimen.

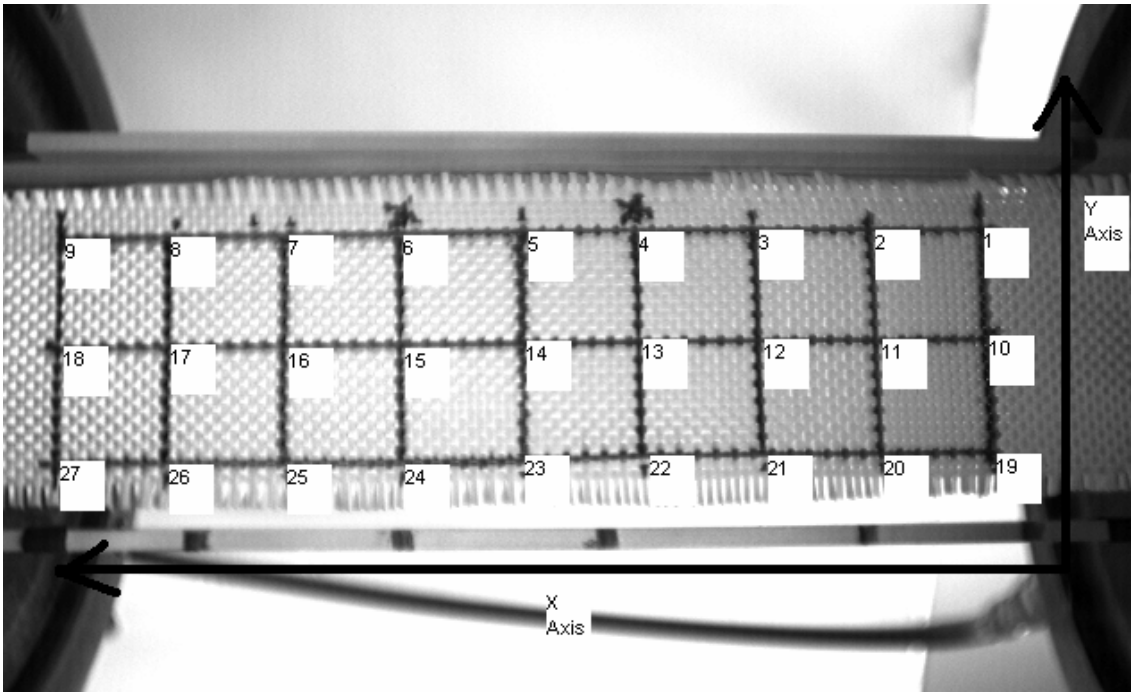

Figure 5.9: Grid on an "uncut" sample

For verification purposes, a Kevlar AS-49 specimen was used on the 22 Kips MTS system. The displacement was applied at the rate of 0.1 in/min. The images were captured every one second. The program was run using an image jump of one second and also by employing an image jump that would vary along the course of the analysis. Figure 5.10 shows the first image used for analysis purpose.

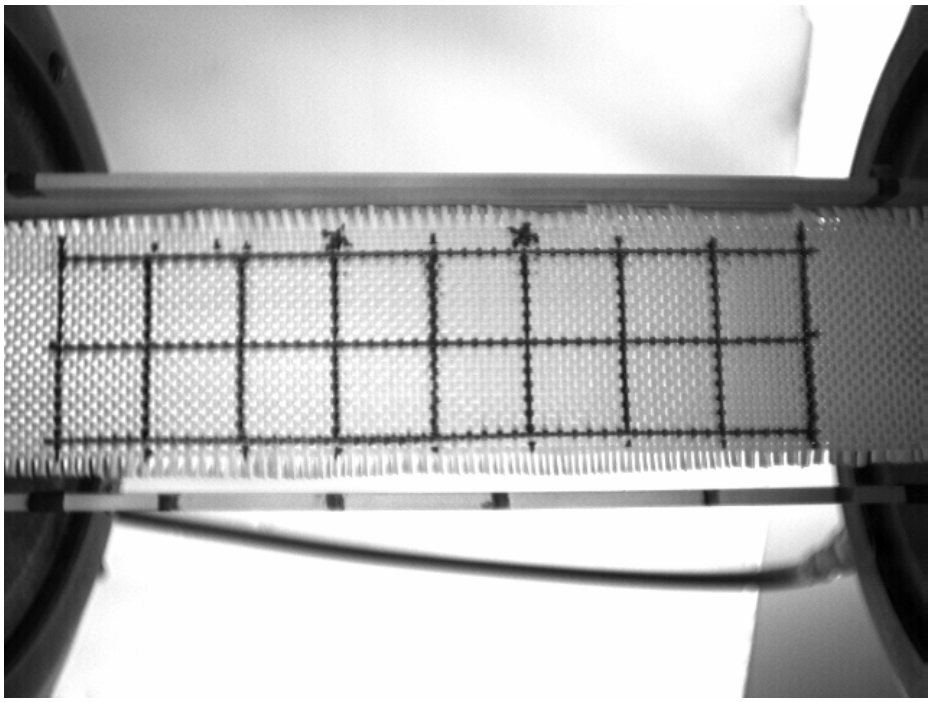

Figure 5.10: First Image Analyzed

In figure 5.11 shows the last image processed. The movement of the actuator during the period of the test is towards the left of the image and hence the final displacements of points 1, 10 and 19 should be relatively less than points 9, 18 and 27. Table 5.4 shows the relative displacements of the aforementioned points at the end of the test calculated using the program. Therefore, the program verifies itself on this account.

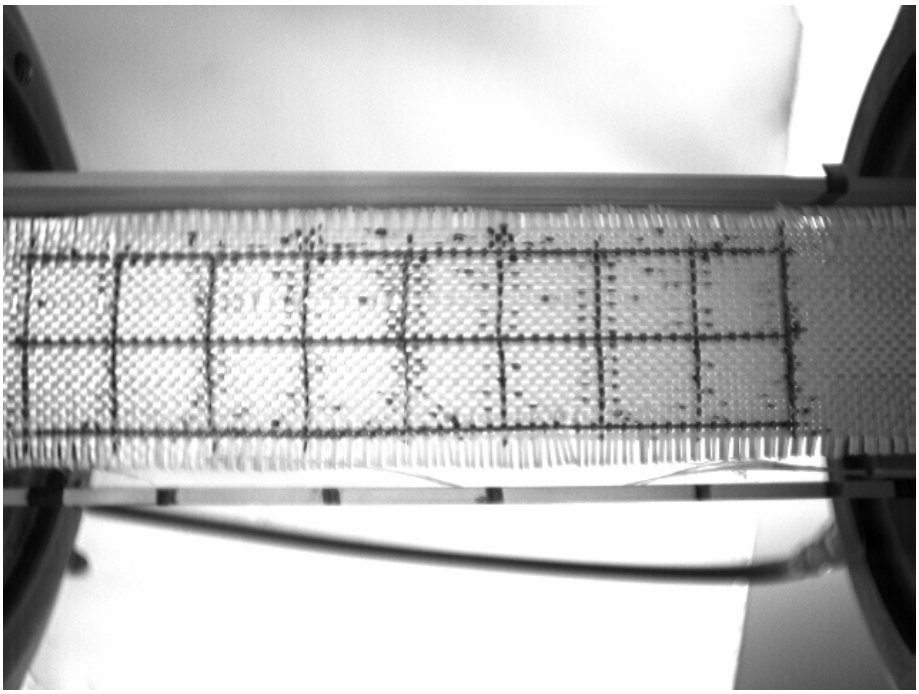

Figure 5.11: Last Image Analyzed

Table 5.4: Relative Displacements of End Points

Point	Final Displacements in Pixels	Point	Final Displacements in Pixels
1	16	9	38
10	19	18	40
19	15	27	36

The displacements obtained by the program are outputted for every image that was analyzed. The process of recording photographs is initialized as soon as the test is begun. Hence, the displacements generated by the program can be related to the time the photograph was taken and in turn to the loading at that point using the MTS machine generated load time data. Therefore, stress strain curves obtained using experimental data

can be compared to the stress strain data that can be obtained from image analysis. A small grid of 1.5” by 1.5” was used for such a comparison. Figure 5.12 shows the grid analyzed (marked with ‘x’).

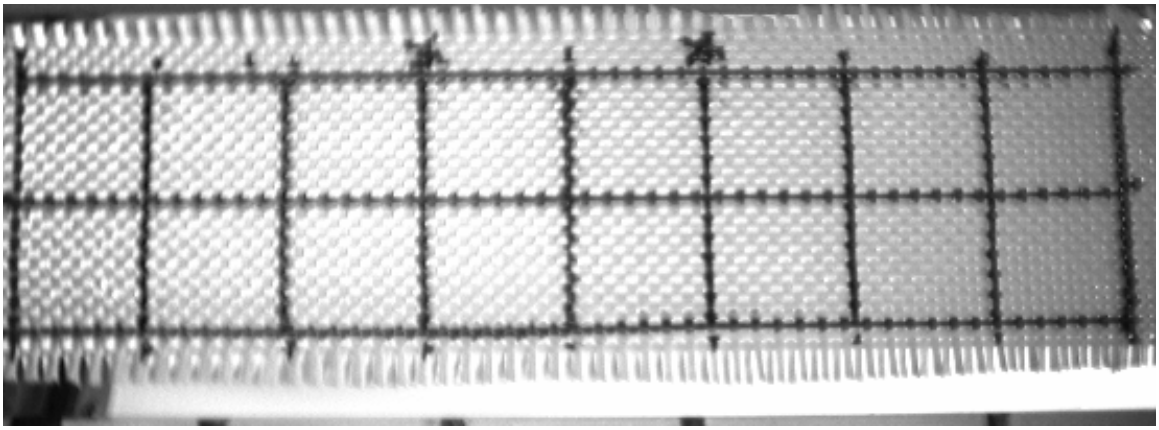

Figure 5.12: Grid Analyzed for Stress-Strain Comparison

Image Analysis was done using Image Jump equal to one and also for a variable image jump. The stress strain plots were drawn for both the cases for the two end points on the smaller grid on the middlemost line. These two plots are compared with the experimental data in figure 5.13 and 5.14 respectively. It was observed that the displacements between 2 points on a line were found to be equal in many cases if image jump is set equal to 1. Hence, a variable image was employed to obtain a better stress strain curve.

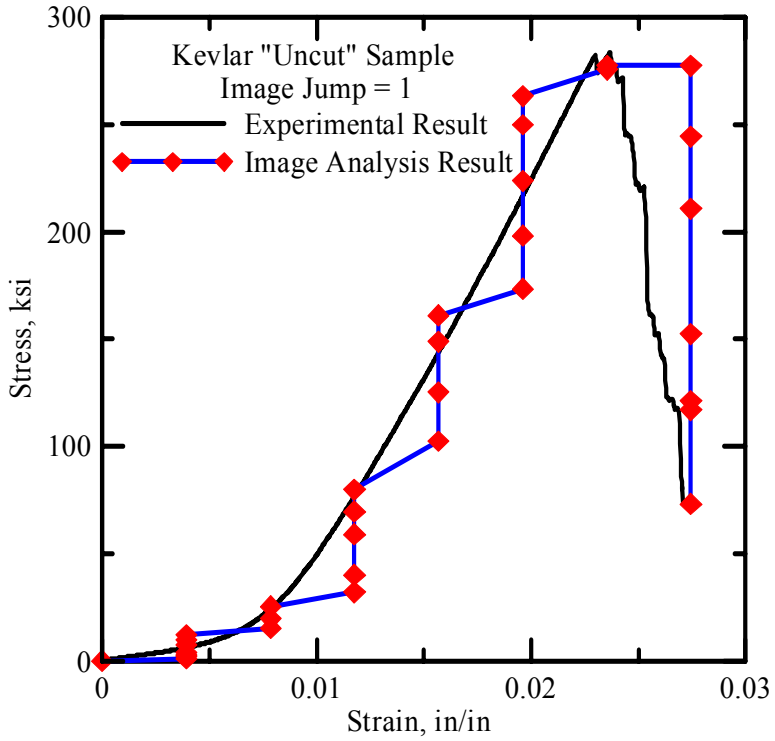

Figure 5.13: Stress Strain Curves using Image Jump = One

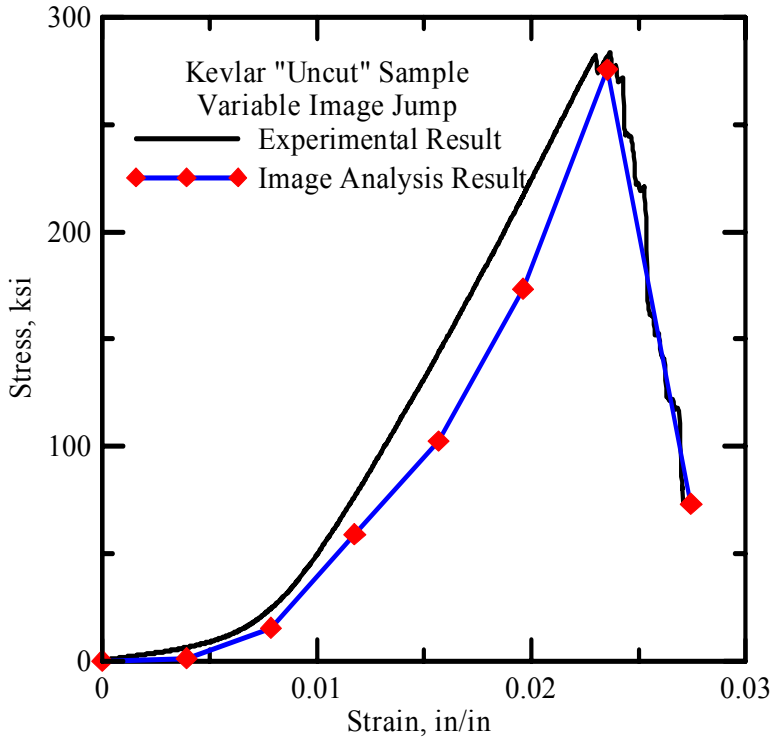

Figure 5.14: Stress Strain Curves using Variable Image Jump

The figure 5.14 shows that the stress strain curve obtained from the variable jump data is comparable to actual stress strain curve obtained for the whole specimen using the experimental data. Hence, it can be concluded that the image analysis program can provide displacement data of various points on a predefined grid with considerable accuracy.

5.3.3 "Cut" Tests Specimens Results

The "cut" sample tests were run on different types of fabrics. The experimental displacement field obtained was matched with the prediction from FE model. The Response Surface Methodology (RSM) was used to carry out the inverse analysis procedure.

Kevlar AS-49

A Kevlar specimen of size 12.5 by 2.25 inches was used to measure the displacement field. A grid of 6.75" by 1.5" was marked on the sample with 30 different points. Points on grid for the cut edge were chosen such that they lied within the two cuts. Figure 5.15 shows the experimental setup. The figure 5.16 shows the first image analyzed and the figure 5.17 shows the final image analyzed. For this particular experiment the image jump used was 6. The figure 5.18 compares the load deflection data from an uncut sample with "cut" sample.

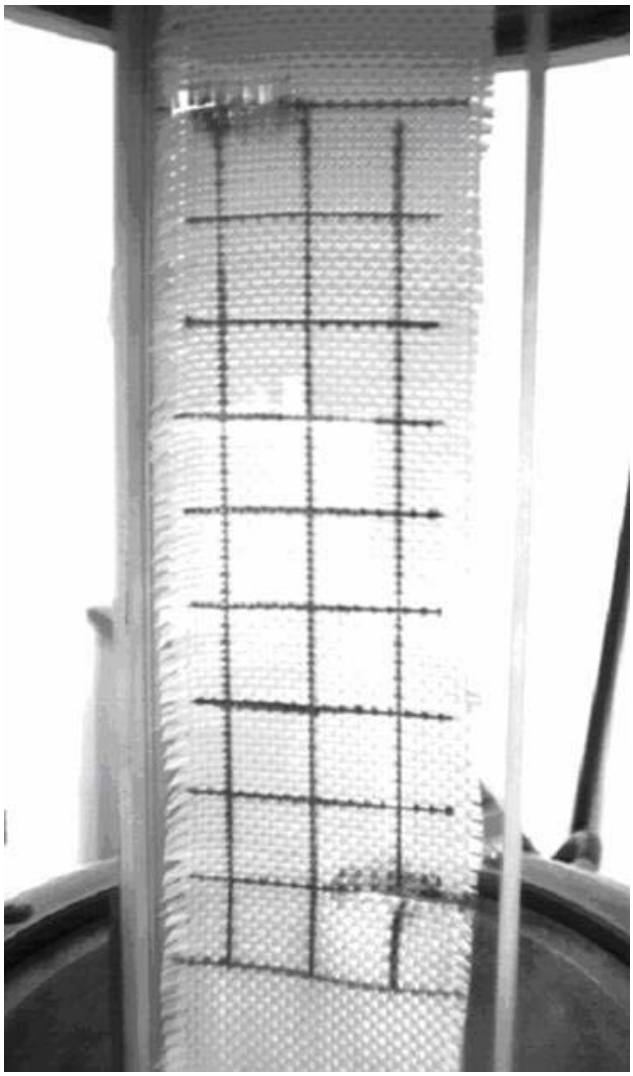

Figure 5.15: Kevlar AS-49 “cut” sample experimental setup

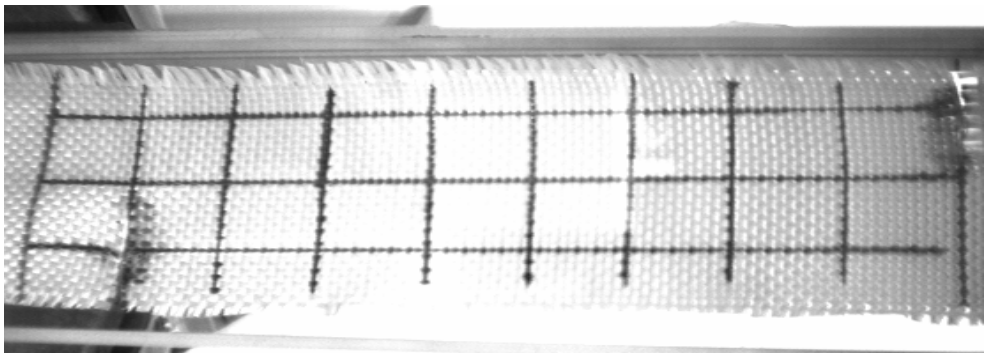

Figure 5.16: Kevlar AS-49 “cut” sample first image analyzed

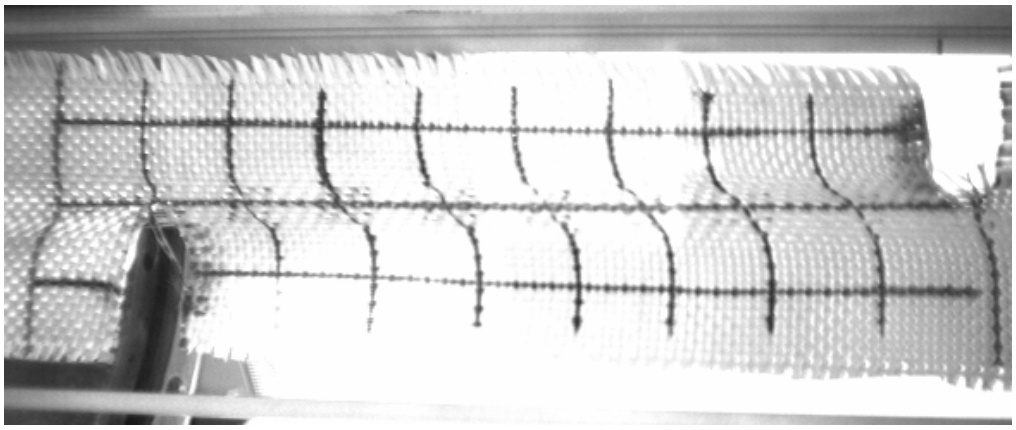

Figure 5.17: Kevlar AS-49 “cut” sample final image analyzed

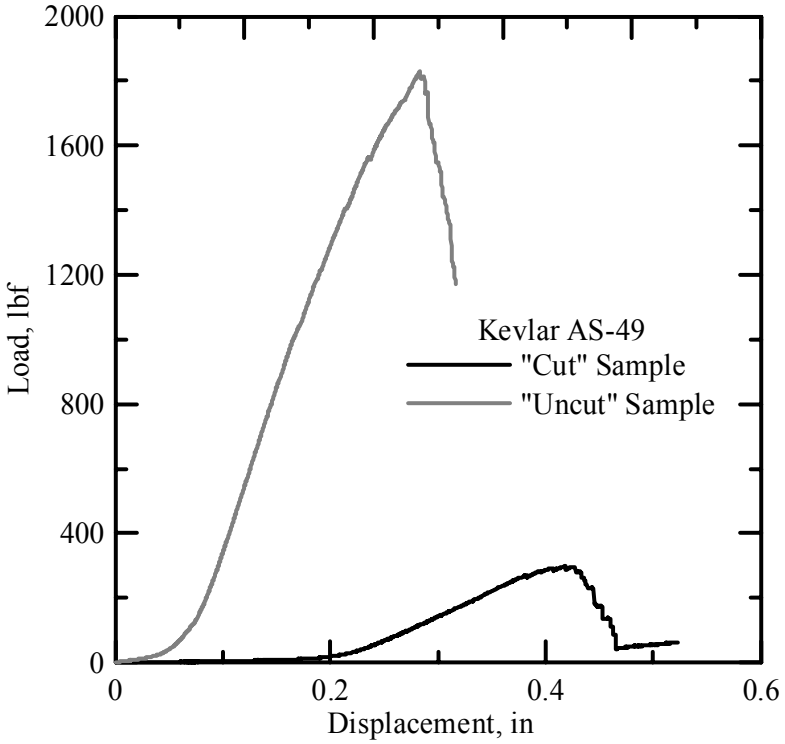

Figure 5.18: Comparison of “Cut” and “Uncut” Kevlar Sample

It can be concluded from figure 5.18 that the “cut” Kevlar sample fails at a much lower load than an “uncut” Kevlar specimen (approximately of the same size). However, the “uncut” sample undergoes more displacement than a uniaxial tensile test sample.

The table 5.5 shows the displacements of the points in pixels on the grid as the test progresses in the direction of loading.

Table 5.5: Relative Displacements of "Cut" Kevlar Sample

Image No	0	6	12	18	24	30	36	42	48	54	60
Time seconds	0	60	120	180	240	300	360	420	480	540	600
					Relative Displacements						
Point											
1	0	6	13	19	25	31	40	47	52	58	68
2	0	6	12	18	25	30	39	46	52	57	66
3	0	4	8	17	22	29	36	43	50	53	63
4	0	5	10	18	24	29	38	43	50	55	65
5	0	5	9	17	23	28	38	43	48	54	64
6	0	5	9	16	21	27	35	41	46	52	62
7	0	6	10	15	20	26	33	39	45	49	59
8	0	5	6	15	20	25	32	38	43	48	58
9	0	2	6	13	17	23	30	34	38	45	54
10	0	6	10	16	20	25	31	37	42	48	55
11	0	5	5	11	14	12	20	20	20	20	24
12	0	6	7	11	13	14	20	21	23	27	32
13	0	4	6	11	11	16	20	22	24	27	34
14	0	3	6	11	12	14	20	21	23	26	33
15	0	4	7	11	12	15	19	22	24	25	34
16	0	4	6	10	12	15	20	22	24	27	35
17	0	3	6	10	12	14	20	22	26	29	38
18	0	4	5	9	12	13	18	21	25	28	36
19	0	2	3	7	9	11	18	18	22	25	34
20	0	2	4	8	11	13	19	22	25	31	39
21	0	3	3	6	5	6	8	7	7	4	7
22	0	4	5	7	6	5	7	7	7	5	7
23	0	3	4	5	5	3	7	5	4	4	6
24	0	3	5	6	5	5	6	4	4	2	7
25	0	3	5	6	5	3	6	2	3	1	5
26	0	4	3	6	5	3	4	2	2	1	4
27	0	3	4	6	4	2	3	2	-1	0	2
28	0	4	4	5	3	1	4	1	-2	-1	2
29	0	3	4	5	6	4	3	5	-6	-4	5
30	0	5	9	15	19	23	31	35	39	46	54

The following observations can be made from the displacements generated by the image analysis program.

- X displacements of points in the topmost line of the grid maximum
- Relatively smaller displacements of points in the middlemost line.
- Displacements least on points on bottom most grid line. (Point near the grip shows displacement comparable to topmost line).
- Negative Displacements tend to occur on points on the bottom most point inside the cut.

Finite Element Analysis

The basic procedure for the finite element analysis is as follows (please refer to

1. A computer program was written using regression analysis to model the behavior of the fabric for the "cut" sample.
2. The ABAQUS/Standard analysis is run with the obtained regression coefficients varying the shear modulus parameter of the material model. The shear modulus is assumed to be a piece-wise approximation with 4 linear curves.
3. The program is rerun with different values of shear modulus until the objective function, which is based on the normalization of the differences between the displacements, is minimized and the displacements through the FE and Image Analysis match.

The experimental setup was modeled with the same FE material model used for the static ring tests except that the shear modulus value was varied using response surface

method (not assumed to be a certain fraction of the modulus of elasticity). The analysis was a displacement controlled static analysis that involved non-linear stress strain behavior for the fabric with loading and unloading in both E_{11} and E_{22} direction. The finite element analysis was run using solid elements (8-noded hexagonal elements), plane stress elements (4-noded quadrilateral elements) and shell elements. The results of the FE analysis are shown in figure 5.19. The images represent the final result at the last load step (for the last image analyzed). The first image represents the results using the solid elements; the second image shows the plane stress elements while the last image shows the shell elements.

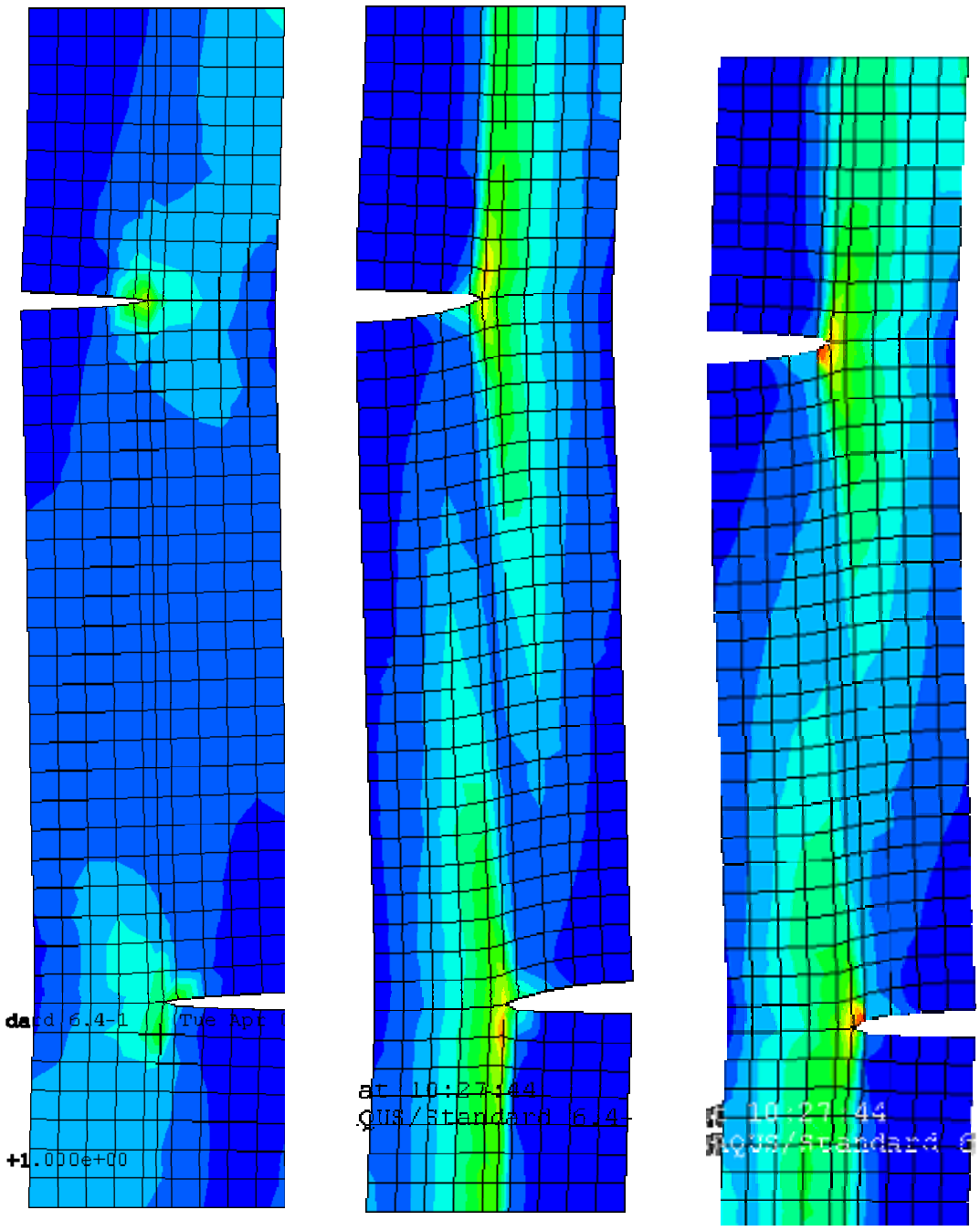

Figure 5.19: FE Analysis Results for “Cut” Kevlar Sample

The figure 5.20 shows the results of the shell elements juxtaposed with the final image analyzed. It can be seen that the shell elements provide a better representation of the final deformed state.

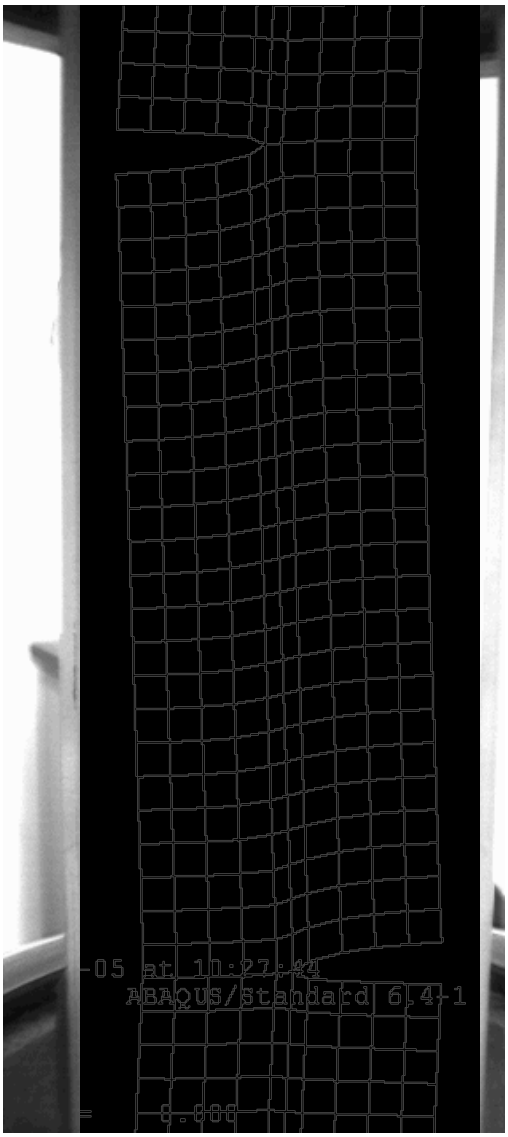

Figure 5.20: Comparison of FE Analysis and Experiment for "Cut" Kevlar Sample

However, the results of the program vary to a great extent. The program has unresolved issues with it. Choosing the lower and upper limits for the shear modulus has a big impact on the final result. The response surface method can only predict the local maximum or minimum. Since the finite element analysis of the fabric is highly non-linear, the program is unable to predict an acceptable value for the shear modulus.

5.4 Picture Frame Tests

A typical shear (or trellis) fixture was developed according to a shear frame developed by Chen, Lussier, Cao and Peng (2002). The figure 5-1 shows the frame developed by ASU. All the three fabrics Kevlar AS-49, Zylon AS-500 and Zylon AS-1500 were tested using this frame.

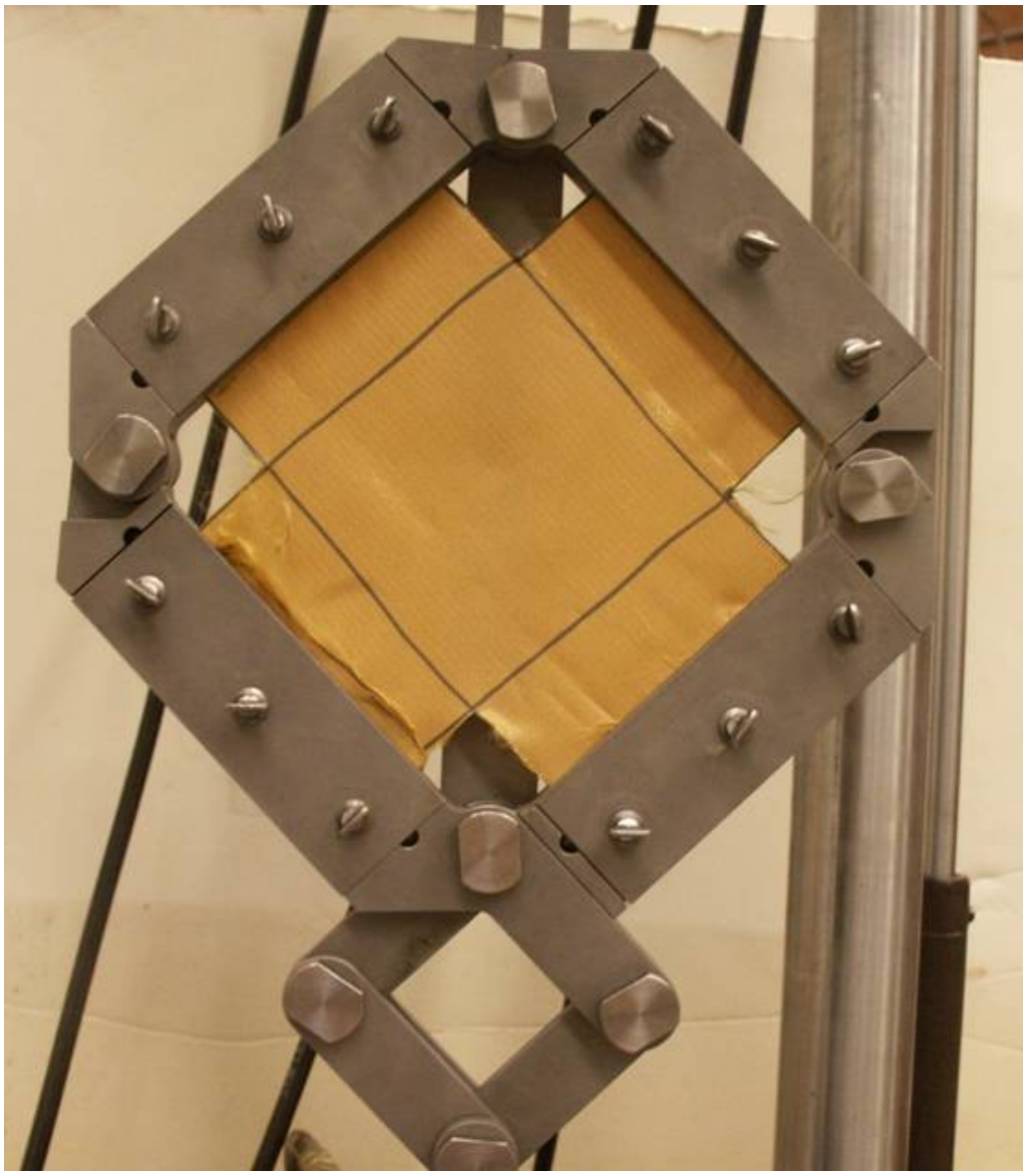

Figure 5.21: Picture Frame Tests

5.4.1 Shear Frame Apparatus

A schematic of the shear (trellis) frame is shown in figure 5.22. The material used for fabricating the frame was steel. The frame consists of five basic parts namely frictionless bearings (7 in number), clamping plates (4 in number), multiplier links, a long plate with a 3.5" slot and two connecting fixtures (for connecting to the top and bottom actuators).

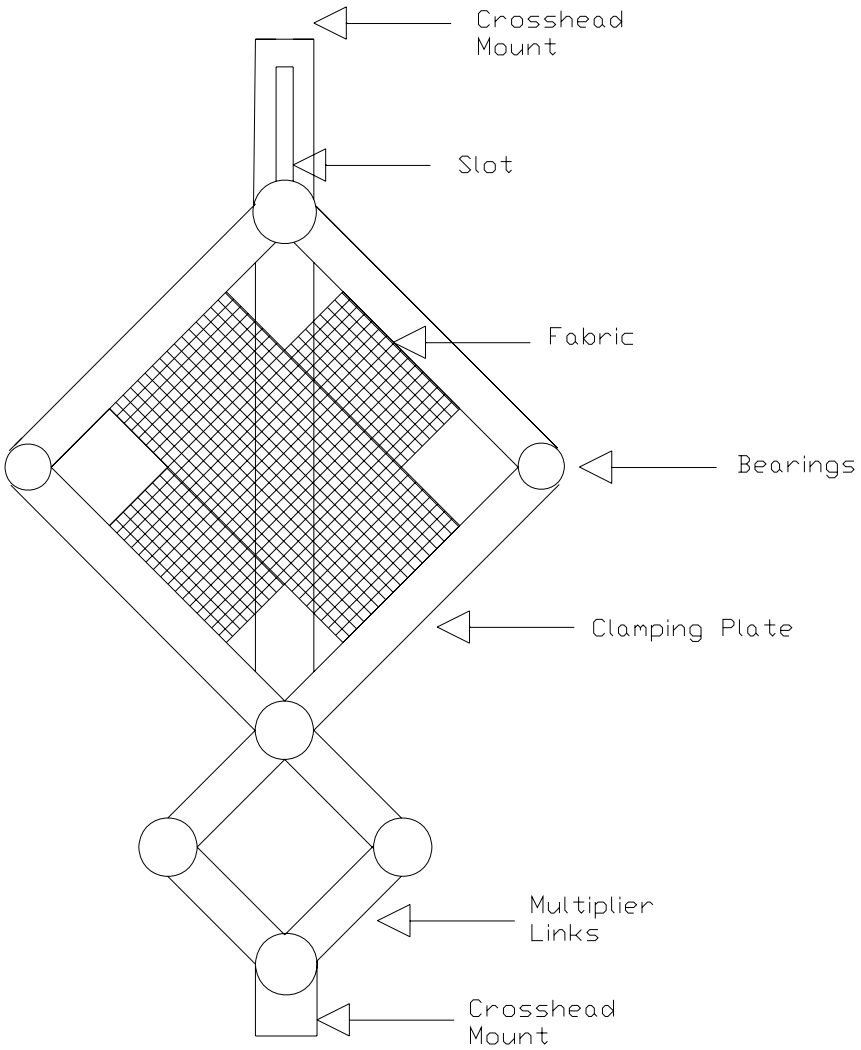

Figure 5.22: Schematic Setup of Shear Frame

Frictionless Bearings

Frictionless bearings of diameter 0.25” each were used for the experiment.

Clamping Plate

The schematic of one of the clamping plates is shown in figure 5.23. The clamping plate has maximum thickness of 0.75” and a minimum thickness of 0.25”. The rectangular slot in the plate is of size 5” by 1.71”. A rectangular plate (figure 5.24) is fixed into this slot and lies on top of the fabric to be tested.

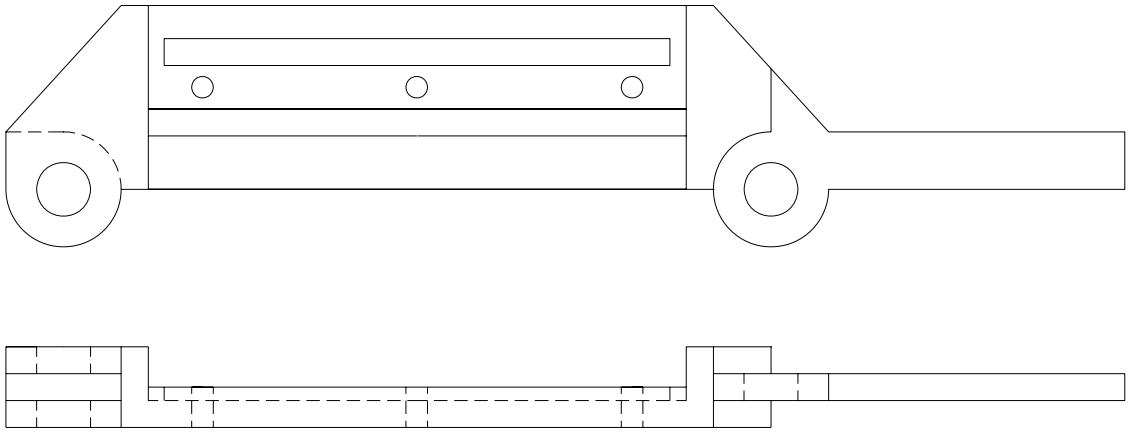

Figure 5.23: Schematic Setup for a Clamping Plate

The material (fabric) is held onto the frame by gripping mechanism similar to the tension tests V-notch grips. The figure 5.24 shows the gripping mechanism used for the shear frame.

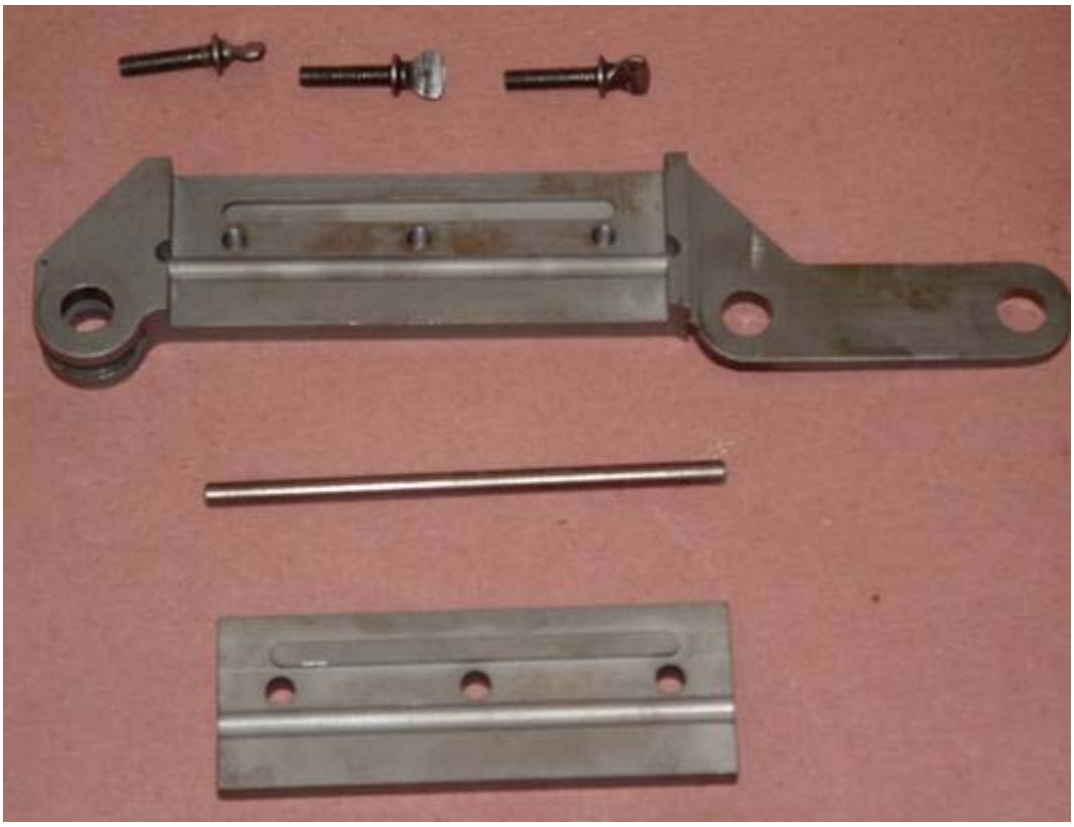

Figure 5.24: Gripping Mechanism for the Claming Plate

The fabric is wound over the circular rod (figure 5.24) and placed in the circular slot in the top part of the clamping plate. The rectangular part of the clamping plate is then fixed onto the top with the help of three set screws. The tightened set screws at the top of the plates keep the assembly intact and prevent the fabric slipping through the application of uniform mechanical pressure.

Multiplier Links

The multiplier links increase testing rates roughly two and half times the crosshead speed. Slight tension variations due to this procedure did not significantly affect the results. The center to center distance between the bearings on a single multiplier link is 2.75”. Before the start of the test the multiplier links are at 90° to each other.

Slotted Steel Plate

The long steel plate used behind the shear frame holds the shear frame in its original position (fabric is held at 45° direction to the loading direction). The slot in the plate facilitates the movement of the shear frame in the loading direction.

Connecting Fixtures

The connecting fixtures are used to mount the frame into the hydraulic grips of the 22 Kips MTS system. The top cross head mount remains stationary while the bottom cross head mount moves at the rate of 0.1”/min.

5.4.2 Shear Parameters Calculations

Shear Angle Calculations

The shear angle is may be defined as the angle through which the fabric has sheared. The multiplier link movement induces upward movement of the clamping plates in the machined slot. Initially, in the stationary position, the links are at 90° to each other. During the testing of a fabric, downward movement of the actuator results in increase in the distance between the vertical opposite bearings connecting the multiplier links (top

bearing is connected the two bottom clamping plates and bottom bearing is connected to the lowermost multiplier links and the assembly that clamps into the bottom hydraulic grips of the 22 kips MTS system. Figure 5.25 shows the multiplier links.

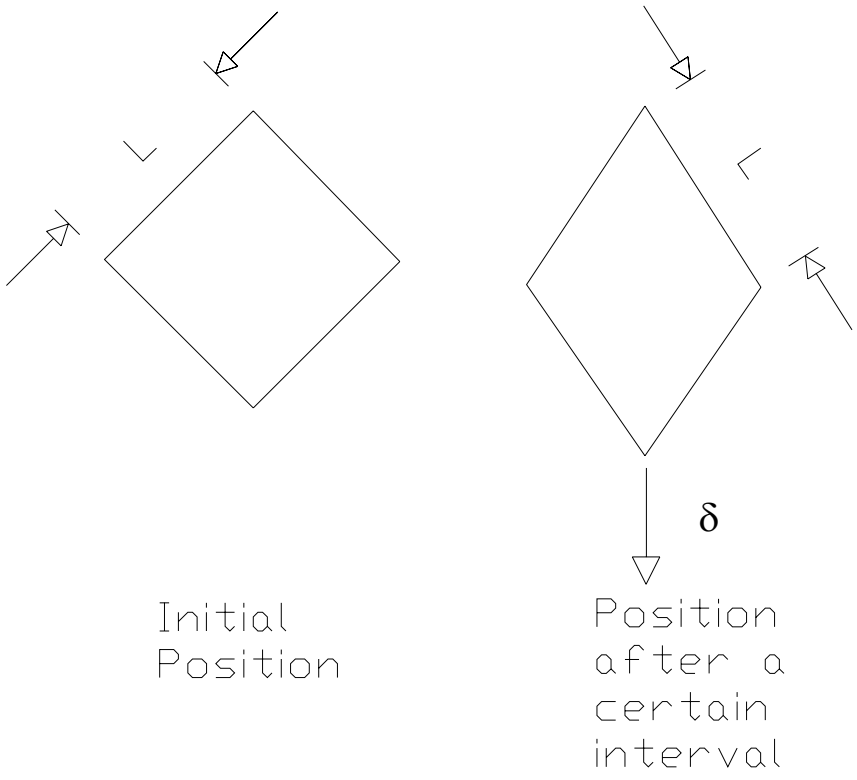

Figure 5.25: Movement of Multiplier Links

Let L be the center to center distance between the bearings attached on the multiplier links along the links as shown in figure 5.25. This distance remains constant throughout the period of the experiment. In the initial position (before the start of the experiment), the diagonal distance between the bearings is $\sqrt{2}L$ (diagonal of a square). After a time t during the course of the experiment let the displacement be δ. Then, the

vertical diagonal would be √2L+ δ. The cosine rule can be used to obtain the obtuse shear angle between the multiplier links. This angle θ in degrees is given by equation (2).

$$\theta = \cos^{-1}((-2\sqrt{2}L\delta - \delta^2)/2/L^2) - 90 \qquad (2)$$

Since, the triangles formed by multiplier links and the clamping plates are similar to each other, the angle θ can be considered as the shear angle for the test fabric. Typically, θ starts at 0° and increases as the trellis frame deforms.

Shear Stress Calculations

The figure 5.26 shows the free body diagram of the trellis frame. The shear load per unit length of the test fabric in the clamping plate can be related to the load recorded by the machine. Let this shear load per unit length be τ and the actuator load P. The shear load in each clamping plate is F. If the length of the fabric in the clamping is S, then

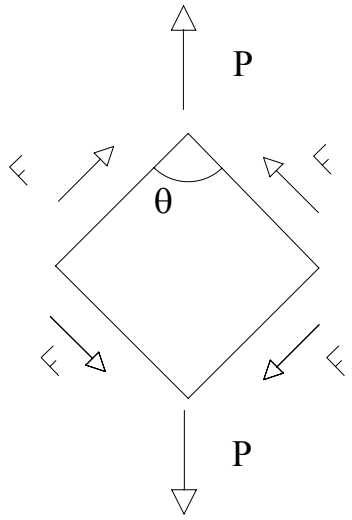

Figure 5.26: Free Body Diagram for Picture Frame

$$F = \tau * S \quad (3)$$

Using the free body diagram

$$P = 2 * F * \cos(\theta / 2) \quad (4)$$

Hence,

$$\tau = 1/2 * P / S * 1/\cos(\theta / 2) \quad (5)$$

The shear stress can be computed by normalizing τ with the thickness for each fabric.

5.4.3 Shear Frame Results

The picture frame tests can be used to plot actuator load versus actuator displacement and actuator load versus the fabric shear angle. The typical shear response shows an initial region with large increase in shear angle with minimal increase in the actuator load. During this initial phase, the yarns begin to rotate offering a small resistance to the applied shear loading. After this phase, the fabric load tends to increase rapidly. In this phase, it can be assumed that the yarns to compress each other laterally at the crossover points. Finally, the ending part of load-shear angle curve shows there is a rapid increase in load with minimal increase in the displacement. During this ending stage, the trellis frame itself is being tested and the experiment is stopped.

Kevlar AS-49

A Kevlar AS-49 sample of size 10” by 10” was cut such that the total fabric area minus the corner cut outs was 75 square inches while the test fabric area was 5” by 5”. The tested Kevlar fabric is shown in figure 5.27.

Figure 5.27: Kevlar Test Fabric for Picture Frame Tests

The load deformation plot of the Kevlar sample is shown in figure 5.28. The sample was tested twice by shifting the tested fabric by 90° in the shear frame. Shear stress strain plot is shown in figure 5.29. It can be seen that for the Kevlar Fabric, during the second tests there is comparatively less loading in the initial phase as compared to the original fresh fabric tested.

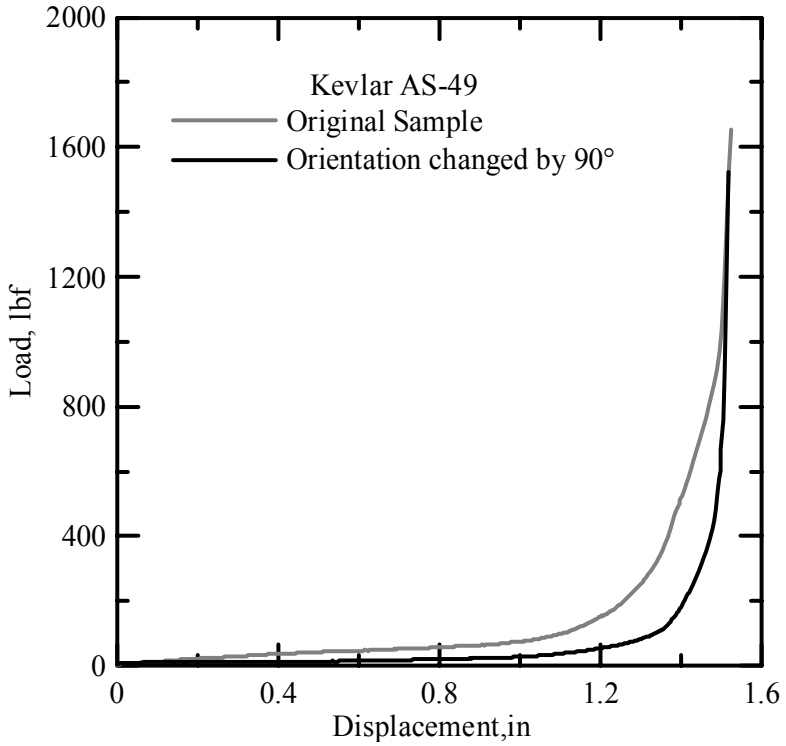

Figure 5.27: Load Deformation Plot for Kevlar Test Fabric for Picture Frame Tests

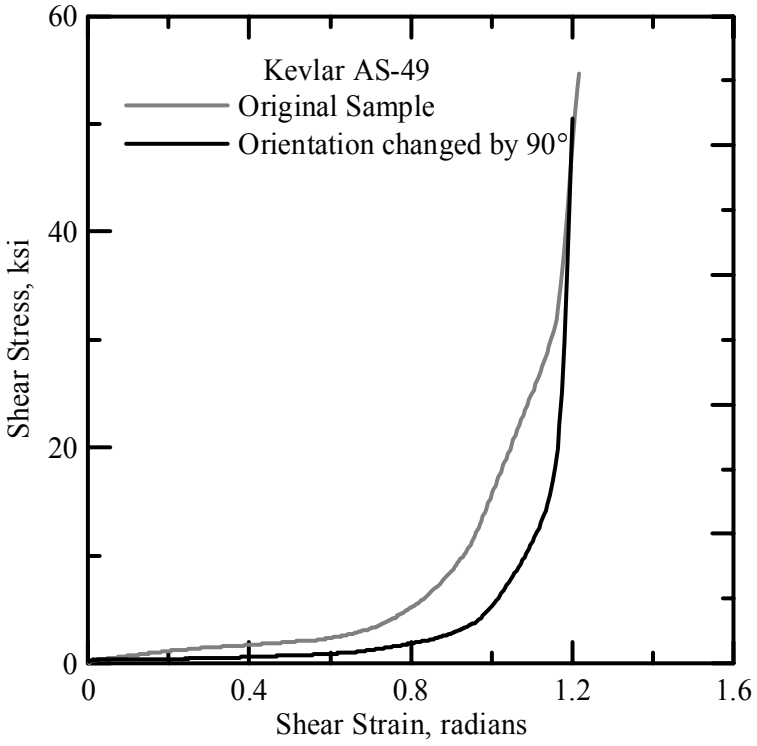

Figure 5.28: Shear Stress Strain Plot for Kevlar Test Fabric for Picture Frame Tests

The figure 5.30 shows the Kevlar test in the initial stage of loading while figure 5.31 shows the sample in the final stage of loading.

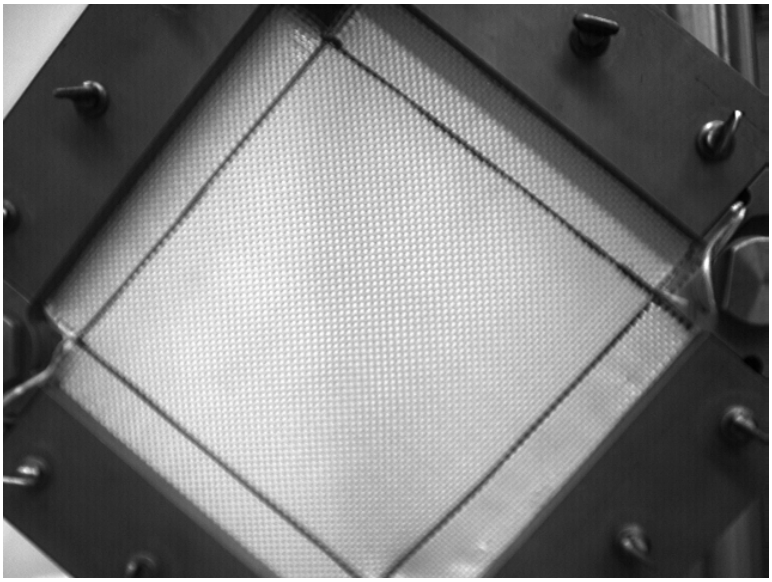

Figure 5.30: Kevlar Test Fabric for Picture Frame Tests in Initial Stage of Loading

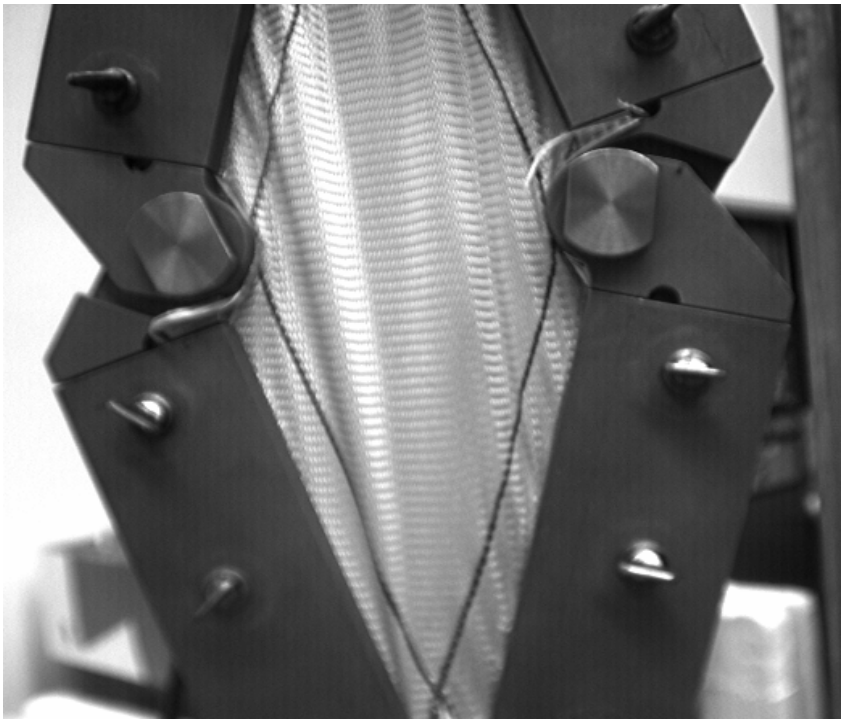

Figure 5.31: Kevlar Test Fabric for Picture Frame Tests in Final Stage of Loading

The figure 5.31 indicates that compression buckling occurs in Kevlar during the final stages of loading.

Zylon AS-500

A Zylon AS-500 sample of size 10” by 10” was cut such that the total fabric area minus the corner cut outs was 75 square inches while the test fabric area was 5” by 5”.

The load deformation plot of the Zylon AS-500 sample is shown in figure 5.32. The sample was tested twice by shifting the tested fabric by 45° in the shear frame. The stress strain plot is shown in figure 5.33. It can be seen that for the Zylon Fabric, the same plot is obtained for in both the cases. Also, there is a steep rise in the load during the final phase of the testing.

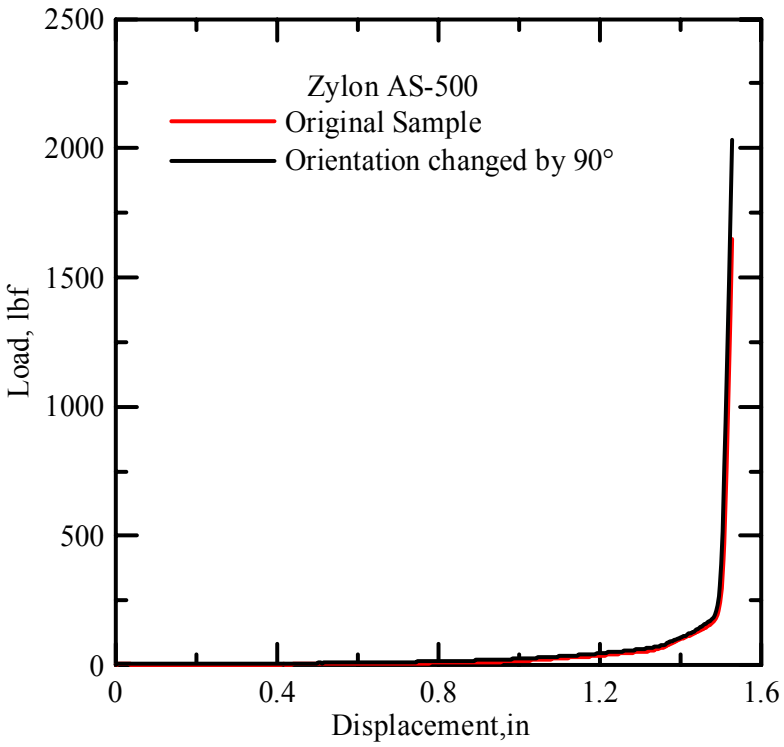

Figure 5.32: Load Deformation Plot for Zylon AS-500 Test Fabrics

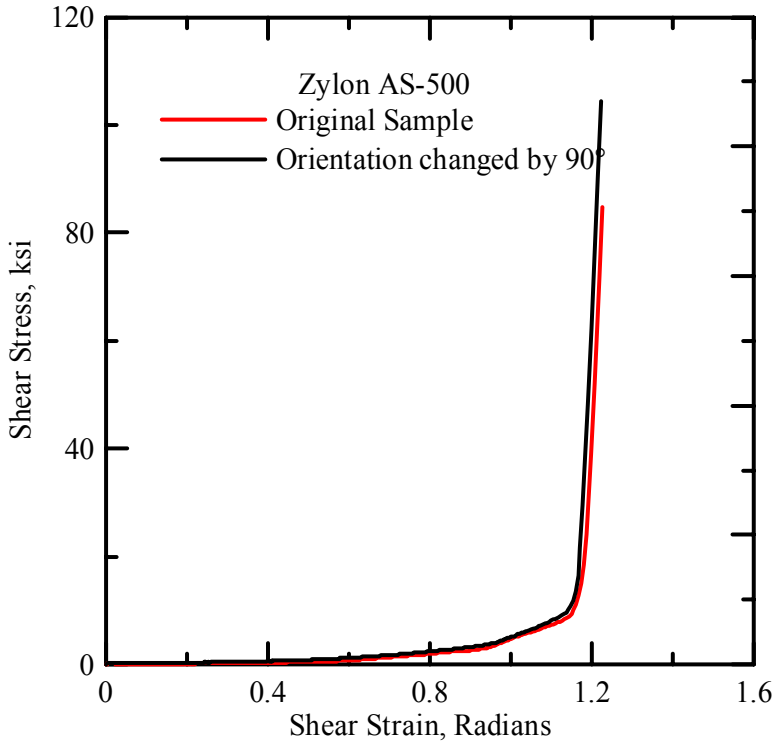

Figure 5.33: Shear Stress Strain Plot for Zylon AS-500 Test Fabrics

Zylon AS-1500

A Zylon AS-1500 sample similar to the Kevlar AS-49 and Zylon AS-500 samples was cut and tested in the trellis frame with similar configurations of the orientation of the fabric.

The load deformation plot and load shear angle plot for the 1500D Zylon are shown in figures 5.34 and 5.35 respectively. It is seen that the orientation shifted sample is slightly weaker than the originally tested sample.

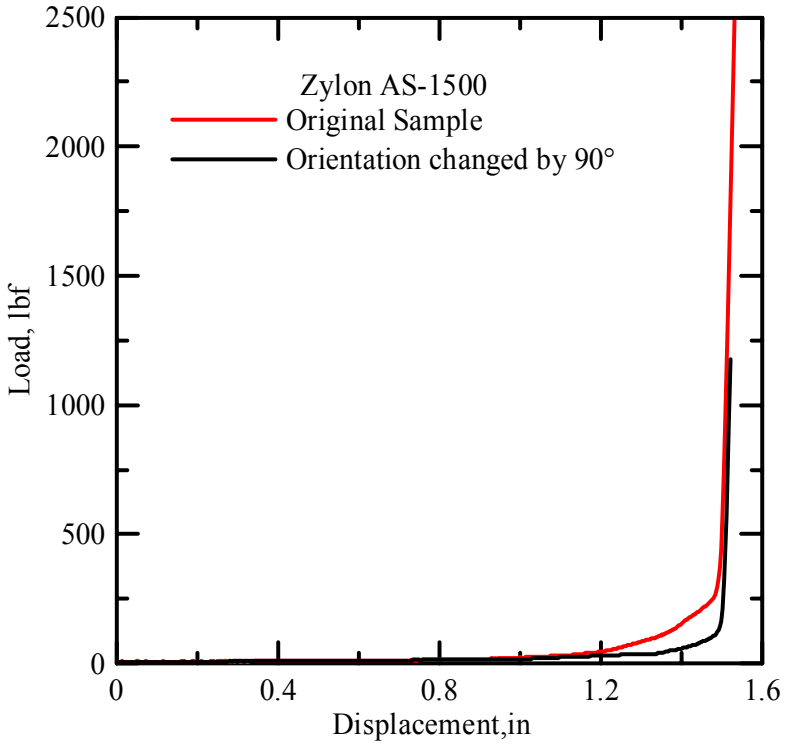

Figure 5.34: Load Deformation Plot for Zylon AS-1500 Test Fabrics

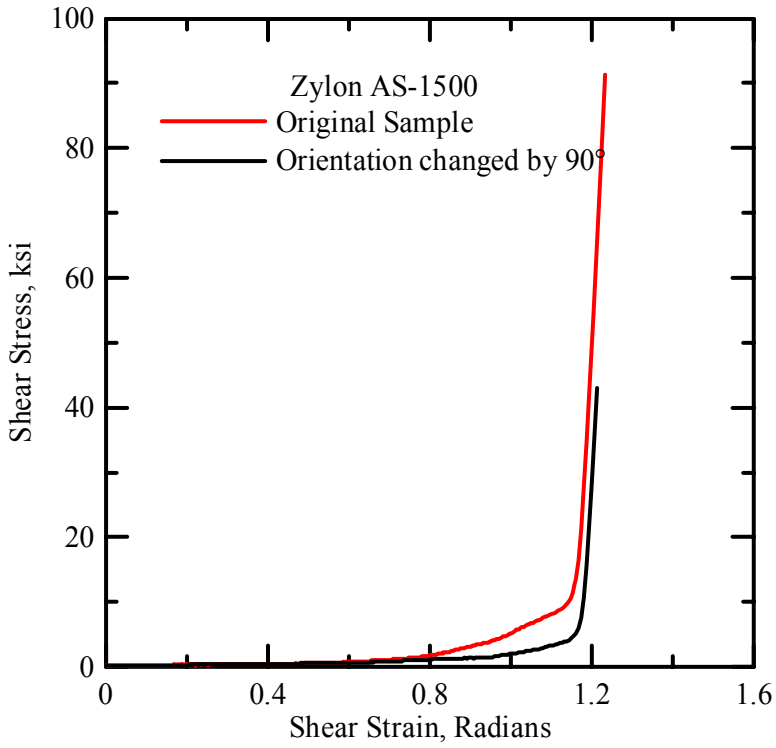

Figure 5.35: Load Shear Angle Plot for Zylon AS-1500 Test Fabrics

5.4.4 Finite Element Simulation

The shear modulus for the fabrics can be computed by creating a model that mimics the deformations obtained through the picture frame tests. The shear parameters for the model can be modified until a similar shear stress strain response is obtained. An FE Approach similar to the one established by Gorezyea, Sherwood, Lussier & Chen for 7th International LS-DYNA users conference can be used.